THESIS

# DIMETHYL ETHER AS A COMPRESSION IGNITION ENGINE FUEL FOR SIMULTANEOUS $NO_X$ AND PM REDUCTION

Submitted by

Matthias Rollins

Department of Mechanical Engineering

In partial fulfillment of the requirements

for the Degree of Master of Science

Colorado State University

Fort Collins, Colorado

Spring 2026

Master's Committee:

Advisor: Daniel B. Olsen

Dan Wise

Jeremy Daily

# ABSTRACT

## DIMETHYL ETHER AS A COMPRESSION IGNITION ENGINE FUEL FOR SIMULTANEOUS $NO_X$ AND PM REDUCTION

Dimethyl ether (DME) is an alternative compression ignition (CI) fuel capable of achieving low nitrogen oxide (NOx) and particulate matter (PM) emissions simultaneously while maintaining diesel equivalent power. However, its behavior under varied injection timing, exhaust gas recirculation (EGR) rates, and multi-condition operation remains insufficiently characterized for practical calibration and commercialization. This research investigates the combustion, emissions, and performance characteristics of DME relative to diesel using a fully instrumented John Deere 6068CI550 single cylinder research engine (SCRE) modified for high pressure common rail DME operation. Baseline diesel and DME tests were conducted at three ISO 8178 C1 steady-state modes, matching location of 50% mass burned (CA50), indicated mean effective pressure (IMEP), and EGR to isolate fuel property effects. Subsequently, an injection timing sweep and a full EGR sweep at 1600 rpm and 50% load were performed to evaluate phasing sensitivity, emissions tradeoffs, and combustion stability limits.

Baseline comparisons show that DME produces substantially lower PM compared to diesel which is composed of more than 95% organic carbon (OC) with less than 5% elemental carbon (EC). DME also reduces $NO_x$ by 10%–35% across baseline conditions, while maintaining diesel equivalent thermal efficiency. Combustion analysis confirms that DME exhibits a single-stage premixed heat release structure with significantly lower peak apparent heat release rates (AHRR) and 4–5 deg shorter 10 to 90% mass fraction burned duration (CA10–90) compared to

diesel. These trends reflect rapid fuel vaporization, uniform mixture preparation, and elimination of diffusion limited burning.

Injection timing sweeps demonstrate that retarding CA50 progressively decreases $NO_x$, with all cases beyond 15 deg ATDC falling below the diesel baseline, but at the cost of increasing brake specific fuel consumption (BSFC). Phasing also becomes more consistent at retarded timings, as indicated by reduced coefficient of variation (COV) of CA50. EGR sweeps reveal that DME sustains stable combustion up to 55% EGR, beyond which COV of IMEP and CA50 start to increase. Higher EGR extends start of injection to 5% mass burned (SOI–CA5) and CA10–90 and reduces peak AHRR, indicating slower reaction rates under heavy dilution. A combustion incompleteness threshold emerges below approximately 0.1 g $kWh^{-1}$ $NO_x$, where carbon monoxide (CO), total unburned hydrocarbons (THC), and BSFC rapidly rise.

Overall, this study fulfills its objectives by identifying optimal operating conditions for low $NO_x$ and low PM DME combustion while maintaining diesel baseline power. The results demonstrate that DME can simultaneously achieve low $NO_x$ and low PM without the traditional diesel PM–$NO_x$ tradeoff, with optimal performance occurring near CA50 of 16 deg ATDC and EGR levels of 30%–40%. These findings provide a foundation for future DME engine development and support its viability as a low emission fuel.

TABLE OF CONTENTS

# CHAPTER 1: INTRODUCTION

## 1.1 Background and Motivation

Diesel fueled compression ignition engines have a tradeoff between $NO_x$ and PM emissions[1]. Engine developers finding an optimal point in this tradeoff and then specifying an aftertreatment system to reduce the remaining emissions. EGR, which recirculates cooled exhaust gases back into the intake to dilute the air with inert gases of a higher specific heat. This results in lower combustion temperatures and less oxygen availability, reducing the formation of $NO_x$. In diesel fueled engines this reduction in combustion temperatures and dilution are results in a greater formation of PM. DME is an alternative compression ignition fuel with a high cetane number (~55) that shows promise with high EGR tolerance and low $NO_x$/PM tradeoff[2]. The goal of this research is to determine the optimal operating conditions for low emissions and high efficiency of DME while maintaining diesel baseline brake power.

DME is gaining attention as a promising alternative fuel for CI engines due to its ability to significantly reduce emissions while maintaining performance[3], [4], [5]. DME inherently produces very low PM, even at high EGR rates, making it especially attractive for meeting stringent off-road emissions standards such as U.S. EPA Tier 4 Final (0.02 g $kWh^{-1}$ PM) and EU Stage V (0.015 g $kWh^{-1}$ PM)[6], [7]. A study by Kim et al. demonstrated that, at a fixed IMEP, DME generated negligible soot emissions compared to diesel and sustained stable combustion at EGR rates up to 45% [5]. These characteristics demonstrate that DME's inherently low soot combustion and favorable response to EGR provide a viable pathway for reducing $NO_x$ without

the accompanying increase in PM that typically constrains diesel engines, enabling simultaneous control of both pollutants in heavy-duty applications.

The Department of Energy (DOE), the project sponsor, has identified DME as a candidate fuel that supports its mission to address energy and environmental challenges through transformative technology solutions[8]. Interest in DME has grown not only because of its ultra-low soot combustion characteristics, but also because it can be produced from renewable feedstocks using carbon neutral pathways, including $CO_2$ to methanol to DME synthesis, which further aligns with DOE's long term decarbonization goals[9]. This project aims to promote the commercialization of DME engines by advancing injection hardware and developing combustion strategies that exploit DME's unique fuel properties to minimize engine out $NO_x$. These objectives also align with the Biden Administration's Justice40 initiative, as lowering $NO_x$ and PM emissions has the potential to improve air quality for agricultural and industrial communities[10]. By aligning with both DOE's mission and national policy goals, this research demonstrates the relevance of DME combustion development for advancing cleaner, more equitable, and commercially viable engine technologies[11].

## 1.2 Research Gap and Contributions

Previous studies on DME as a fuel for CI engines have consistently demonstrated its potential to achieve low PM emissions and under optimized conditions, reduced $NO_x$ emissions[4], [5], [12]. DME's high cetane number (~55) and oxygen content contribute to its non-sooting combustion, leading to near zero PM emissions even without advanced aftertreatment systems[2]. For instance, research on agricultural tractor engines fueled with DME reported ultra-low soot and PM emissions, highlighting DME's suitability for applications requiring stringent emission standards[13].

Regarding $NO_x$ emissions, studies have shown that while DME combustion can produce lower $NO_x$ levels compared to conventional diesel, achieving optimal $NO_x$ reduction requires careful calibration of injection strategies and EGR rates. For example, a study on a heavy-duty CI engine demonstrated that DME could meet current and future emissions standards with minimal exhaust gas aftertreatment when operating at an efficiency optimal $NO_x$ level of around 8 g/kWh. This was achieved by balancing injection phasing, injection pressure, and EGR variations [14]. However, excessively high EGR rates can lead to combustion instability and reduced engine performance, indicating the need for optimized EGR strategies [15].

Unlike previous DME studies, which typically evaluate EGR effects at a single operating condition, this work performs a full EGR sweep at one speed–load point and extends the analysis to two additional operating points using both nominal and 50% EGR[16], [17], [18], [19]. This provides a broader multi-condition assessment of DME's EGR tolerance while maintaining IMEP matched to a diesel baseline. By combining injection timing sweeps with EGR sweeps, this work identifies, cycle controllable strategies that optimize combustion phasing, minimize $NO_x$ emissions, and preserve brake power. This approach provides a comprehensive mapping of DME's operational envelope, addressing a critical gap in prior studies and offering practical insights for engine calibration and real-world implementation of DME as a low emission alternative fuel.

### 1.3 Key Variables and Performance Metrics in Compression Ignition Engines

CI engines operate by injecting fuel directly into the combustion chamber near top dead center (TDC), where high in-cylinder pressures and temperatures cause the fuel to auto ignite. The combustion and emissions characteristics of CI engines are strongly influenced by several key variables, including fuel properties, air–fuel mixing, injection timing, and the application of

EGR. These variables determine the spatial and temporal distribution of temperature, pressure, and equivalence ratio, which in turn govern the formation of major emissions such as $NO_x$ and PM.

In CI engines, the dominant $NO_x$ formation pathway is the thermal mechanism, described by the extended Zeldovich mechanism. This mechanism involves the dissociation of $N_2$ at high temperatures and subsequent reactions with oxygen and radical species to form NO, which can further oxidize to $NO_2$. $NO_x$ formation is highly temperature dependent, increasing exponentially with peak flame temperature and local oxygen concentration[20].

PM, is primarily composed of soot, which consists of agglomerated carbon particles with adsorbed organic compounds and trace metals[1]. Soot formation is strongly influenced by spray atomization, in-cylinder air motion, and local pressure. Earlier injection generally promotes better vaporization and air–fuel mixing, reducing fuel-rich zones and thus limiting soot formation[21]. To minimize PM, combustion strategies must therefore focus on improving mixing and reducing air–fuel ratio gradients within the spray, promoting uniform combustion and soot oxidation. When fuel is injected into the cylinder, atomization and evaporation occur, forming a non-uniform mixture of air and fuel. The distribution of this mixture, known as mixture stratification, is a critical factor that dictates combustion efficiency and pollutant formation. Regions within the combustion chamber vary from fuel-rich to fuel-lean, and this non-uniformity results in localized combustion chemistry[22], [23].

$NO_x$ form predominantly in the near stoichiometric burned gas regions, where local temperatures are highest and oxygen is sufficiently available for the thermal $NO_x$ mechanisms to occur[1]. Conversely, soot, the main component of PM, forms within the fuel-rich zones of the

spray core, where limited oxygen availability prevents complete oxidation of hydrocarbons. Within these regions, hydrocarbon fragments polymerize and nucleate into solid carbon particles.

The spatial distribution of air–fuel ratios thus determine the balance between $NO_x$ and soot formation. Improved mixing reduces fuel-rich regions, promoting soot oxidation and decreasing PM emissions. However, enhanced mixing also increases local temperatures, which can elevate $NO_x$ formation. This tradeoff, known as the soot–$NO_x$ tradeoff, is a defining characteristic of diesel combustion [24]. Experimental results by Hountalas et al. demonstrated this behavior. Increasing EGR decreased $NO_x$ emissions through charge dilution and lower flame temperatures but simultaneously increased soot due to inhibited oxidation [25].

CO and THC are direct indicators of incomplete combustion in compression ignition engines. They form when local temperatures or oxygen levels are too low for the oxidation reactions that convert CO to $CO_2$ and hydrocarbons to stable products. Heywood notes that low temperature regions, spray impingement on chamber walls, and crevice volumes all provide environments where these reactions cannot fully proceed [1]. As a result, CO and THC typically originate in fuel-rich or overly diluted pockets that do not burn completely before the expansion stroke cools the gases. Because they respond strongly to any condition that slows or weakens combustion, CO and THC are useful signals that the combustion process is no longer fully efficient.

These emissions become especially important when strategies to reduce $NO_x$ unintentionally weaken combustion. Studies from Jacobs et al. 2003 showed that using EGR lowers flame temperature and oxygen availability which reduces $NO_x$ but causes a clear rise in both CO and THC [26]. Beatrice et al. n.d. observed the same trend when applying clean and cold EGR. Lower temperature combustion greatly reduced $NO_x$ but increased incomplete

combustion products in a single cylinder diesel engine [27]. These results show that efforts to suppress $NO_x$ by lowering temperature or delaying combustion tend to increase CO and THC because the charge does not burn completely. In contrast improving mixing or raising local temperatures reduces CO and THC but increases $NO_x$. This relationship shows that CO and THC are important markers of the limits of low temperature and diluted combustion strategies used to control $NO_x$ in diesel engines.

The properties of the fuel play a fundamental role in defining engine behavior and emissions. Diesel fuel, the conventional CI fuel, is characterized by its cetane number, a measure of ignition quality analogous to the octane number in spark-ignition engines. The John Deere 6068CI550 engine used in this study operates on diesel fuel meeting ASTM D975 specifications for ultra-low sulfur diesel (ULSD) [28]. According to ASTM D975, ULSD fuel of S15 grade must have a minimum cetane number of 40, while John Deere recommends at least 45, or 50 for cold or high-altitude conditions [29]. Diesel is liquid under ambient conditions, offering high energy density with a lower heating value (LHV) of approximately 42.6 MJ/kg [30].

DME, an alternative fuel, has emerged as a promising low emission substitute for diesel. DME exists as a gas at ambient conditions but can be liquefied at pressures above 5.31 bar at 20 °C [2]. Its LHV is 28.9 MJ/kg, lower than diesel, requiring higher mass flow rates for equivalent energy delivery[30]. However, DME possesses a cetane number greater than 55, ensuring excellent ignition quality. Moreover, its molecular structure contains oxygen, which supports more complete combustion and virtually eliminates soot formation under typical diesel operating conditions [2]. The use of oxygenated fuels such as DME can therefore help decouple the soot–$NO_x$ tradeoff by providing internal oxygen for soot oxidation even in fuel-rich regions. Zhu et al.

demonstrated that increasing fuel oxygen content allowed $NO_x$ to decrease with EGR addition while maintaining nearly constant soot emissions[31].

Injection timing is one of the most influential engine control parameters affecting both performance and emissions. Advancing injection timing allows combustion to occur earlier in the expansion stroke, increasing in-cylinder pressure and temperature, which improves efficiency but tends to increase $NO_x$ emissions. Conversely, retarding injection timing delays combustion, reducing temperature and $NO_x$ formation but often resulting in incomplete combustion and higher PM emissions. Raeie et al. observed that early injection timing in a CI diesel engine produced lower PM emissions but higher $NO_x$ levels[32]. A separate study found that retarded injection timing reduced $NO_x$ but increased soot due to incomplete oxidation in cooler, fuel-rich regions[33]. These results show the role of injection phasing in balancing the soot–$NO_x$ tradeoff.

EGR is another key variable that affects both combustion and emissions. EGR involves redirecting a portion of the exhaust gases back into the intake air stream. This process introduces inert gases such as $CO_2$ and $H_2O$, which dilutes the air, reducing the percent of oxygen in the intake charge and increase the specific heat capacity of the intake mixture, lowering combustion temperatures and consequently reducing $NO_x$ formation [1]. Beyond temperature effects, EGR alters combustion kinetics and stability. Higher EGR rates reduce the intake oxygen concentration and slow the overall reaction rate, extending ignition delay and retarding combustion phasing [34]. Although moderate EGR levels can reduce $NO_x$, excessive EGR may increase combustion instability and limit load capability. This instability is typically quantified by the COV of the IMEP and COV of CA50[1], [35]. High EGR can elevate COV of IMEP, especially at low loads, while moderate levels can enhance stability at higher loads [36], [37].

The IMEP is a fundamental performance parameter representing the average pressure that, if it acted uniformly on the piston throughout the engine cycle, would produce the same indicated work as that measured from the actual pressure trace. It directly relates to the indicated work output of the cylinder and provides a normalized metric for engine load independent of displacement or speed [1]. In CI engines, IMEP is strongly influenced by the rate of heat release, combustion phasing, and in-cylinder pressure development. Combustion events that occur closer to TDC generally yield higher IMEP due to greater thermodynamic efficiency. however, overly advanced combustion can increase peak pressure and $NO_x$ emissions. Retarded combustion lowers peak temperature and $NO_x$ but reduces IMEP because a larger portion of the heat release occurs during the expansion stroke, resulting in lower work output [1].

The BSFC quantifies the fuel mass required to produce a unit of brake work and is a measure of combustion efficiency within the cylinder. It is typically expressed in grams of fuel per kilowatt-hour (g $kWh^{-1}$) and can be derived from the ratio of fuel mass flow rate to brake power output [1]. Lower BSFC values indicate more efficient combustion and reduced fuel consumption for a given load. Factors such as injection timing, EGR rate, and air–fuel mixing significantly influence BSFC. For example, increasing EGR often raises BSFC slightly due to lower combustion temperatures and slower reaction kinetics, which reduce thermal efficiency [38]. Likewise, excessively retarded injection timing can degrade fuel economy by shifting combustion too far into the expansion stroke.

The performance and emissions of CI engines are governed by a balance of fuel properties, combustion phasing, and charge conditions. Improved mixing and higher in-cylinder temperatures favor efficient combustion but promote $NO_x$ formation, whereas lower temperatures and oxygen-deficient regions favor soot formation. BSFC provides a

complementary measure of efficiency, representing the fuel mass flow rate per unit of brake power; reductions in BSFC signify improved fuel utilization and thermal efficiency. Optimizing variables such as fuel formulation (adopting oxygenated fuels like DME), injection timing, and EGR rate can reduce both $NO_x$ and PM emissions while maintaining comparable power levels. Together, these factors determine how modern CI engines operate and shape approaches for reducing emissions.

## 1.4 Research Objectives

The core objective of this research project is to determine the optimal operating conditions for low emissions and high efficiency of DME and study the relationship between $NO_x$ and PM that results. Exploration into reducing the soot-$NO_x$ tradeoff while maintaining diesel like power is an objective as well. This research project seeks to answer the following questions:

- What is the difference in PM and $NO_x$ emissions between diesel and DME at the same operating conditions?
- What is the optimal combustion phasing for DME to simultaneously reduce PM and $NO_x$?
- What is the optimal EGR rate for DME to simultaneously reduce PM and $NO_x$?

The following objectives are outlined below to help answer to those questions:

- Convert the John Deere 6068CI550 to a SCRE.
- Baseline test the John Deere SCRE on diesel.
- Convert the fuel system to DME to allow combustion and emissions comparisons against diesel baselines.

- Conduct injection timing sweeps on DME.
- Conduct EGR rate sweeps with DME.

This project is taking a testing approach to these objectives, by physically modifying an engine to run on DME and observing the changes. Results from this testing are included in Chapters 4 and 5. Chapter 4 includes validation of engine operating parameters on diesel. Chapter 5 contains all the results from the DME, fuel pressure sweeps, injection timing sweeps and EGR sweeps.

# CHAPTER 2: METHODS AND MATERIALS

## 2.1 Engine Test Cell and Controls

Testing for this research was conducted on a John Deere 6068CI550 diesel engine. The 6068CI550 is an industrial diesel engine designed to meet U.S Final Tier 4 emissions standards using split injection, EGR and variable injection pressure. An image of this engine test cell is shown in Figure 1, DME fuel system in Figure 2 and some basic engine information is shown in Table 1.

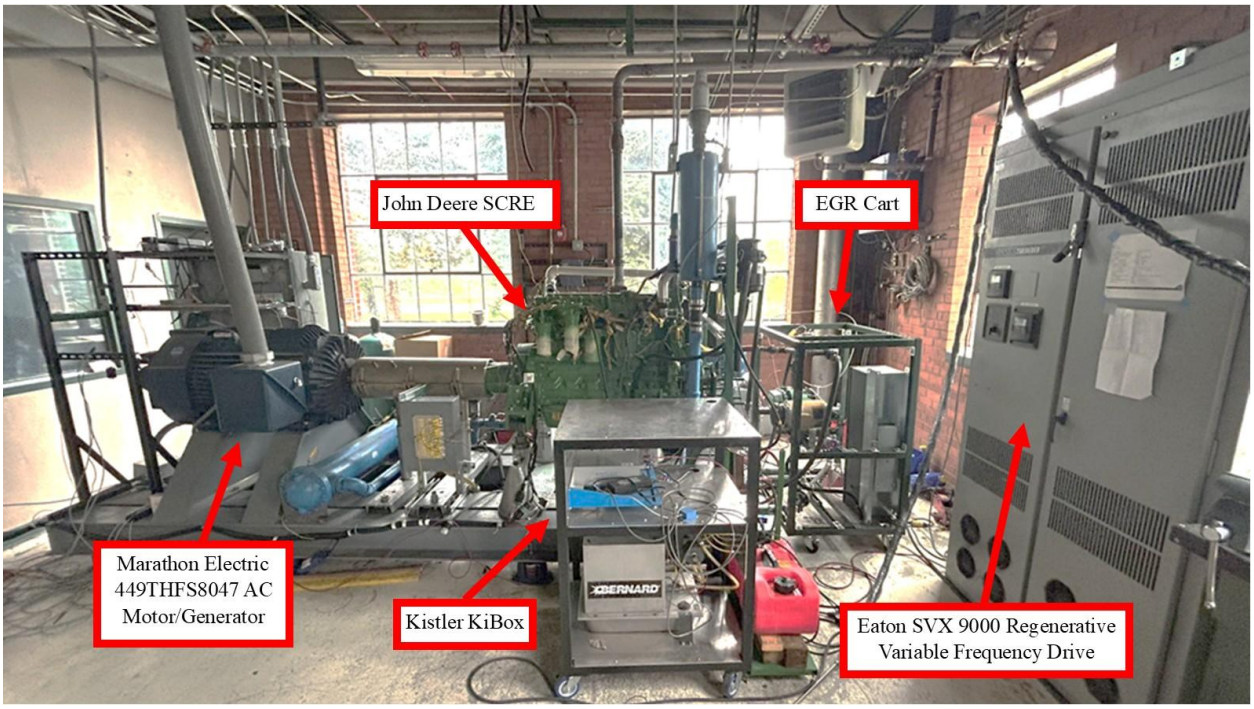


**Fig. 1.** John Deere 6068CI550 SCRE Test Cell

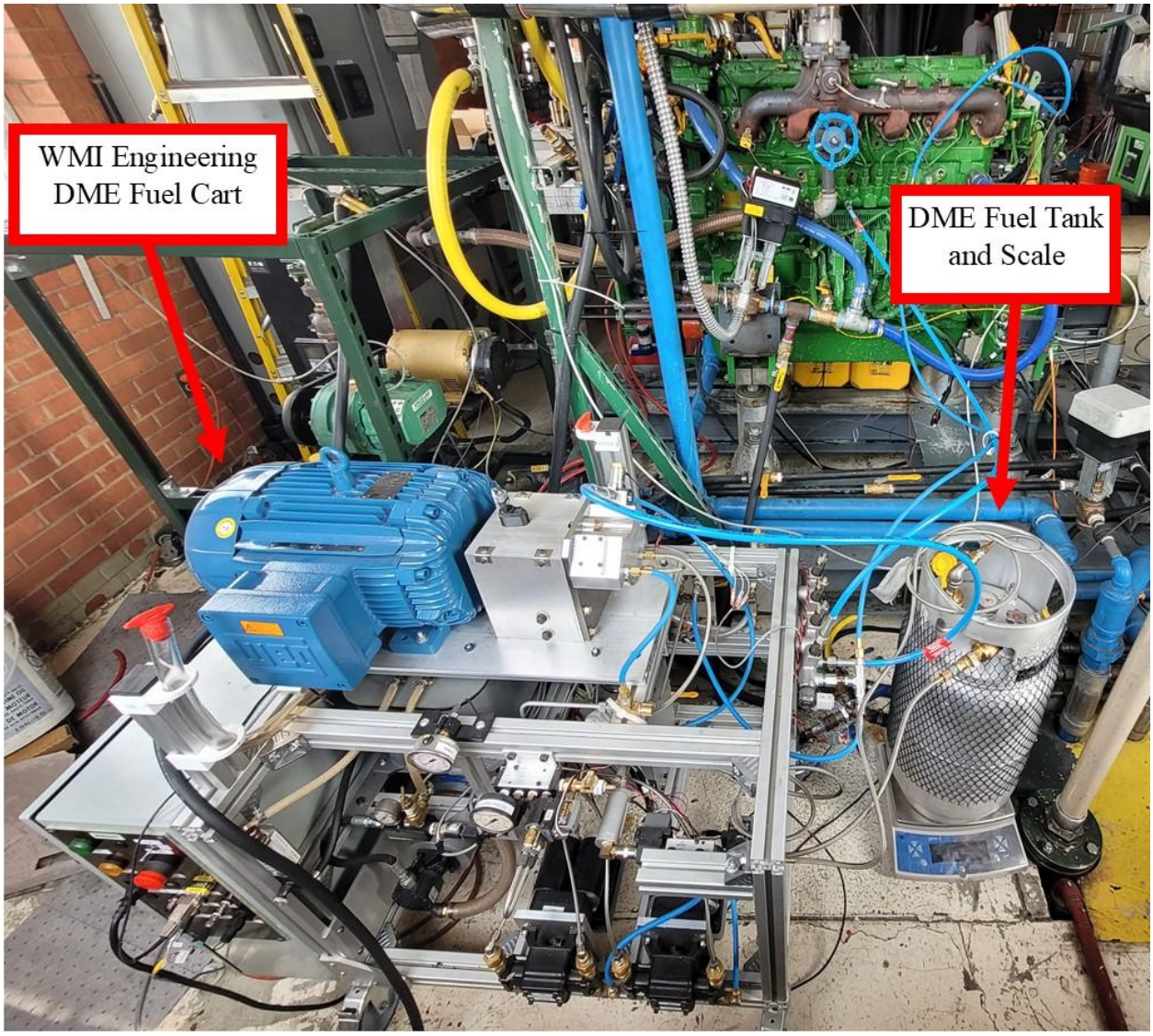


**Fig. 2.** DME Fuel System and Scale

**Table 1** Key specifications of test cell engine

| | |
|---|---|
| Engine Name | John Deere 6068CI550 |
| Engine Type | In-line, single cylinder, water cooled, four stroke |
| Bore | 106 mm |
| Stroke | 127 mm |
| Displacement | 6.8L |
| Compression Ratio | 16.7:1 |
| Rated Power | 224 kW |
| Rated Speed | 2400 rpm |
| Number of Valves | 4 |
| Fuel System | High Pressure Common Rail |
| Electronic Control Unit | L33 Controller |

For this study, the 6-cylinder engine was converted into a SCRE with a 1.13-liter displacement, corresponding to one-sixth of the total engine displacement. The engine is capable of operation up to 224kW at 2400 rpm in the stock, 6-cylinder configuration.

The test cell shown in Figure 1 uses a Marathon Electric 449THFS8047 AC motor/generator coupled to an Eaton SVX 9000 regenerative variable frequency drive (VFD). This system enables both motored operation and engine loading. The VFD provided closed-loop speed control, modulating the applied load to hold the engine at the commanded speed and supplying motoring power when combustion was absent.

The engine and motor are mounted on a rigid steel chassis with height adjustable mounts for alignment. Facility supplied water and compressed air provide cooling and intake air, respectively. The OEM flywheel and a custom adapter plate connect the engine to the driveshaft.

The cooling system was connected to an external water cooling/heating loop that allowed control of coolant temperature. This heat exchanger used water from the facility's cooling loop to

extract heat from the engine. A control valve varied cooling water flow as a function of engine coolant temperature to maintain an operating temperature of approximately 100 °C.

The engine's air intake used compressed dry air from the facility's air supply. The intake pressure could be varied up to 60 psig. The compressed air passed through an intake heat-exchanger system to simulate turbocharger outlet temperatures. A Woodward throttle valve, controlled through the LabVIEW system, then regulated the compressed air pressure to the desired intake pressure. The system also included an exhaust backpressure valve (Woodward GloTech) to simulate the effects of the turbocharger's exhaust turbine. Finally, the EGR cart pumped exhaust gases into the intake manifold, controlling EGR temperature and flowrate. A summary of the test cell configuration, including controllers and instrumentation, is shown in Figure 3.

Two fuel system configurations were utilized depending on the test fuel. During diesel operation, a dedicated fuel skid equipped with a 6-gallon tank, lift pump, fuel cooler, and scale for fuel consumption measurement. The low-pressure circuit interfaced with the John Deere fuel system at the stock low-pressure pump above one of the fuel filters, and the return line routed fuel from the manifold back to the tank through the cooler. A John Deere RE549641 800 cc injector was used for all diesel testing.

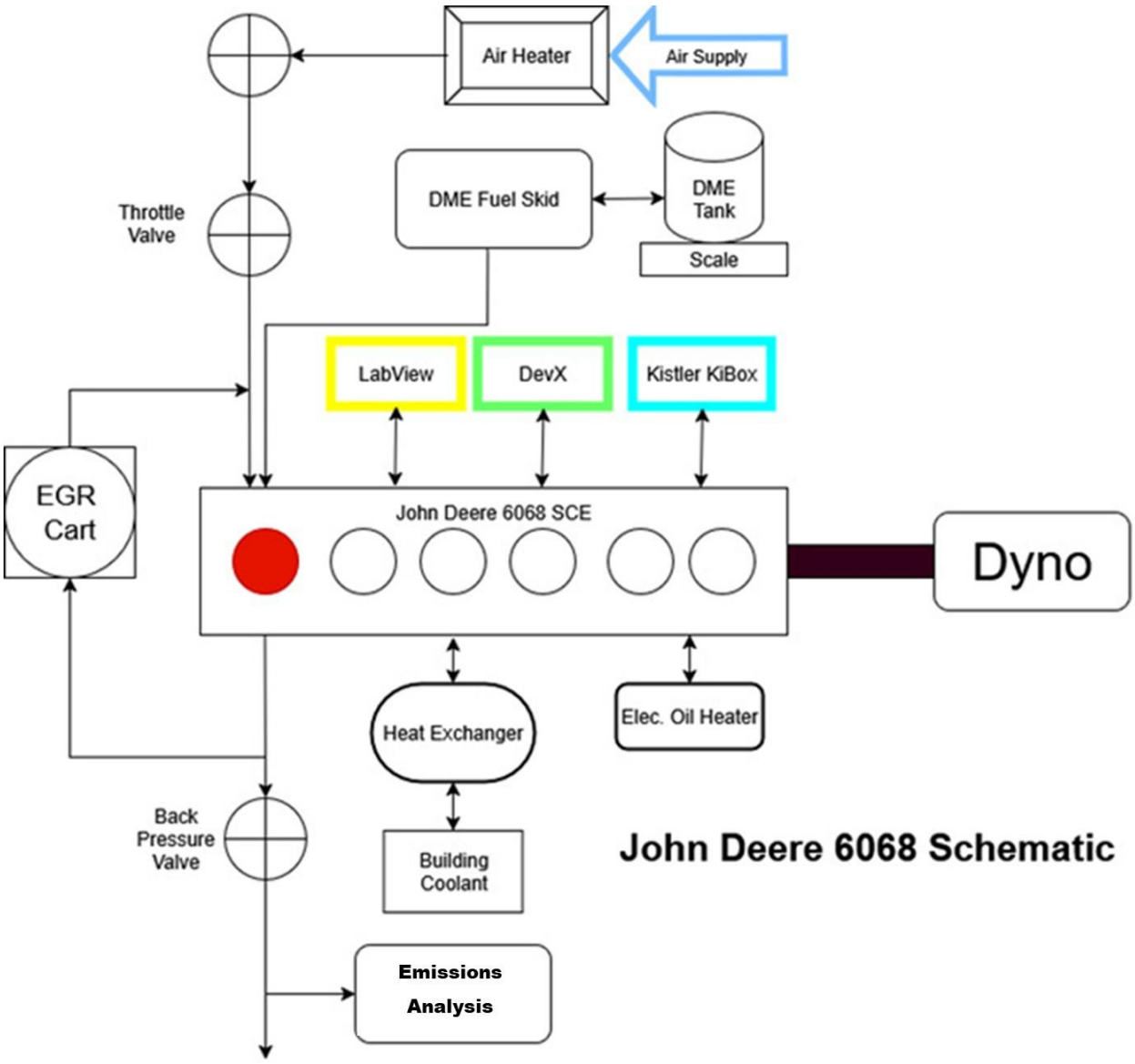


**Fig. 3.** Test cell schematic in the DME configuration.

For DME operation, a Flame King 33.5-lb propane cylinder served as the fuel reservoir and was mounted on a scale to determine mass flow. Low-pressure supply and return lines connected the tank to a DME fuel cart provided by WMI Engineering. The cart incorporated both low- and high-pressure pumps that operated in conjunction with the John Deere common rail pressure regulator to maintain the desired rail pressure. A John Deere RE550611 1000 cc injector was installed for all DME testing to provide the higher mass flow rates required.

An EGR test cart was used to supply variable, conditioned exhaust flow. Originally developed for a CFR engine and then later adapted for a Cummins X15 SCRE[39], the cart was modified with a John Deere RE535729 EGR heat exchanger to meet the requirements of the 6068CI550 SCRE. Exhaust gases from the high-pressure exhaust manifold port enter the cart, where gas temperature (typically 350–550 °C) are reduced using the John Deere air–water heat exchanger. The desired EGR gas temperature was specified by the user, and a LabVIEW-controlled valve (Honeywell ML7425A3013) adjusted coolant flow to achieve this condition.

Engine and test cell operation were controlled through two primary modules, the John Deere L33 controller and a National Instruments (NI) PXI-1050 chassis equipped with 6224 and 6704 modules. The NI-based data acquisition and control system operated through a custom LabVIEW virtual instrument that regulated throttle position, intake air pressure and temperature, exhaust backpressure, EGR rate, and dynamometer speed. This system provided low speed sampling for overall test cell control and monitoring, recording temperatures, pressures, and flow rates at 2 Hz.

The John Deere L33 controller was selected for this research because it enabled full control of the engine's fuel system. The L33 managed the Denso HP6 high pressure common rail system used for diesel operation, including rail pressure regulation and single or multiple injection events per cylinder referenced to TDC. The controller was compatible with multiple John Deere injector sizes and, being natively integrated with the test engine, provided a straightforward path toward potential DME fuel commercialization.

In-cylinder combustion was characterized using a Kistler KiBox system. The engine was instrumented with several Kistler in-cylinder pressure transducers and high-speed transducers on the intake and exhaust manifolds. These sensors provided crank angle resolved pressure data for

combustion analysis in cylinder one. A crankshaft encoder provided precise engine position and speed for signal synchronization. Using these inputs, the KiBox generated live pressure traces, apparent heat release, heat release rate, IMEP, peak pressure, peak pressure location, CA10-90, and CA50. Indicated power was computed from the in-cylinder pressure measurements and later converted to brake power using confidential mechanical efficiency data provided by John Deere. All pressure data were recorded at a resolution of 0.1 crank angle degrees.

## 2.2 Emissions Sampling

Emissions measurements were performed at both the intake and exhaust to quantify EGR rate, air–fuel ratio (AFR), and exhaust gas composition. Both intake and exhaust samples were routed through heated sampling lines to a remote emissions analyzer located in the control room. Exhaust gas was sampled from a port downstream of the exhaust throttle, while intake gas was sampled from a port in the intake elbow upstream of the intake runners.

A Siemens 600 Series 5-Gas Analyzer measured CO, $CO_2$, $NO_x$, $O_2$, and THC. An MKS MultiGas 2030 FTIR spectrometer quantified formaldehyde, DME, diesel, and speciated hydrocarbons up to $C_3$, as well as NO and $NO_2$ concentrations.

PM samples were collected from the exhaust using a heated sampling line to prevent condensation and loss of semi volatile material. The raw exhaust was diluted with conditioned building air to achieve a target dilution ratio appropriate for filter loading and to maintain temperatures suitable for PM collection. The diluted exhaust was then directed into a PM sampling cart equipped with a flow control system and a cyclone that removed larger particles and allowed collection of $PM_{2.5}$, defined as particles with an aerodynamic diameter of 2.5 micrometers or smaller. This ensured consistent sampling of fine particulate matter relevant to diesel and DME combustion.

PM was collected on a Teflon filter for gravimetric mass measurement and on a quartz fiber filter for carbon speciation. The PM collection and gravimetric analysis in this study were carried out following the procedures described by L'orange et al. 2021[40]. Gravimetric filters were equilibrated to the balance environment and weighed to a resolution of one microgram. Each filter was weighed at least three times, and measurements were accepted once successive readings agreed within five micrograms. After sampling, filters were again equilibrated and reweighed using the same procedure. The difference between the pre sampling and post sampling masses was used to calculate the collected PM mass.

Quartz filters were analyzed for OC and EC using a Sunset OC/EC analyzer following the thermal optical protocol outlined in the NIOSH 5040 method[41]. The analyzer heats the sample in defined temperature steps under inert and oxidizing atmospheres and determines OC and EC fractions based on the optical correction point where pyrolyzed carbon returns to baseline. This analysis provided quantitative measurement of carbonaceous PM composition, complementing the gravimetric mass measurements and enabling detailed assessment of particulate emissions across the operating conditions tested.

2.3, EGR Rate Determination

The rate of EGR is defined as the percent of intake mixture that is recycled exhaust gas. This is calculated on a mass basis through the ratio of EGR mass in the intake to the that of the mass of fresh air and fuel. This can be seen in equation 1 [1].

$$EGR\ Rate\ (\%) = \left(\frac{mEGR}{mFuel+mAir}\right)*100 \qquad (1)$$

The rate of EGR can also be determined from the ratio concentration of $CO_2$ in the exhaust and the concentration of the $CO_2$ in the intake. Desantes et al. 2010 and Jaffar et al. 2012 both used this method to determine EGR rate in their studies[42], [43].

$$EGR\ Rate\ (\%) = \left(\frac{[CO_2]_{int} - [CO_2]_{amb}}{[CO_2]_{exh} - [CO_2]_{amb}}\right) * 100 \qquad (2)$$

A further simplification can be made by assuming that the $CO_2$ present in the atmosphere is negligible which results in this simplification for EGR rate calculations by Zheng et al. 2004 [44].

$$EGR\ Rate\ (\%) = \left(\frac{[CO_2]_{int}}{[CO_2]_{exh}}\right) * 100 \qquad (3)$$

The simplified EGR rate calculation seen in equation 3 was used for EGR rate calculations in this study. The $CO_2$ concentrations were determined through emissions sampling ports on the intake and exhaust of the SCRE. The 5-gas emissions analyzer was used to determine the $CO_2$ concentration from these sampling ports.

## 2.4 Testing Procedure

A combination of the ISO 8178-4 C1 test cycle conditions and parameter sweeps was used for baseline diesel and DME testing.

The ISO 8178-4 C1 test cycle, commonly referred to as the 8-mode steady state test, is a standardized procedure used to evaluate gaseous and particulate emissions from nonroad diesel engines. It specifies discrete operating modes defined by combinations of engine speed and load. Emissions, reported in g $kWh^{-1}$, are calculated from steady state measurements of CO, THC, $NO_x$, and PM.

For this study, only modes 2, 3, and 7 of the C1 cycle were selected to represent typical mid-load and high-load operating regions. These modes were chosen based on tractor engine operating data provided by John Deere. Engine load was determined using IMEP based on guidance from John Deere. A live 200-cycle average IMEP reported by the Kistler KiBox was used during testing. A summary of the test plan is shown in Table 2.

**Table 2** Summary of Test Plan

| ISO 8178-4 C1 Test Cycle | Objective | Fuel | Engine Speed (rpm) | Load IMEP (bar) | EGR rate (%) | Injection Timing (deg BTDC) | CA50 (deg ATDC) |
|---|---|---|---|---|---|---|---|
| Mode 2 | Baseline | Diesel | 2200 | 8.6 | 22 | 2.3 | 21 |
| Mode 3 | Baseline | Diesel | 2200 | 6.84 | 24 | 5 | 20 |
| Mode 7 | Baseline | Diesel | 1600 | 7.29 | 22 | 3.5 | 16 |
| Mode 7 | Injection Sweep | DME | 1600 | 7.29 | 22 | -1,1,3,5,6,7,9,11,13 | 16 |
| Mode 7 | EGR Sweep | DME | 1600 | 7.29 | 22,25,30,40,50 | Variable | 16 |
| Mode 2 | Baseline Comparison | DME | 2200 | 8.6 | 22 | Variable | 16,21 |
| Mode 2 | Max EGR | DME | 2200 | 8.6 | 50 | Variable | 16,21 |
| Mode 3 | Baseline Comparison | DME | 2200 | 6.84 | 24 | Variable | 16,20 |
| Mode 3 | Max EGR | DME | 2200 | 6.84 | 50 | Variable | 16,20 |

At each test condition, key parameters such as exhaust pressure, intake temperature and pressure, coolant and oil temperatures, and EGR temperature were maintained at constant values, as summarized in Table 3.

**Table 3** Constant Operating Conditions

| | | Operating Condition | | |
|---|---|---|---|---|
| Parameter | Units | 1600rpm, 50% Load | 2200rpm, 50% Load | 2200rpm, 75% Load |
| Exhaust Pressure | bar (a) | 1.58 | 2.18 | 2.38 |
| Intake Pressure | bar (a) | 1.36 | 1.36 | 1.8 |
| Intake Temperature | °C | 50 | 50 | 55 |
| Coolant Temperature | °C | 99 | 99 | 99 |
| Oil Temperature | °C | 109 | 110 | 112 |
| EGR Temperature | °C | 104 | 110 | 117 |

In addition to the C1-cycle test points, parameter sweeps were conducted to characterize DME combustion behavior. Injection timing sweeps and EGR rate sweeps were performed while maintaining key operating parameters at constant values. Rail pressure was maintained at 135 MPa based on guidance from WMI Engineering. For both sweep types, IMEP was held constant by adjusting the injected fuel quantity per stroke. The resulting optimal CA50 from the injection timing sweeps was then held constant during the EGR sweeps. Additional boost was supplied at high EGR rates when increased fueling alone was insufficient to maintain IMEP.

# CHAPTER 3: SINGLE CYLINDER RESEARCH ENGINE CONVERSION

## 3.1 Background and Approach

Several approaches exist for converting multi-cylinder engines to SCRE. One method isolates a single cylinder for experimentation while the remaining cylinders continue to drive the engine[45]. Other approaches achieve complete cylinder deactivation by either preventing compression through piston modifications or by removing the cylinder head entirely[46]. Alternatively, the valve train of the deactivated cylinders can be disabled so that a fixed mass of air remains trapped in the inactive cylinders[47].

For the conversion of the 6068CI550 to a SCRE, the chosen approach was to deactivate the valve train for cylinders two through six, creating a fixed trapped air volume in each of the non-firing cylinders. This method followed standard practice recommended by John Deere.

The conversion process required removal of numerous engine components, including the turbochargers and associated piping, EGR cooler, EGR valve, throttle, starter, alternator, and intake manifold. Several components were replaced or modified for single cylinder operation. The coolant manifold, cylinder head, exhaust manifold, intake system, and oil pan were all replaced with custom single cylinder components. The injectors for cylinders two through six were disconnected to fully deactivate fuel delivery.

## 3.2 Cylinder Head

A custom cylinder head was designed and machined for converting the engine to a SCRE configuration. The head was machined at cylinder one to provide direct access to that cylinder's intake runner. The John Deere 6068CI550 uses a common plenum intake with cast runners

integrated into the head, making machining necessary to isolate cylinder one for SCRE operation.

The glow plug ports on cylinders one and six were originally machined to accept liquid cooled AVL QC34C pressure transducers for combustion pressure measurements. Due to availability constraints, adapters were later designed and machined to fit Kistler 6052C pressure transducers instead. Both transducers were mounted directly to the combustion chamber following Kistler's installation guidelines [48]. A second pressure transducer was added to cylinder one for redundancy. A Kistler 6052C transducer was installed through a cross-drilled passage machined into the head. The locations of both sensors and the adapter sleeve are shown in Figure 4.

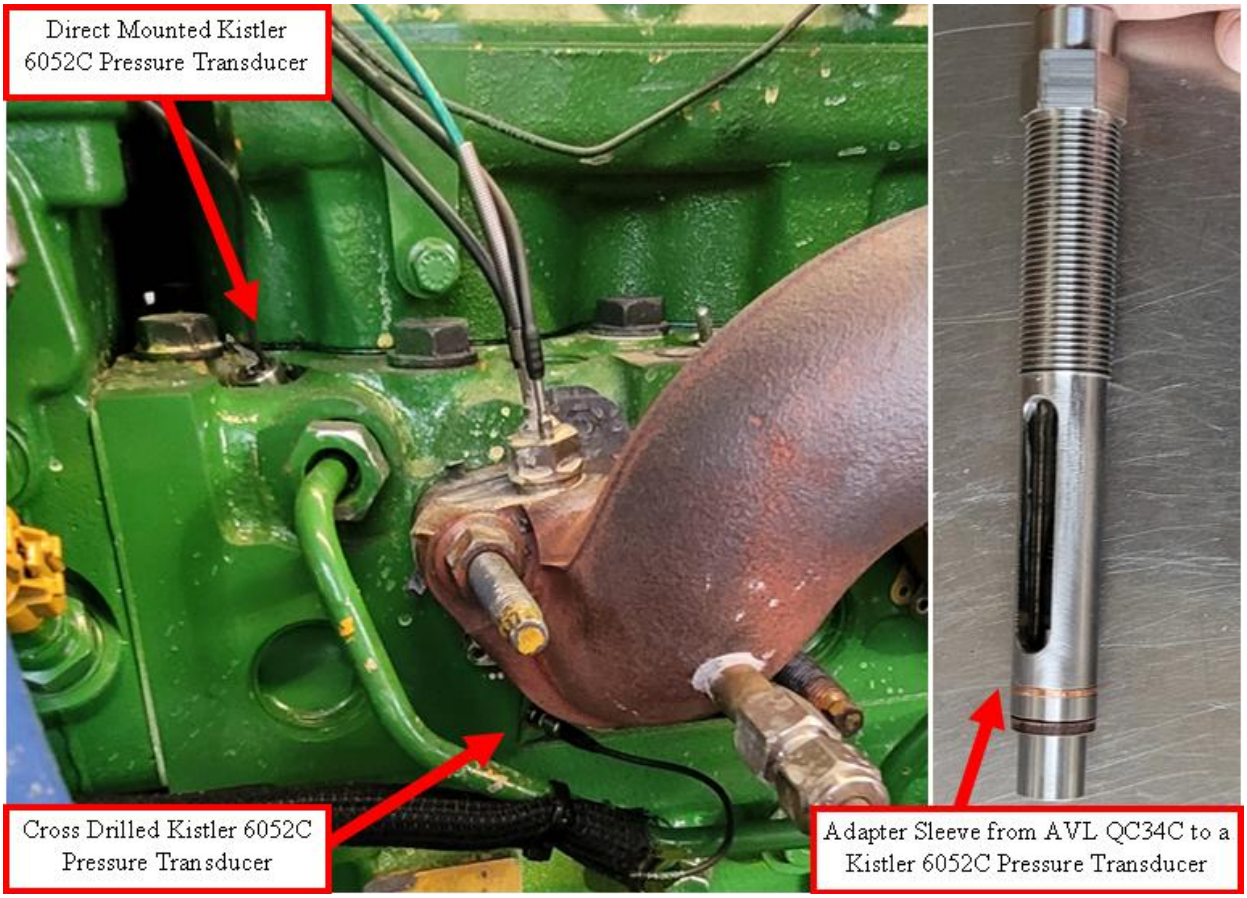


**Fig. 4.** Left: Location of the direct mounted and cross drilled pressure transducers. Right: Adapter from AVL pressure transducer to Kistler pressure transducer.

A custom intake elbow was fabricated, and modifications were made to the exhaust manifold to interface with the SCRE cylinder head, as shown in Figure 5. This intake elbow had three ports added. The first port was added to accept a K-type thermocouple with a 1/8-inch diameter probe. The second port was added to accept a Kistler Type 4007D dynamic pressure transducer. The final port was added to pull a gas sample from the intake for calculating lambda and EGR rate. The original exhaust manifold was modified by adding ports and block-off plates at the deactivated cylinders. The existing EGR port and high-pressure turbo port were retained. Custom plates were fabricated to mount a valve to the EGR port for regulating flow to the external EGR system, and to adapt the turbo port to the test cell exhaust system. The cylinder one exhaust runner was machined to accept a liquid cooled Kistler Type 4049B dynamic pressure transducer and a K-type thermocouple with a 3/16-inch probe.

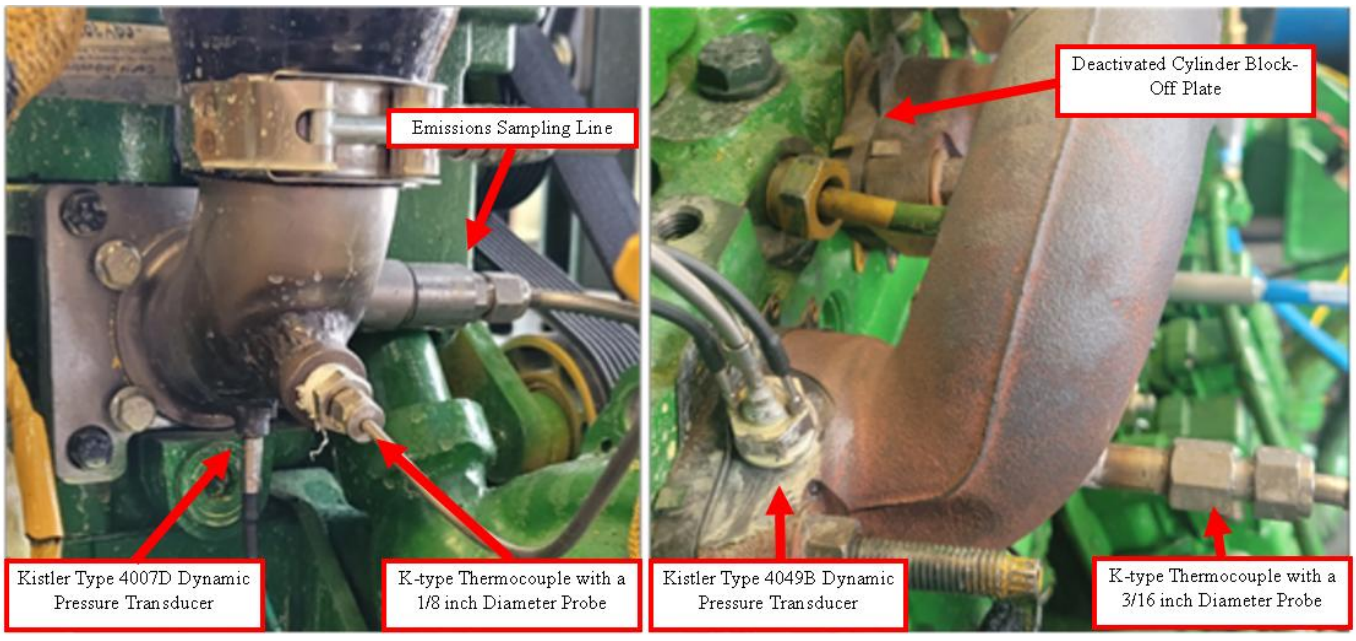


**Fig. 5.** Right: Location of high-speed pressure transducer, thermocouple and emissions sampling line on the intake. Left: Location of high-speed pressure transducer, thermocouple and block off plates.

3.3 Valve Train Deactivation

With the choice to use a trapped air cylinder deactivation method, the valve train needed to be deactivated on the unused cylinders. The John Deere 6068CI550 is a solid lifter pushrod engine with four valves per cylinder. Each intake–exhaust pair is actuated by a single rocker arm, as seen in Figure 6, with the rocker arms supported on a common shaft containing oil passage lubrication.

To deactivate the unused cylinders, the lifters, pushrods, rocker arms, and associated hardware were removed. To maintain proper oil pressure to the active cylinder-one valve train, custom rocker arm sleeves were designed and installed on the deactivated cylinders. The sleeves matched the spacing and tolerances of the OEM rocker arms, and one sleeve was used per deactivated cylinder, as seen in Figure 6.

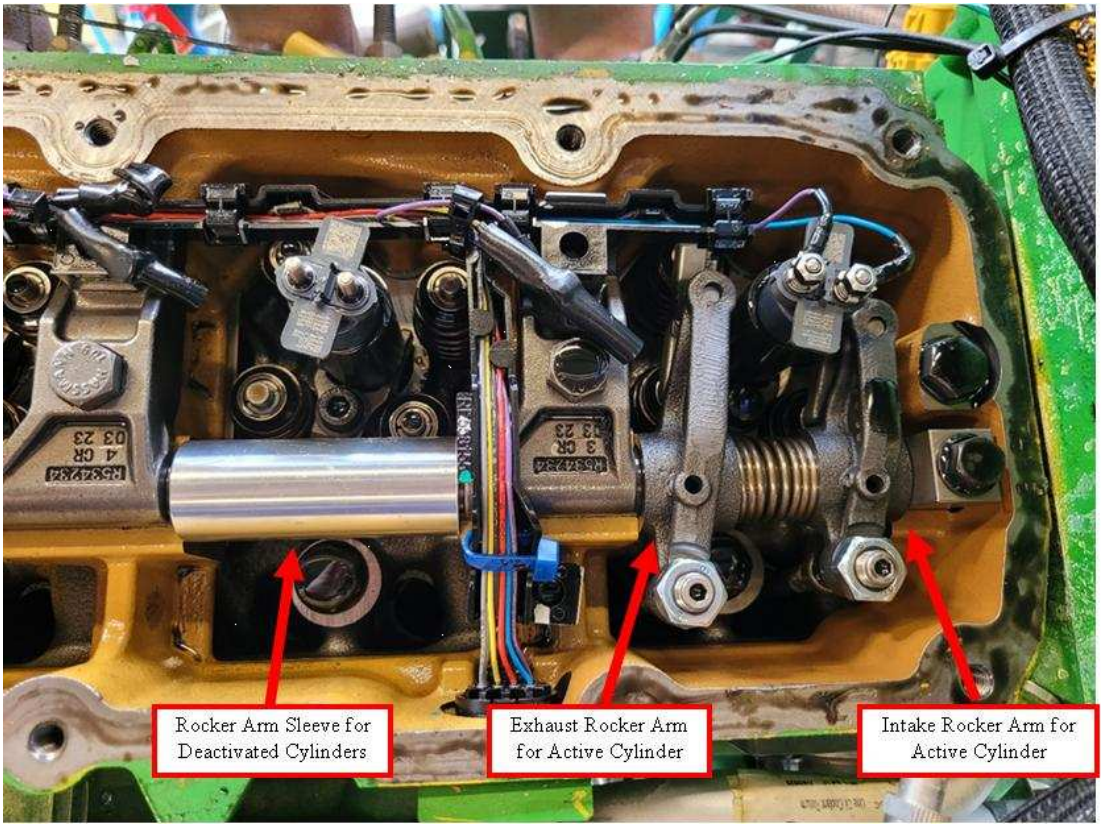


**Fig. 6.** Valvetrain configuration with rocker arm spacers for cylinders #2-#6.

The unused cylinders were fully sealed from the intake and exhaust once the valve train components were removed. The valve train configuration of cylinder one remained unchanged and installation of the custom sleeves-maintained cylinder one oil pressure.

### 3.4 Oil Pan, Coolant Manifold, Drive Belt and Block-Off Plates

Several systems required modification because SCRE operation involved removing or replacing numerous OEM components. Block off plates and fittings were fabricated for the starter, diesel high pressure fuel pump and turbocharger oil and coolant lines as seen in Figure 7.

A custom coolant manifold was machined to provide clearance for the SCRE intake manifold. This modification rerouted the oil cooler coolant line to avoid interference with the new intake geometry and removed the alternator mounting bracket, since the alternator had been eliminated earlier. These changes required installation of an alternative accessory drive belt to operate the water pump.

The OEM EGR cooler was removed because EGR for the SCRE was supplied by an external EGR cart. In the stock configuration, the EGR cooler circulates coolant from the cylinder head, through the cooler, and back to the coolant manifold via a dedicated thermostat. To maintain coolant distribution, a hose was installed to connect the cylinder head directly to the coolant manifold in place of the EGR cooler.

Running the engine on a single cylinder reduces its heat output to one-sixth of the full 6-cylinder engine. To maintain the same fluid temperatures for oil and coolant as the 6068CI550 would have during 6-cylinder operation, a heating element was added to the block coolant passages and the oil pan. The oil pan was modified to integrate a 4500-Watt Watlow BLS724N5S heating element by welding a bung into the front of the pan and removing internal ribbing. A John Deere RE539167 block heater capable of supplying 1000 W at 120 V was also added to reduce warm up

time and help maintain test ready temperatures. Both heating elements can be seen in Figure 8.

3.5 Instrumentation and Measurement Systems

Engine combustion measurements were synchronized to crank angle position using a BEI H25 rotary encoder with 3600 pulses per revolution (7200 pulses per engine cycle). This required modification of the harmonic balancer to machine an alignment surface inside its central cavity.

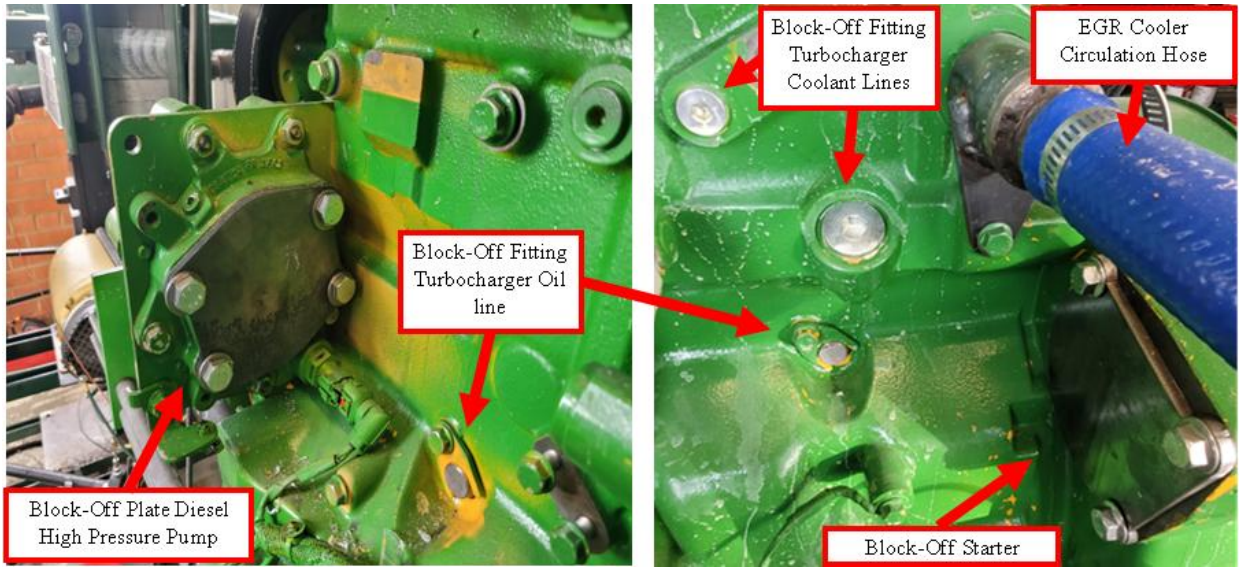


**Fig. 7.** Right: High pressure diesel pump block-off plate for DME operation and turbocharger oil line block-off fittings. Left: Starter block-off plate, turbocharger coolant line block-offs and EGR cooler circulation hose.


**Fig. 8.** Right: Block heater placement on rear of engine. Left: Heating element placement in oil pan.

A custom adapter plate was machined to utilize existing balancer bolt holes and center itself on the newly machined alignment surface. The adapter included a 3/8-inch extrusion that coupled to the encoder through a flexible collar coupling. The encoder was supported in axial alignment with the crankshaft using a ½-inch steel mounting plate and a sandwich style alignment system. Threaded rods, vibration resistant flange nuts, and machined standoff pins were used to rigidly support the plate parallel to the harmonic balancer. The encoder mounting assembly can be seen in Figure 9.

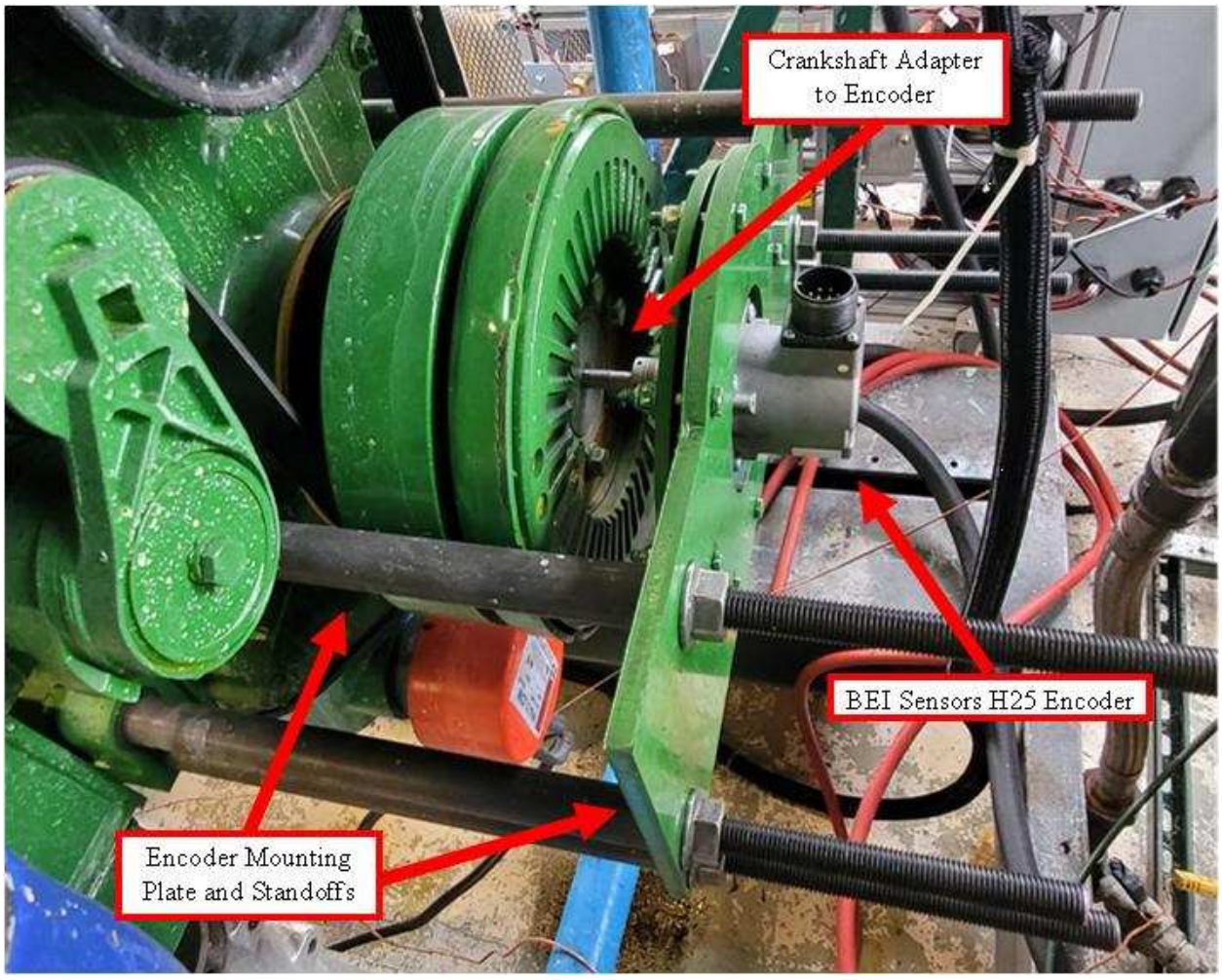


**Fig. 9.** Encoder mounting assembly, crank shaft adapter, and encoder location.

## 3.6 Control Systems Modifications

The SCRE conversion removes many components, prompting the OEM controller to detect faults and trigger derates or diagnostic codes. To avoid this, external control of the engine management system was required. The John Deere DevX software was used to override diagnostic limits and derates, allowing direct adjustment of fueling related parameters.

As described in Chapter 2, engine and test cell control were divided between the John Deere L33 controller and a LabVIEW based NI system. The L33 controller managed the full diesel fuel system and controlled injection timing and rail pressure for both diesel and DME operation. Real time adjustments were made using a John Deere Service Advisor EDL V2 data link in conjunction with DevX. DevX enabled modification of calibration tables and fixation of specific operating parameters including injection timing, injection count, fuel quantity, and rail pressure to maintain stable experimental conditions.

For experimental sweeps, certain parameters were fixed to minimize cycle to cycle and test to test variability. Fueling modes determine which variables the controller uses for closed loop control (e.g., speed vs. torque), while operation modes determine behavior with respect to boundary conditions such as coolant temperature. For all experiments, the engine operated in torque based fueling mode and in Control Mode 15 (Normal Operation), with injection timing, injection count, fuel quantity, and rail pressure held fixed.

Additional DevX modifications were required for DME fueling. Because DME has approximately 68% of the lower heating value of diesel, injection durations were significantly longer at a given rail pressure. The standard L33 safety limits derated fueling when duration

approached calibrated thresholds, which occurred frequently with DME. To prevent derating, the maximum fueling duration limit was doubled.

The diesel injection duration table which maps commanded fuel quantity (mg/stroke) and rail pressure to injection duration (μs) was replaced with a DME specific table provided by WMI Engineering, who designed the DME fuel cart. Although precise accuracy of the table was not critical (since IMEP targeting was achieved through external fuel flow measurements), the updated table improved controller behavior during DME operation.

Additional DevX adjustments supported SCRE operation and dynamometer based starting. Because the engine was coupled to a motor–generator dynamometer, the OEM starter motor was not used. Instead, the dynamometer accelerated the engine to cranking speed while DevX held fueling at zero. Once the engine reached the target speed, fueling was enabled. For single-cylinder operation, zero fuel was commanded to cylinders two through six, and multiple injection events were disabled to support the single injection combustion strategy.

# CHAPTER 4: DME-DIESEL COMPARISON AT BASELINE OPERATING CONDITIONS

The baseline testing defines the initial performance condition of the SCRE on diesel and helps to compare it to the performance of the SCRE on DME. Modes 2, 3, and 7 from the ISO 8178-4 C1 test cycle were chosen as operating points for baseline testing. No parameter sweeps were conducted for baseline testing. Brake specific emissions and combustion characterizations were used to baseline the diesel SCRE performance to compare to DME.

## 4.1 Combustion Parameters

Baseline diesel and DME combustion is shown in Figures 10 through 15 using cycle averaged in-cylinder pressure and AHRR. The comparison evaluates combustion behavior across the three baseline operating points using a common set of parameters: SOI-CA5, CA50, CA10–90, peak pressure, the crank angle location of peak pressure, maximum AHRR and location of maximum AHRR. Each condition was run according to the procedures outlined in Chapter 2, Section 2.4, Table 2, with injection quantity and timing fixed for diesel, and with CA50, EGR rate, and IMEP matched to the diesel baseline for DME. The resulting diesel combustion parameters are summarized in Table 4, and the corresponding DME results are presented in Table 5. Using identical metrics for both fuels provides a consistent basis for comparing combustion phasing, heat release duration, and pressure development under matched operating conditions.

All in-cylinder pressure traces and AHRR plots presented in this study represent cycle averaged combustion data computed from 1600 consecutive engine cycles at each operating condition. This cycle count was selected to ensure stable averaging and consistent comparison between fuels. The AHRR traces exhibit some noise in the signal. To mitigate this effect while

preserving the shape and timing of the heat release features, a moving average smoothing window of 5 points was applied to all AHRR curves.

Figure 10 shows diesel combustion at 1600 rpm and 50% load. The AHRR trace shows two main stages of diesel combustion. The initial sharp spike in heat release immediately after ignition corresponds to the premixed phase, where fuel that accumulated during the ignition delay burns very rapidly. This is followed by a longer, gradual decline in AHRR that reflects the diffusion-controlled phase, during which fuel continues to burn as it mixes with air. Phasing markers for SOI, CA5, CA50 and CA10–90 identify the key stages of combustion.

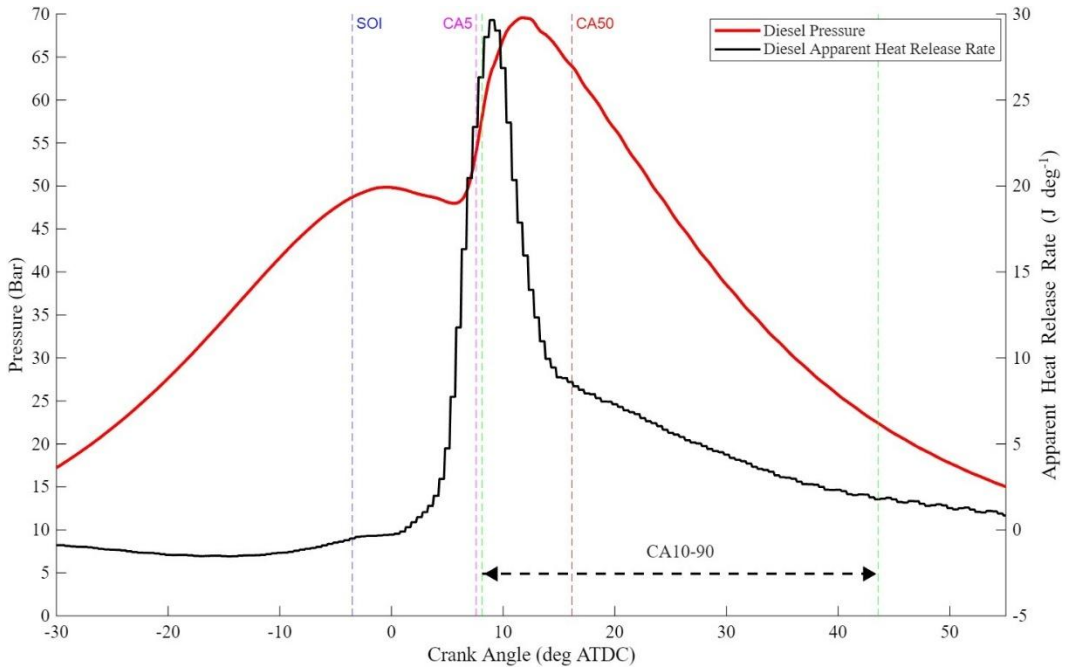


**Fig. 10.** Diesel average pressure trace and apparent heat release rate 1600 rpm 50% load

Figure 11 presents DME combustion at 1600 rpm and 50% load. The AHRR trace for DME displays a broad and low magnitude heat release profile. The absence of a sharp initial spike indicates that only a small fraction of the fuel accumulates prior to ignition. This produces a smoother rise in cylinder pressure and a reduced pressure rise rate compared to diesel, even though CA50 is matched between the fuels.

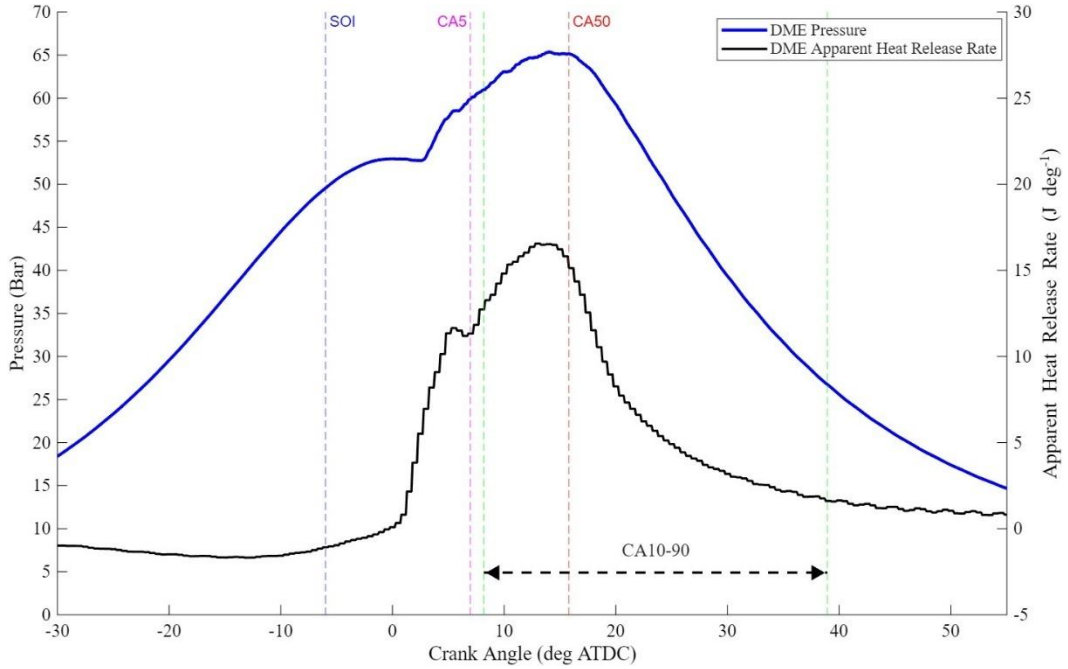


**Fig. 11.** DME average pressure trace and apparent heat release rate 1600 rpm 50% load

Figure 12 shows diesel combustion at 2200 rpm and 50% load. The AHRR curve exhibits a distinct, sharp premixed spike immediately after ignition, followed by a long diffusion controlled tail. The premixed spike remains prominent at this operating point, indicating that a significant portion of the fuel accumulates during ignition delay before rapidly burning. The pressure trace reflects this behavior through a steep pressure rise and an early peak near TDC. The diffusion phase proceeds over a longer crank angle interval, visible in the gradual tapering of the AHRR trace.

Figure 13 presents DME combustion at 2200 rpm and 50% load. The AHRR curve shows a broader, lower magnitude heat release profile compared to diesel, with no sharp premixed spike. This shape indicates that only a small amount of fuel accumulates prior to ignition, resulting in a more gradual premixed burn followed by an extended, evenly distributed heat release period. The pressure trace mirrors this behavior through a smoother rise to peak pressure and a noticeably reduced pressure rise rate, even though CA50 is matched to diesel.

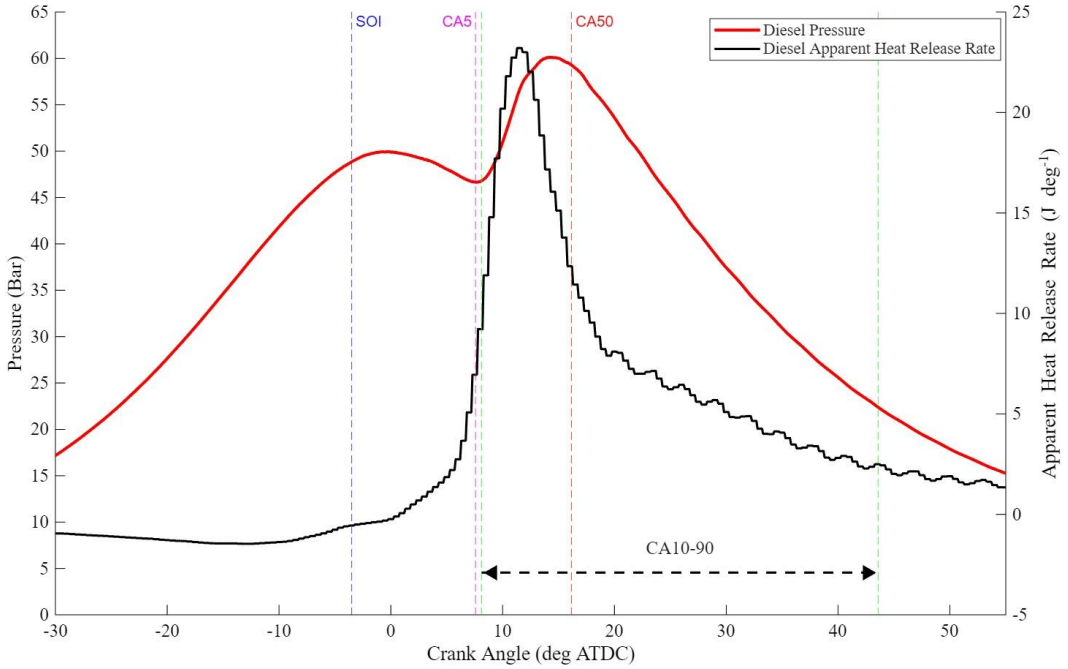


**Fig. 12.** Diesel average pressure trace and apparent heat release rate 2200 rpm 50% load

Figure 14 shows diesel combustion at 2200 rpm and 75% load. SOI is very close to TDC, which contributes to the small dip in the pressure trace shortly before the main pressure rise as the piston transitions into expansion. The AHRR curve shows a double peak structure where an initial sharp premixed heat release peak followed by a second, broader peak associated with the transition into mixing controlled combustion. After this second peak, the AHRR decays gradually over a wide crank angle range into a diffusion burn phase.

Figure 15 shows DME combustion at 2200 rpm and 75% load. The pressure trace shows a smooth rise to peak pressure, with no abrupt changes near top dead center. The AHRR profile exhibits a broad, rounded heat release peak followed by an extended, gradually declining tail. Unlike diesel at this same operating point, the AHRR does not display a distinct premixed spike or double peak structure. Heat release is instead spread more uniformly over the crank angle domain.

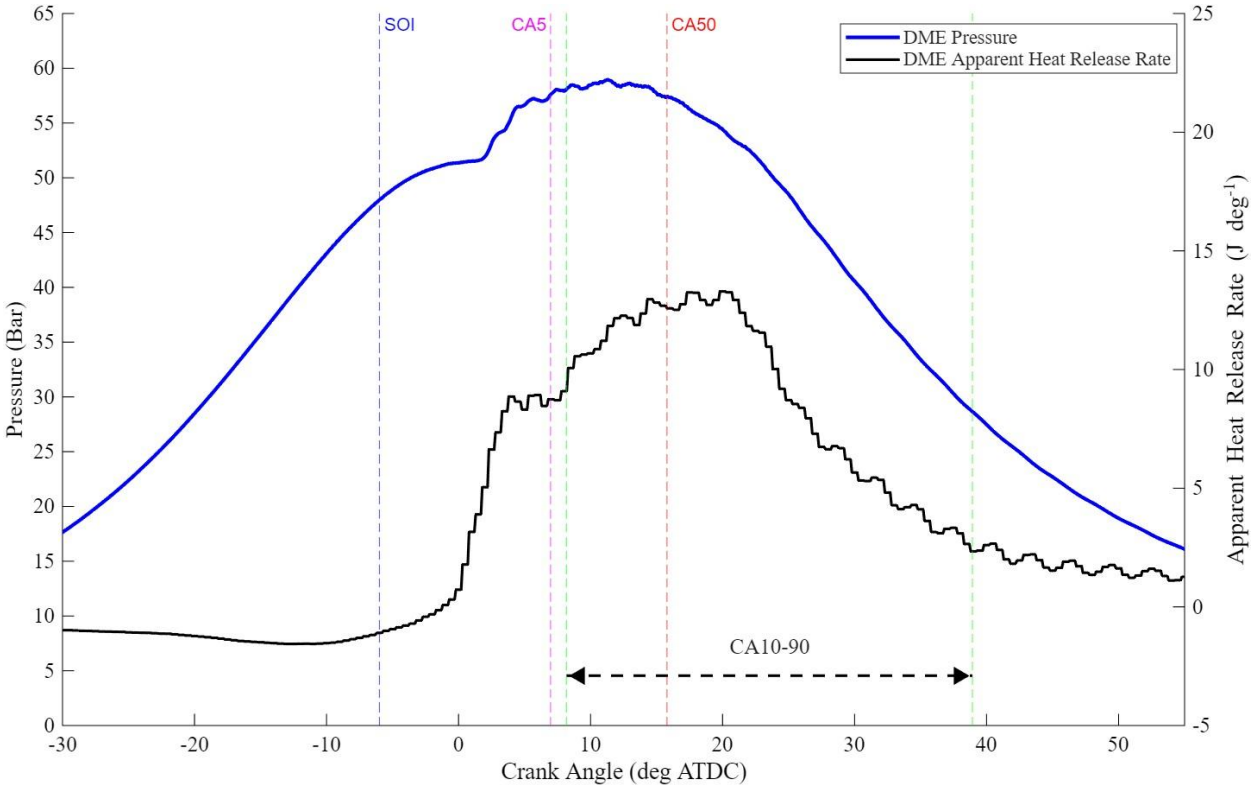


**Fig. 13.** DME average pressure trace and apparent heat release rate 2200 rpm 50% load

The combustion parameter results from diesel and DME baseline testing are presented in Table 4 and 5, respectively. Across all conditions, DME operated with a consistently shorter combustion duration than diesel, as indicated by lower CA10–90 values. SOI–CA5 also differed between the fuels, with DME exhibiting longer SOI-CA5, reflecting later start of combustion relative to injection. Peak pressure trends varied with operating condition. At 1600 rpm and 2200 rpm under 50% load, DME produced lower peak pressures than diesel, while at 2200 rpm and 75% load, DME reached a higher peak pressure. The location of peak pressure showed similar variation. At 1600 rpm and 50% load, DME's peak pressure occurred about 2 deg ATDC later than diesel; at 2200 rpm and 50% load, DME peaked roughly 2 deg ATDC earlier; and at 2200 rpm and 75% load, DME's peak pressure occurred substantially earlier, by approximately 6 deg ATDC. Maximum AHRR values were lower for DME at all shared operating conditions, consistent with its broader and more gradual heat release profile. The crank angle location of the

maximum AHRR occurred later for DME at 1600 rpm, but earlier at the two 2200 rpm points, with the largest shift at 2200 rpm and 75% load, where the DME heat release peak occurred more than 5 deg ATDC ahead of the diesel case.

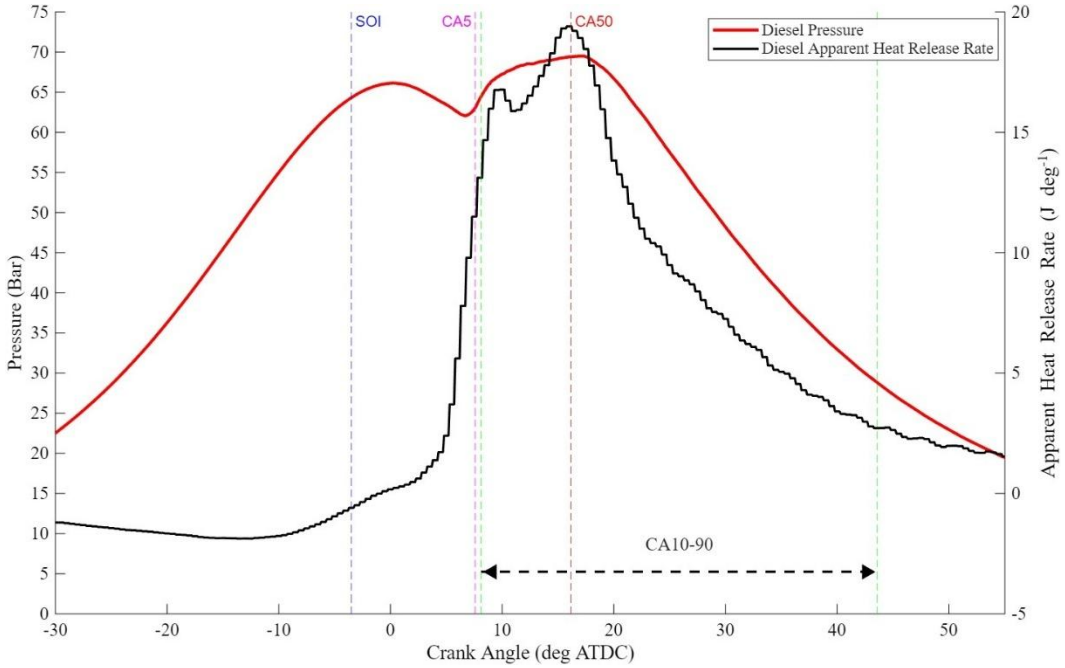


**Fig. 14.** Diesel average pressure trace and apparent heat release rate 2200 rpm 75% load

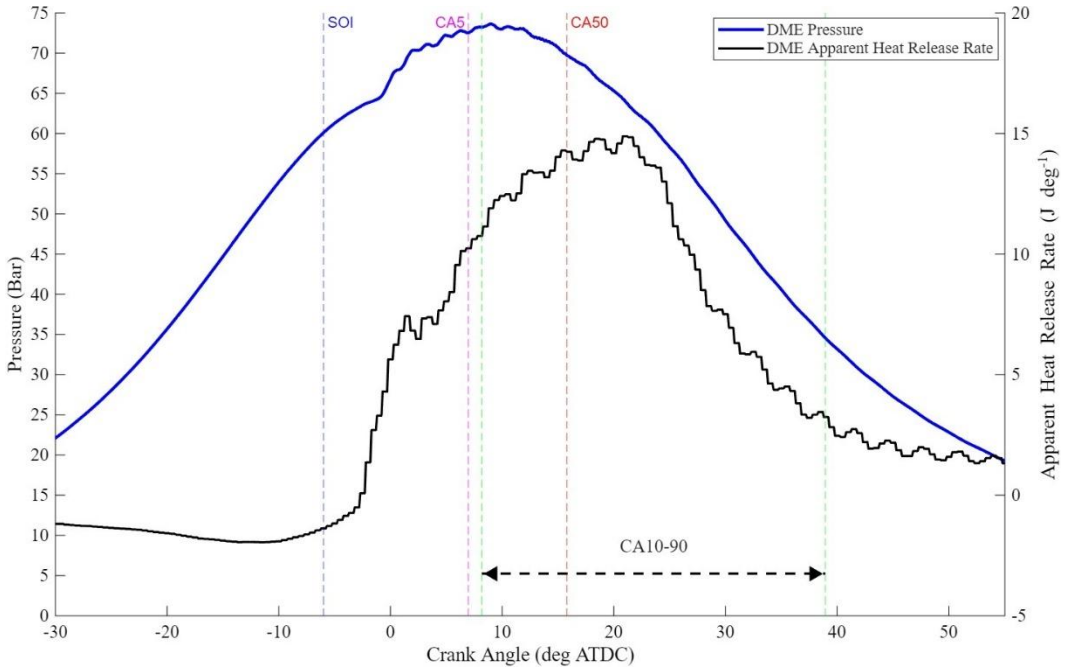


**Fig. 15.** DME average pressure trace and apparent heat release rate 2200 rpm 75% load

Table 4 Diesel Baseline Combustion Parameters

| | | Diesel Operating Condition | | |
|---|---|---|---|---|
| Parameter | Units | 1600rpm, 50% Load | 2200rpm, 50% Load | 2200rpm, 75% Load |
| SOI-CA5 | deg | 11.08 | 15.05 | 11.94 |
| CA50 | deg ATDC | 16.17 | 19.96 | 20.80 |
| CA10-90 | deg | 35.46 | 38.27 | 37.86 |
| Peak Pressure | bar (a) | 73.60 | 63.56 | 69.04 |
| Location of Peak Pressure | deg ATDC | 12.31 | 12.96 | 15.23 |
| Peak AHRR | J $deg^{-1}$ | 29.65 | 23.21 | 19.40 |
| Location Peak AHRR | deg ATDC | 8.80 | 11.30 | 15.80 |

Table 5 DME Combustion Parameters

| | | DME Operating Condition | | |
|---|---|---|---|---|
| Parameter | Units | 1600rpm, 50% Load | 2200rpm, 50% Load | 2200rpm, 75% Load |
| SOI-CA5 | deg | 12.97 | 17.20 | 17.79 |
| CA50 | deg ATDC | 15.79 | 20.05 | 20.37 |
| CA10-90 | deg | 30.76 | 34.34 | 33.39 |
| Peak Pressure | bar (a) | 66.16 | 59.88 | 74.49 |
| Location of Peak Pressure | deg ATDC | 14.33 | 11.13 | 9.30 |
| Peak AHRR | J $deg^{-1}$ | 16.55 | 13.29 | 14.89 |
| Location Peak AHRR | deg ATDC | 12.80 | 19.80 | 20.80 |

4.2 Emissions and Efficiency Comparison

Emissions and efficiency comparisons for diesel and DME are presented in Figures 16 through 23. The fuels are evaluated using Brake specific emissions of CO, THC, $NO_x$, and PM, as well as Brake specific fuel consumption and thermal efficiency. These metrics provide a direct, side by side assessment of fuel performance under matched combustion phasing conditions, where CA50, EGR rate, and IMEP are held constant between diesel and DME.

Figure 16 presents Brake specific carbon monoxide (BSCO) emissions, where diesel exhibits substantially higher CO formation at all operating conditions. The greatest disparity occurs at 2200 rpm 50% load, where diesel CO exceeds DME by more than a factor of two. This result is consistent with DME's inherent oxygen content, which promotes more complete oxidation and reduces CO formation under comparable combustion phasing.

Brake specific nitrogen oxides ($BSNO_x$) emissions are shown in Figure 17. Under matched CA50 and EGR rates, DME produces lower $NO_x$ than diesel. The difference is most notable at 2200 rpm 50% load, where diesel generates the highest $NO_x$ level in the baseline set. This suggests that diesel maintains higher local temperatures during combustion, whereas the lower flame temperature and faster vaporization rate of DME reduce thermal $NO_x$ formation in this regime.

Brake specific particulate matter (BSPM) emissions for both fuels are reported in Figure 18. DME demonstrates a dramatic reduction in PM across all operating conditions, aligning with its lack of C–C bonds and near soot free combustion properties. Although PM increases with load for both fuels, the increase is far less pronounced for DME, suggesting that load driven enrichment plays a minimal role in particulate formation when fuel bound oxygen is present.

Figure 19 further resolves DME particulate emissions into OC and EC fractions. More than 95% of measured PM mass for all operating conditions is OC, indicating that emissions are dominated by volatile hydrocarbons rather than soot. This confirms that particulate formation is governed by fuel and oil vaporization rather than accumulation of carbon based particulate matter commonly formed in diesel combustion. A comparable diesel reference study reported PM compositions with significant EC as shown in Figure 20 [49].

Figure 20 illustrates the PM composition for a 4-cylinder John Deere 4045 Tier 3 CI engine operating at Mode 4 of ISO 8178 (50% torque at 1700 rpm). This engine and operating point closely align with those used in this study, providing relevant insight into diesel PM composition. Nearly half of the PM mass from ULSD consists of EC, indicating a high proportion of soot. In contrast, DME PM contained less than 5% EC[49]. This stark difference demonstrates that diesel PM is predominantly soot based, whereas DME produces minimal soot even under comparable conditions.

Brake specific total unburned hydrocarbons (BSTHC) emissions are shown in Figure 21, follow a trend similar to PM. DME THC remains lower at all operating points, increasing moderately with load in a manner comparable to diesel.

BSFC results shown in Figure 22, show that DME requires higher mass-based fuel flow due to its lower LHV. Despite this increase, the BSFC trend for DME closely mirrors that of diesel, with both fuels peaking at 2200 rpm and 50% load. This demonstrates that the primary driver of BSFC differences is fuel energy density rather than combustion efficiency.

Figure 23 compares thermal efficiency. At 1600 rpm 50% load, diesel and DME operate at nearly identical efficiency values. At the higher-speed conditions, diesel shows a slight efficiency advantage. Overall, the similarity in efficiency confirms that DME can operate with diesel equivalent combustion phasing without significant thermal efficiency penalty.

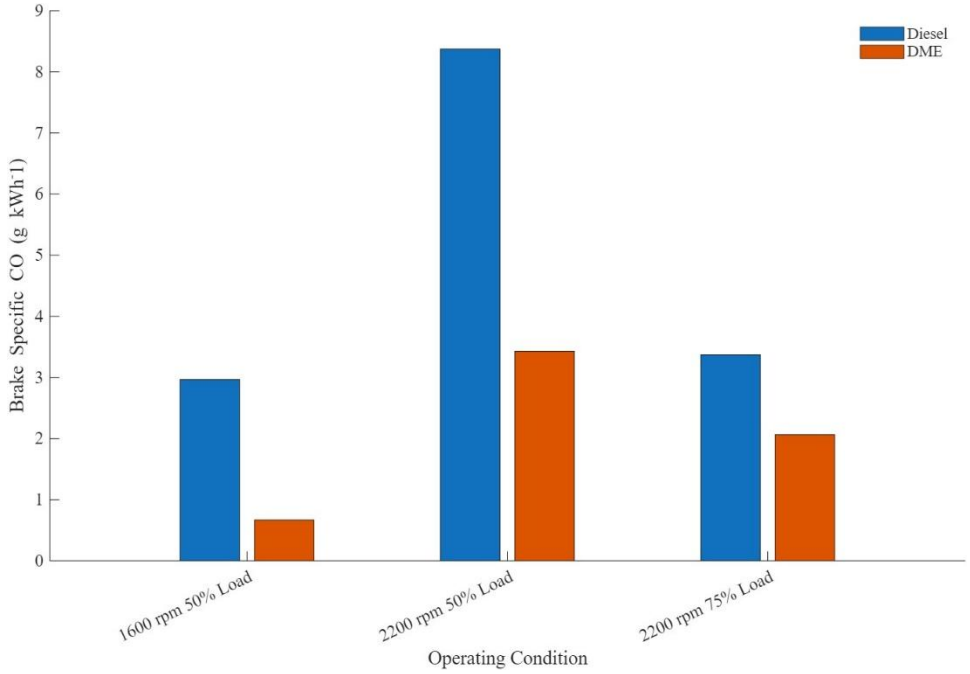


**Fig. 16.** Brake specific carbon monoxide emissions for diesel and DME

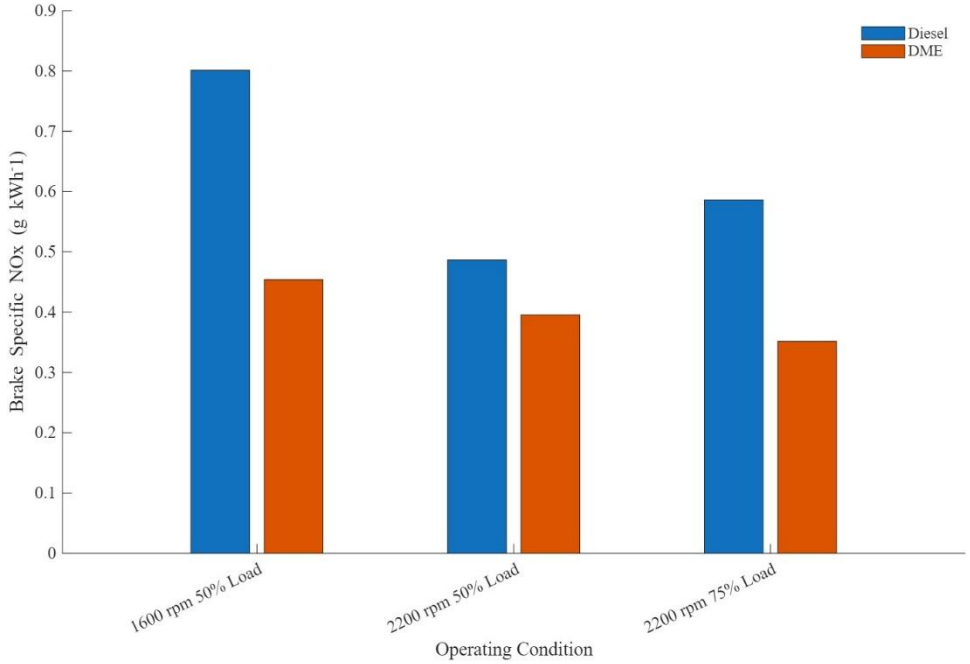


**Fig. 17.** Brake specific nitrogen oxides emissions for diesel and DME

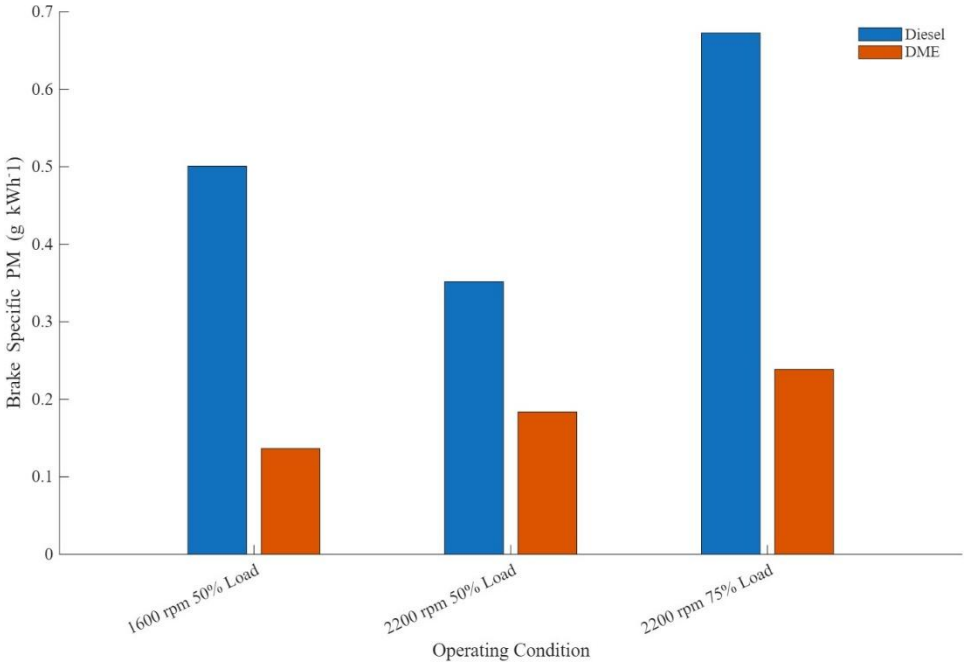


**Fig. 18.** Brake specific particulate matter emissions for diesel and DME

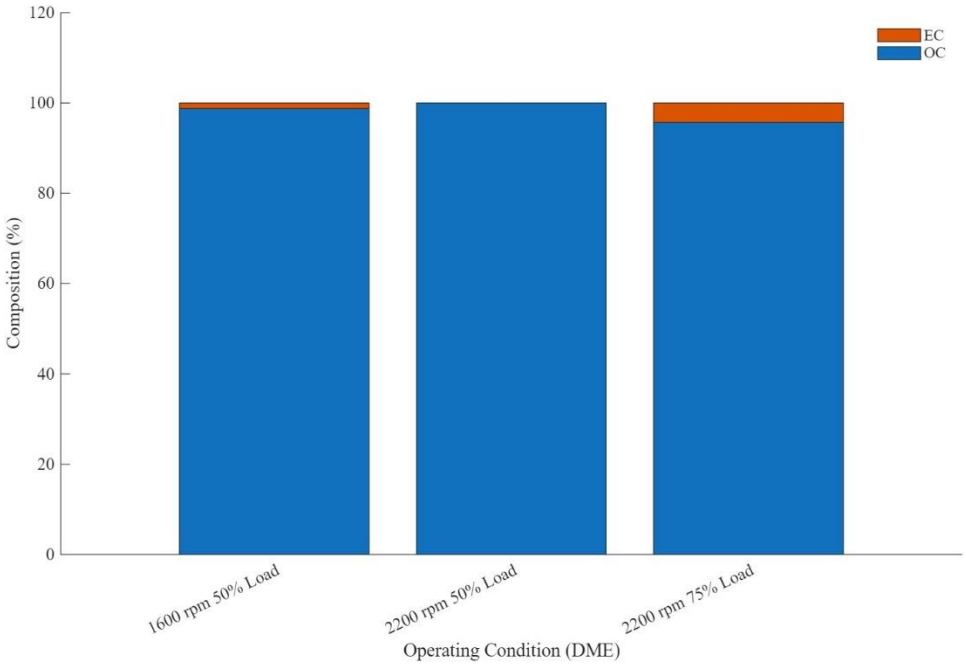


**Fig. 19.** Composition of DME Brake specific particulate matter emissions between organic and elemental carbon

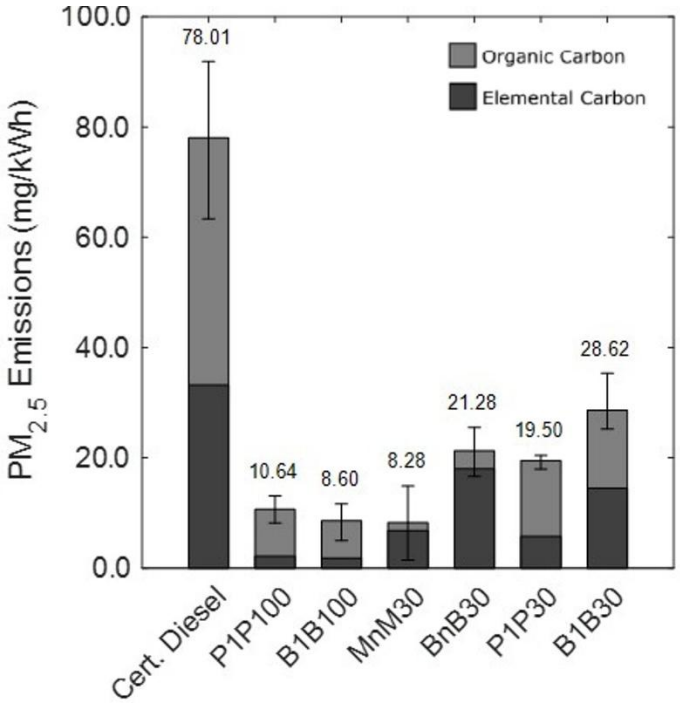


**Fig. 20.** Composition of diesel brake specific particulate matter emissions between organic and elemental carbon [49]

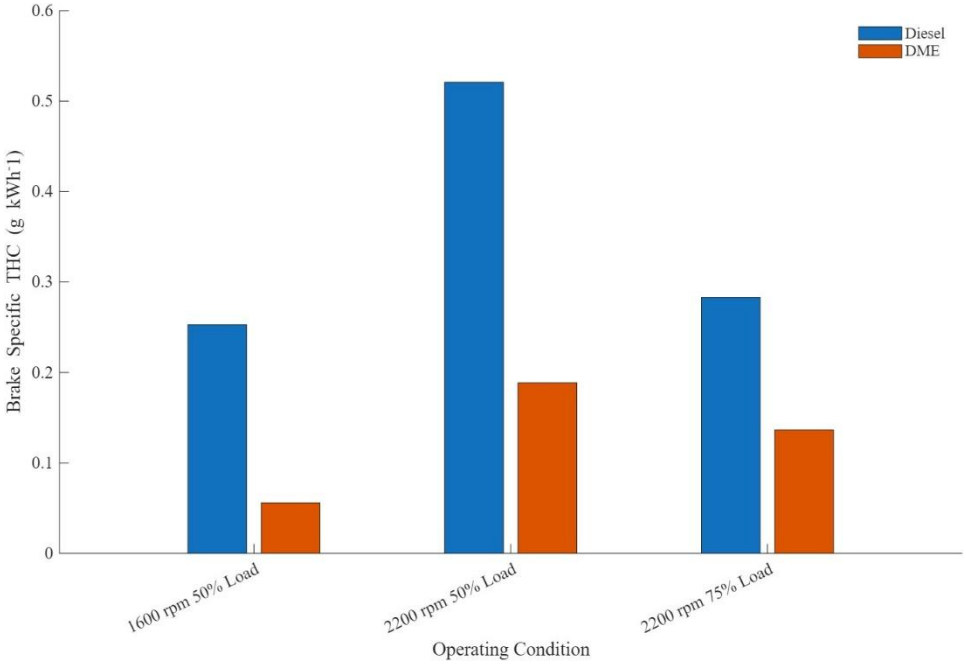


**Fig. 21.** Brake specific total unburned hydrocarbons emissions for diesel and DME

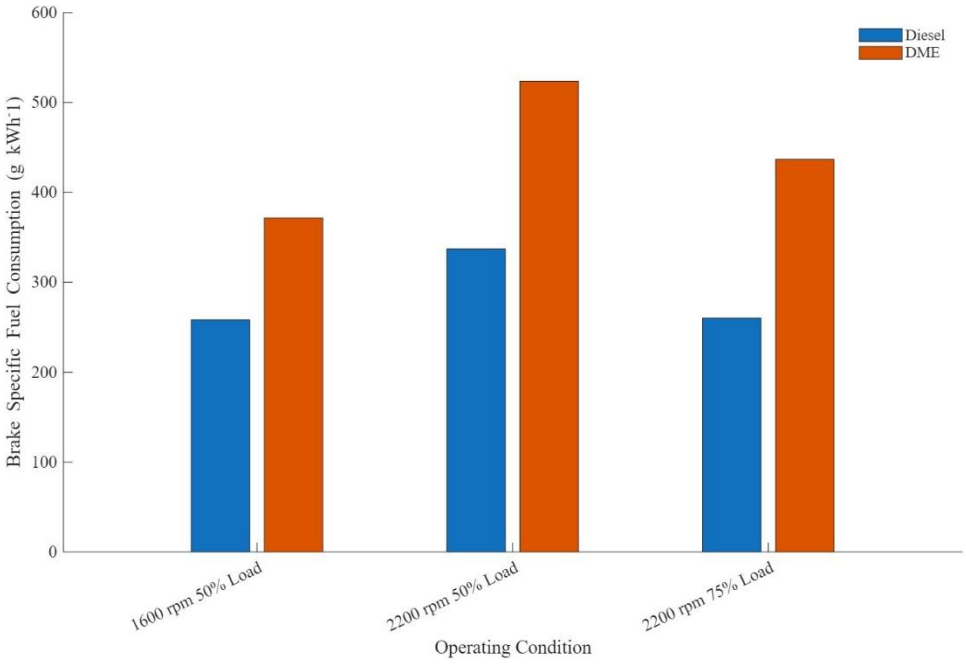


**Fig. 22.** Brake specific fuel consumption for diesel and DME

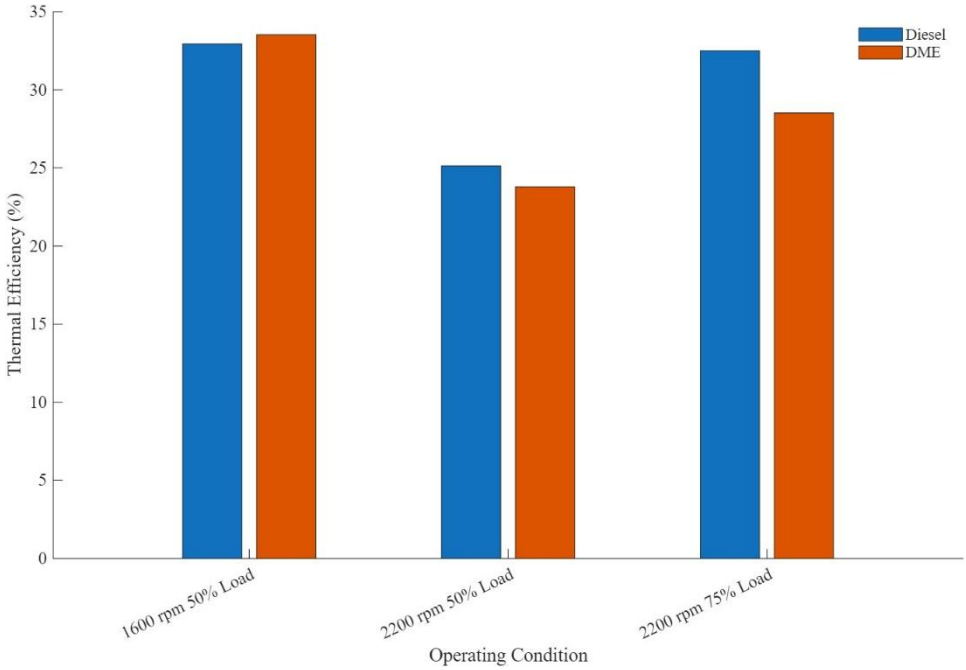


**Fig. 23.** Thermal Efficiency for diesel and DME

4.3 Baseline Diesel vs DME Discussion

The baseline comparison of diesel and DME under matched CA50, IMEP, and EGR illustrates clear distinctions in combustion phasing, heat release behavior, emissions formation,

and fuel consumption. By evaluating parameters such as SOI–CA5, CA10–90, peak AHRR, and peak pressure timing, the results of this study can be related to established diesel and DME combustion characteristics documented in the literature.

The SOI–CA5 results show that diesel consistently reaches 5% mass fraction burned sooner after SOI than DME. While DME is often noted for its short chemical ignition delay due to its high cetane number, several experimental studies have reported that pressure-based detection of ignition can appear later for DME in moderate load operation because its fast vaporization, high latent heat, and low early heat release intensity delay the onset of detectable HRR rise [3], [5], [50]. The longer SOI–CA5 values measured for DME in this work align with literature and the observations that the timing of measurable heat release does not necessarily reflect the chemical ignition delay for DME and can be influenced by the weaker initial HRR signal.

The CA10–90 results also show strong agreement with the literature. Across all baseline points, DME burns over a narrower crank angle interval, with 4–5 deg shorter CA10–90 values than diesel. This reduction closely matches the 10–15% shorter burn durations reported by Arcoumanis et al. 2008, Kim et al. 2007 and Stepanenko et al. 2019, who attribute this behavior to DME's rapid vaporization, enhanced premixing, and the absence of a diffusion-limited burn phase [3], [5], [50]. In contrast, diesel's longer CA10–90 duration observed here is consistent with the persistent mixing-controlled combustion described by Heywood 1988 [1].

The AHRR profiles further reinforce these distinctions. In this study, diesel consistently produces premixed heat release spikes that are approximately 50–75% larger than those of DME. This finding corresponds closely to diesel combustion theory, which attributes the magnitude of the premixed spike to the formation of partially vaporized, fuel-rich pockets that burn rapidly at

the onset of high temperature ignition [5], [50]. The results measured here therefore reflect mechanisms described in Heywood 1988 where even with a shorter SOI–CA5 interval, diesel accumulates a substantial amount of reactive mixture before the start of combustion, producing a sharp heat release spike once ignition begins [1]. DME, by contrast, exhibits the broad, single-stage AHRR, which several authors have linked to its complete vaporization, highly uniform mixing, and lack of diffusion burning zones [3], [50], [51].

Peak pressure phasing also aligns with previously observed DME trends. In the present work, DME exhibits earlier peak pressure timing at higher speed and load but slightly later phasing at 1600 rpm and 50% load. Similar behavior was noted by Kim et al. 2007 and Youn et al. 2022, who reported that DME's phasing shifts depend strongly on charge temperature and mixing intensity [5], [15]. At higher speeds, faster mixing and more complete vapor phase distribution can advance combustion phasing, while at lower speeds, weaker early heat release can delay peak pressure location.

The particulate matter behavior observed in this study is consistent with established trends for diesel and DME combustion. Diesel PM measured here increased with load but did not show a consistent dependence on engine speed. Although diesel OC/EC fractions were not measured directly, the diesel reference study by Windom et al. n.d. shows that nearly half of diesel PM mass at similar load and speed conditions consists of EC [49]. In contrast, DME PM increased with both load and speed in this study, but the absolute PM mass remained significantly lower than diesel across all baseline points. The OC/EC analysis performed on DME samples showed that more than 95% of particulate mass consisted of OC, with EC contributing less than 5% at every condition. This result is consistent with previous DME combustion studies. Kim et al. 2007 reported nearly soot free DME combustion due to rapid

vaporization and minimized fuel-rich regions, while Zhang et al. 2008 showed that DME PM levels are typically one to two orders of magnitude lower than diesel and the PM mainly consists of volatile organic material consistent with OC [5], [12].

The $NO_x$ trends observed in this study are consistent with previously reported DME behavior under comparable moderate EGR conditions. At the baseline EGR level of approximately 22–24%, DME produces roughly 10–35% lower Brake specific $NO_x$ than diesel. Similar reductions have been documented by Kim et al. 2007, who found that DME consistently yields lower $NO_x$ than diesel at EGR levels representative of typical diesel operation [5]. Studies by Arcoumanis et al. 2008 and Putrasari et al. 2021 report that DME's more homogeneous temperature field, lower peak temperatures, and reduced high temperature residence time contribute to $NO_x$ suppression even under modest dilution, whereas diesel continues to exhibit the characteristic $NO_x$–soot tradeoff at similar EGR levels [50], [51].

The CO and THC emissions measured in this study also follow known trends. DME produces significantly lower CO and THC than diesel across all baseline points. Prior DME studies consistently attribute this behavior to DME's inherent oxygen content and its ability to form spatially uniform equivalence ratios, which together enable more complete oxidation even under moderate dilution [3], [5], [51]. Diesel, in contrast, displays increasing CO and THC, which aligns with the incomplete oxidation and flame quenching described by Heywood 1988 [1].

Both fuels operated at comparable mixture strengths under all baseline conditions. At the matched operating points (1600 rpm 50% load, 2200 rpm 50% load, and 2200 rpm 75% load), diesel lambda values were 1.41, 1.37, and 1.47, while DME lambda values were 1.47, 1.48, and 1.49, respectively. Both fuels exhibited similar lambda values, indicating that global equivalence

ratio was effectively matched across operating points. Therefore, the lower $NO_x$ and PM observed for DME are attributed to the inherent chemical and physical properties of the fuel rather than to variations in global lambda.

The fuel consumption and thermal efficiency trends measured in this study are also in strong agreement with the broader body of DME research. Because DME's LHV is approximately two-thirds that of diesel on a mass basis, the higher Brake specific fuel consumption observed here is expected and reflects the differences in fuel energy density rather than differences in combustion completeness. Despite this higher BSFC, the thermal efficiency of DME remains comparable to that of diesel across all baseline points. This behavior mirrors the findings of Arcoumanis et al. 2008, who reported that engines operating on DME frequently achieve similar or slightly improved indicated and brake thermal efficiencies, even while consuming a greater mass of fuel [50]. Similar trends were observed by Putrasari et al. 2021 and Kim et al. 2007, who attributed DME's efficiency to faster heat release rates, earlier combustion phasing, and reduced spatial and temporal temperature gradients, all of which contribute to lower heat transfer losses relative to diesel [5], [51]. Youn et al. 2022 likewise demonstrated that DME maintains strong thermal efficiency across a wide operating range, despite requiring higher mass flow to achieve matched load [15]. The alignment between these published results and those observed show that DME's higher BSFC does not carry an efficiency penalty and is primarily a reflection of fuel chemistry rather than a limitation of combustion performance.

Table 6 summarizes the measurement uncertainty for the key operating and emissions parameters used in testing. The table is based on a repeated test point at 1600 rpm, 50% load and 22% EGR that was performed at the beginning of each test day. For each parameter, the variation was evaluated and the uncertainty is reported as one sigma expressed as a percentage of the mean

value. This focuses on repeatability from day to day for the complete experimental system rather than on the variability within a single run.

The table shows that the engine operating conditions were very well controlled. Engine speed had the lowest uncertainty at ±0.25%, indicating that the dynamometer and control system held the target speed accurately. Intake and exhaust pressures and IMEP remained within roughly ±1% and ±3% respectively. CA50 uncertainty was ±1.97%, which is acceptable for combustion phasing measurements [1]. EGR rate uncertainty was ±3.85%, which reflects the sensitivity of the dilution level to small changes in pressure and flow but still indicates good control of the target operating condition. Brake thermal efficiency also showed a low uncertainty of ±1.04%, which shows that the overall energy balance of the engine and dynamometer system was stable from day to day.

The emissions measurements exhibit larger percentage uncertainties, which is expected when working with low engine out emissions [52], [53]. BSNOx uncertainty was ±8.93% and BSPM was ±6.03%. The largest uncertainties occurred for BSCO and BSTHC at ±15.29% and ±22.44% respectively. These higher values arise because the absolute concentrations of CO and THC for DME are very small, so even modest analyzer drift or noise appears as a large percentage difference.

Taken together, the baseline combustion, emissions, and fuel consumption results are in agreement with DME combustion literature. Differences between diesel and DME in SOI–CA5 timing, combustion duration, peak AHRR, and PM composition match the mechanisms attributed in previous studies to fuel vaporization, mixture stratification, chemical kinetics, and the suppression of diffusion burning. The emissions and efficiency results further shows that DME can achieve low $NO_x$ and PM compared to diesel without penalties in CO or THC as comparable

operating points. The uncertainty analysis in Table 6 strengthens this conclusion by demonstrating that key operating and performance parameters were well controlled and repeatable across days, with low one-sigma uncertainties for engine speed, pressures, IMEP, CA50, EGR, and brake thermal efficiency. Although the emissions measurements exhibited higher relative uncertainties, this behavior is expected at very low engine out emission levels and does not affect differences observed between fuels. The alignment between the present experimental data and prior DME research reinforces the validity of the baseline comparisons used as the foundation for the combustion parameter sweeps presented in Chapter 5, and the measured uncertainties further support the reliability of these conclusions.

Table 6 Repeatability-Based One-Sigma Uncertainties for Engine Operating and Emissions Parameters

| Parameter | Units | Uncertainty (%) |
|---|---|---|
| Engine Speed | rpm | ±0.25 |
| Intake Pressure | bar (a) | ±1.17 |
| Intake Temperature | C° | ±6.58 |
| Exhaust Pressure | bar (a) | ±1.03 |
| EGR Rate | % | ±3.85 |
| IMEP | bar | ±2.99 |
| CA50 | deg ATDC | ±1.97 |
| Thermal Efficiency | % | ±1.04 |
| BSCO | g $kWh^{-1}$ | ±15.29 |
| BSTHC | g $kWh^{-1}$ | ±22.44 |
| $BSNO_x$ | g $kWh^{-1}$ | ±8.93 |
| BSPM | g $kWh^{-1}$ | ±6.03 |

# CHAPTER 5: IMACT OF INJECTIONG TIMING AND EGR RATE ON DME PERFORMANCE

The baseline comparison demonstrated that DME can operate at combustion phasing and thermal efficiency comparable to diesel, with reduced PM and $NO_x$ emissions. Building on these results, a series of operating parameter sweeps were performed to evaluate how DME responds to injection timing and EGR dilution, $NO_x$ tradeoff plots (e.g. CO vs $NO_x$) are used as a means for performance evaluation. The purpose of this chapter is to characterize the sensitivity of DME combustion to these parameters and identify operating zones that achieve minimum emissions while maintaining acceptable fuel consumption.

## 5.1 Injection Timing Sweep

An injection timing sweep was conducted at 1600 rpm 50% load to determine the combustion phasing sensitivity of DME relative to $BSNO_x$ and BSFC. IMEP and EGR rate were fixed for the sweep. The results are shown in Figure 24 and Figure 25, where in-cylinder pressure traces and AHRRs are shown and injection timing is expressed in terms of CA50 to unify the comparison across firing conditions.

Figure 24 presents the averaged in-cylinder pressure traces for the DME injection timing sweep conducted at 1600 rpm and 50% load. The figure shows the pressure evolution for injection timings ranging from 13 deg BTDC to 1 deg ATDC. All conditions follow a similar compression trajectory prior to ignition, after which the traces diverge according to the injection timing. Earlier injections produce higher peak pressures and an earlier rise in pressure relative to TDC, while later injections delay the start of combustion and lower the pressure rise rate.

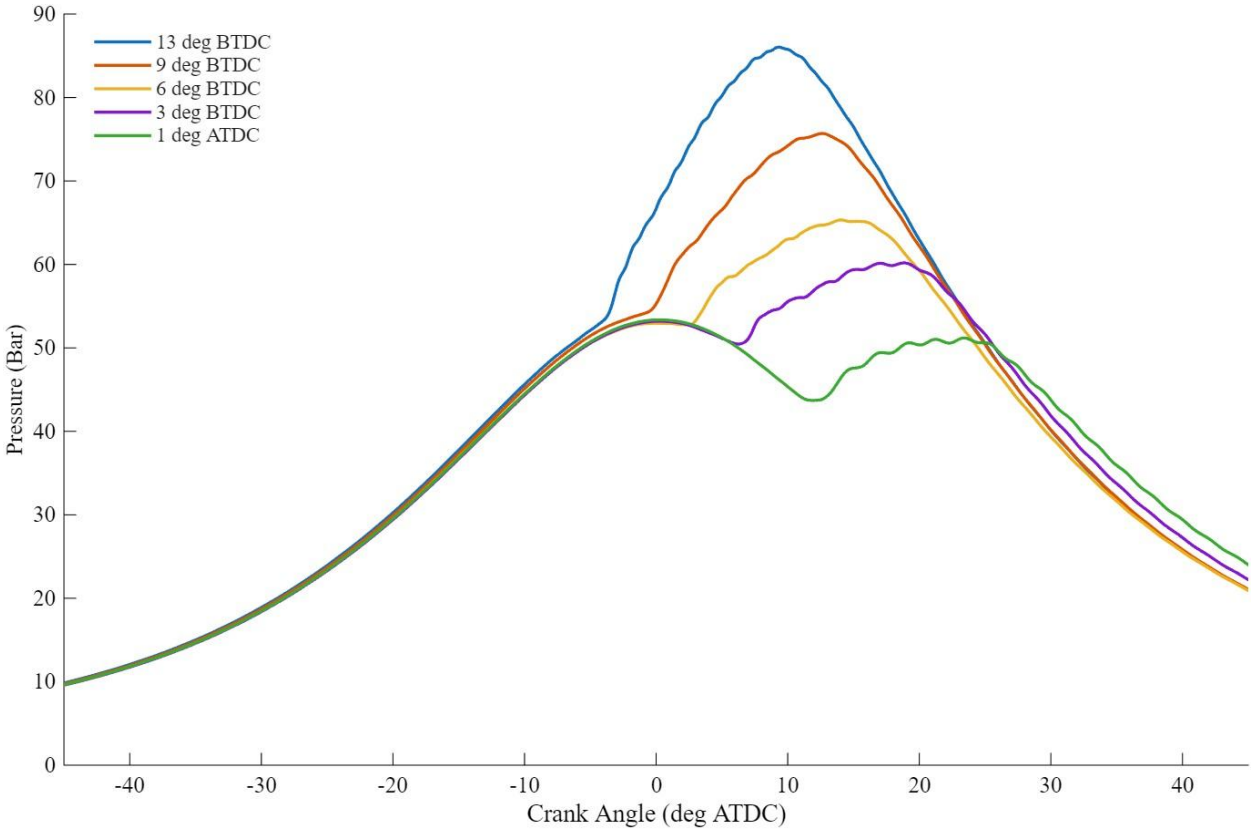


**Fig. 24.** Average pressure traces for injection timing sweep at 1600 rpm 50% load

Figure 25 presents the AHRR for DME at 1600 rpm and 50% load across an injection timing sweep, showing how combustion phasing shifts as SOI is advanced or retarded. The most advanced case (13 deg BTDC) exhibits the earliest rise in heat release and an early, narrow main heat release peak. As injection timing is progressively retarded, the start of combustion moves later in the cycle, and the main heat release peak shifts accordingly toward more positive crank angles, with the curves becoming slightly broader and less sharply peaked. The most retarded case (1 deg ATDC) shows the latest onset of combustion and the most delayed peak heat release location, accompanied by a wider main combustion region.

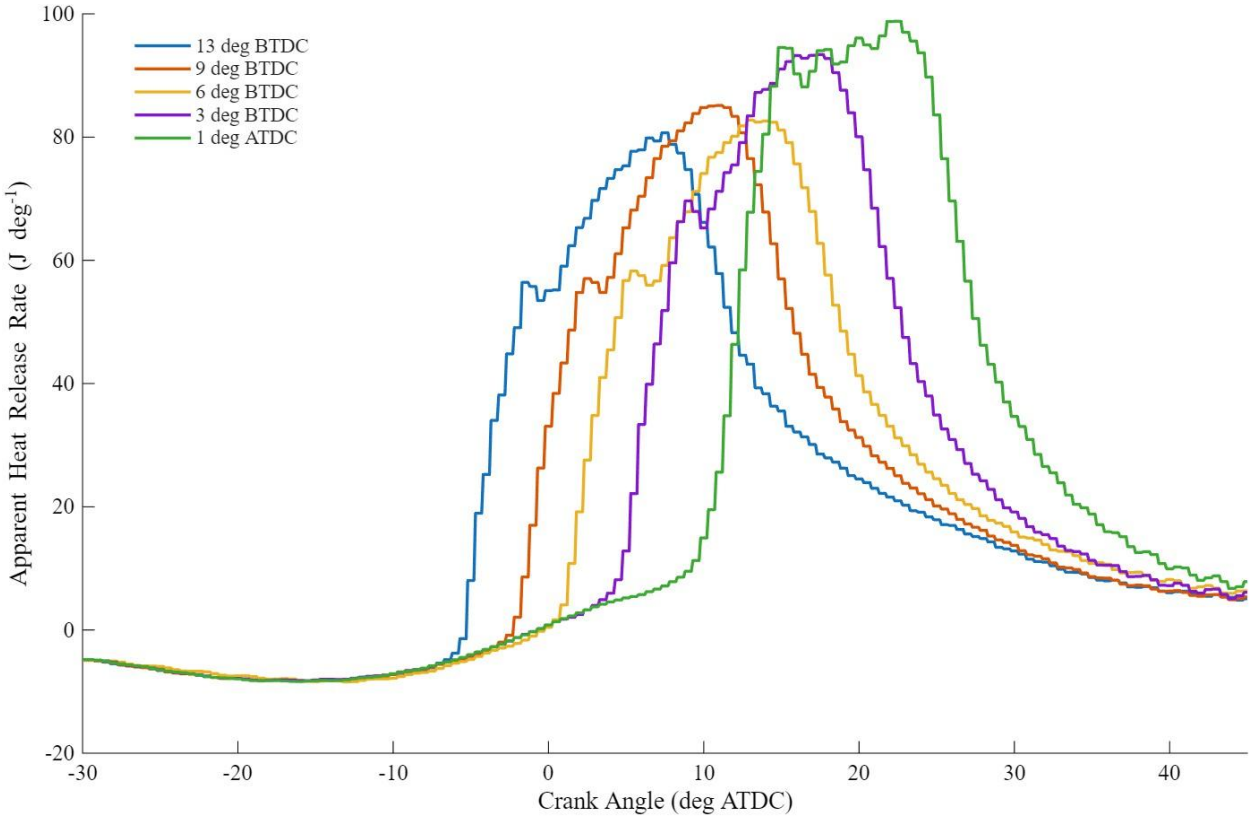


**Fig. 25.** Apparent heat release rates for injection timing sweep at 1600 rpm 50% load

Figure 26 presents the injection timing sweep for DME at 1600 rpm and 50% load by plotting CA50 against SOI–CA5, often referred to as ignition delay. As CA50 moves later in the cycle, corresponding to progressively retarded injection timing, the SOI–CA5 duration generally becomes shorter, indicating a reduced delay between injection and the onset of combustion. This trend continues until CA50 approaches about 23 deg ATDC, which corresponds to the most retarded injection timing case (1 deg ATDC). At this point the SOI–CA5 value levels off relative to earlier points.

Figure 27 presents CA10–90, which can be considered the combustion duration, plotted against CA50 for the DME injection timing sweep at 1600 rpm and 50% load, showing how the main combustion duration changes as injection timing is retarded. As CA50 moves later in the

cycle with progressively retarded injection timing, CA10–90 consistently decreases, indicating that the main combustion duration becomes shorter as timing is delayed. This trend persists across the full range of phasing, with the shortest durations occurring at the most retarded conditions.

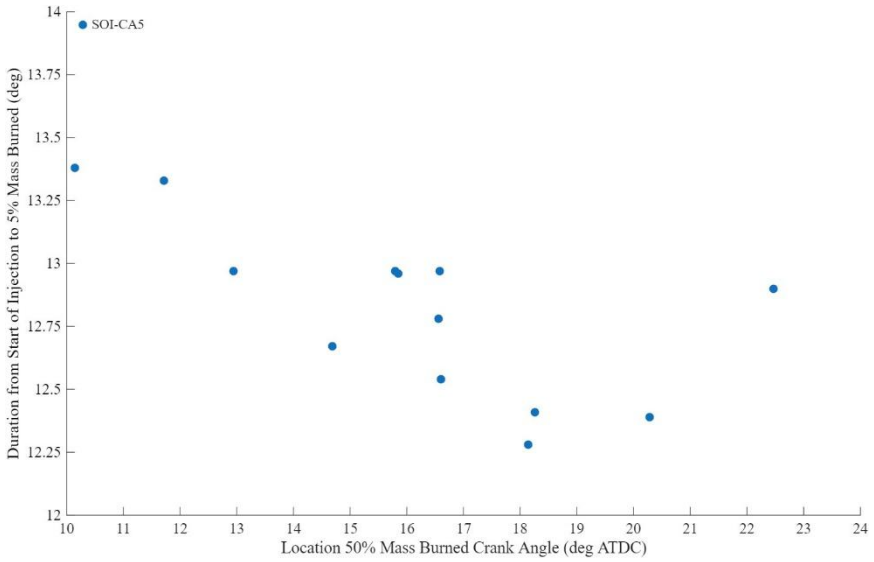


**Fig. 26.** Location 50% mass burned vs start of injection to 5% mass fraction burned duration

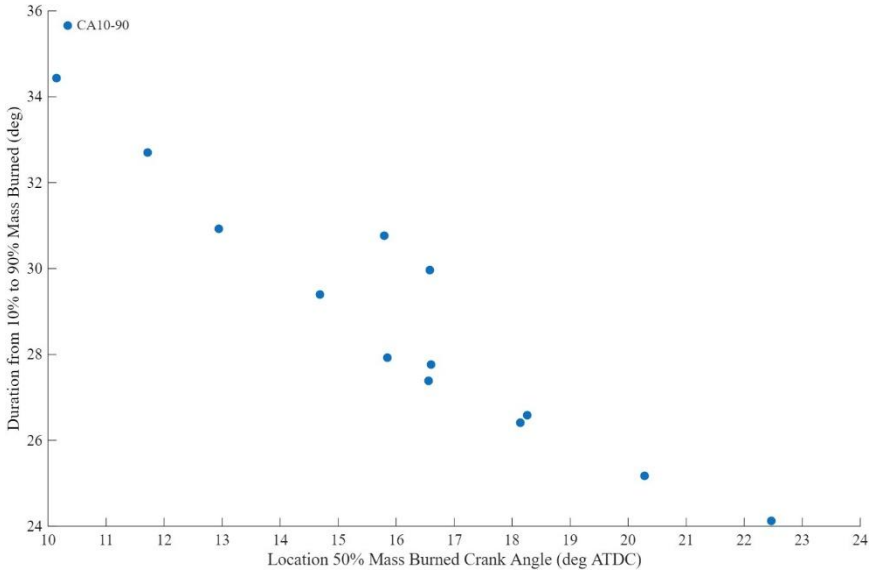


**Fig. 27.** Location 50% mass burned vs 10% mass burned to 90% mass burned duration

Figure 28 presents the COV for IMEP and CA50 across the DME injection timing sweep at 1600 rpm and 50% load, plotted against CA50 to represent combustion phasing. These COV parameters are generally indicative of combustion stability. As CA50 shifts later with progressively retarded injection timing, the COV of CA50 steadily decreases, indicating improved cycle to cycle phasing consistency at more retarded timings. In contrast, the COV of IMEP remains generally uniform across the sweep, showing only modest variation with timing. A single outlier appears near CA50 of about 13 deg ATDC, where IMEP COV increases noticeably relative to the surrounding points.

Figure 29 shows the relationship between combustion phasing, $NO_x$ emissions, and BSFC. As CA50 shifts earlier in the cycle, Brake specific $NO_x$ increases and as CA50 is retarded, $NO_x$ decreases steadily, and all data points with CA50 greater than approximately 15 deg ATDC fall below the diesel baseline $NO_x$ level indicated by the dashed red line. BSFC displays an opposite trend where earlier CA50 points show lower BSFC values, while BSFC increases gradually as CA50 is retarded.

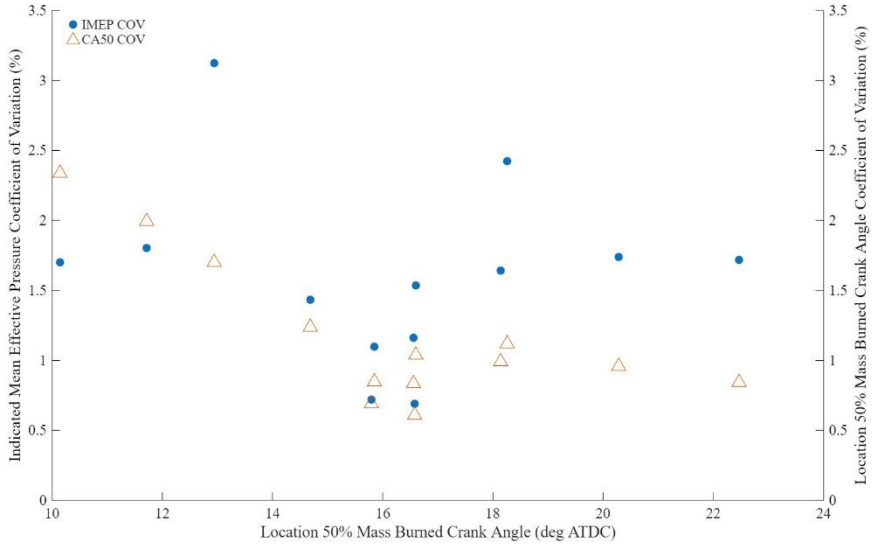


**Fig. 28.** Location of 50% mass burned vs coefficient of variation for indicated mean effective pressure and location of 50% mass burned

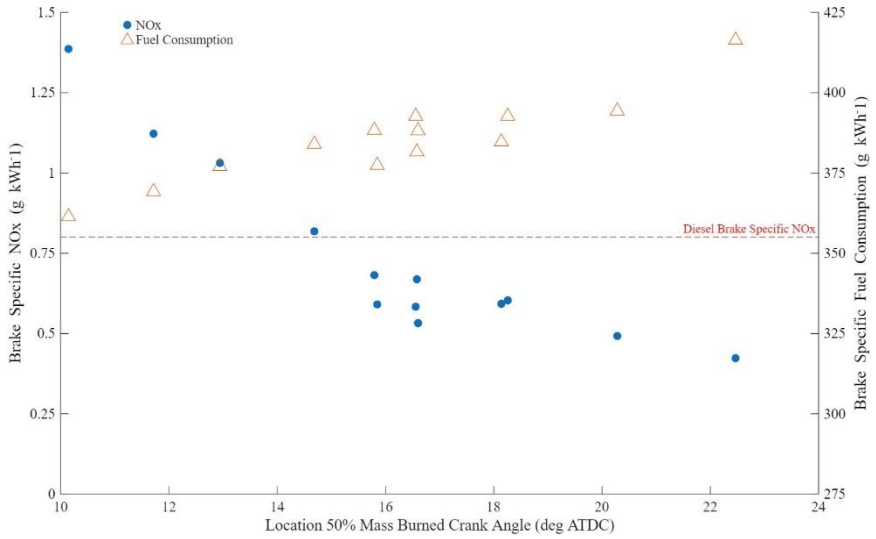


**Fig. 29.** Location 50% mass burned crank angle vs brake specific nitrogen oxides and brake specific fuel consumption

5.2 EGR Sweeps

An EGR sweep was performed at 1600 rpm and 50 % load to evaluate the effect of increasing dilution on $NO_x$ reduction, the associated tradeoffs with other emissions, and the limits of combustion stability. For this sweep, IMEP and CA50 were held constant while EGR rate was varied. The resulting combustion and emissions behavior is presented in Figures 30–36, including in-cylinder pressure traces, AHRR, relationships between EGR rate and SOI–CA5 and CA10–90, COV for IMEP and CA50, and the corresponding emissions trends.

Figure 30 presents the averaged in-cylinder pressure traces for the DME EGR sweep conducted at 1600 rpm and 50% load. The figure includes EGR rates ranging from 22% to 55%. All conditions follow a similar compression trajectory prior to combustion, with the traces beginning to diverge as combustion initiates and proceeds through the expansion stroke. The 55% EGR case exhibits a higher-pressure curve throughout compression and early combustion because additional boost pressure was required to maintain the target operating.

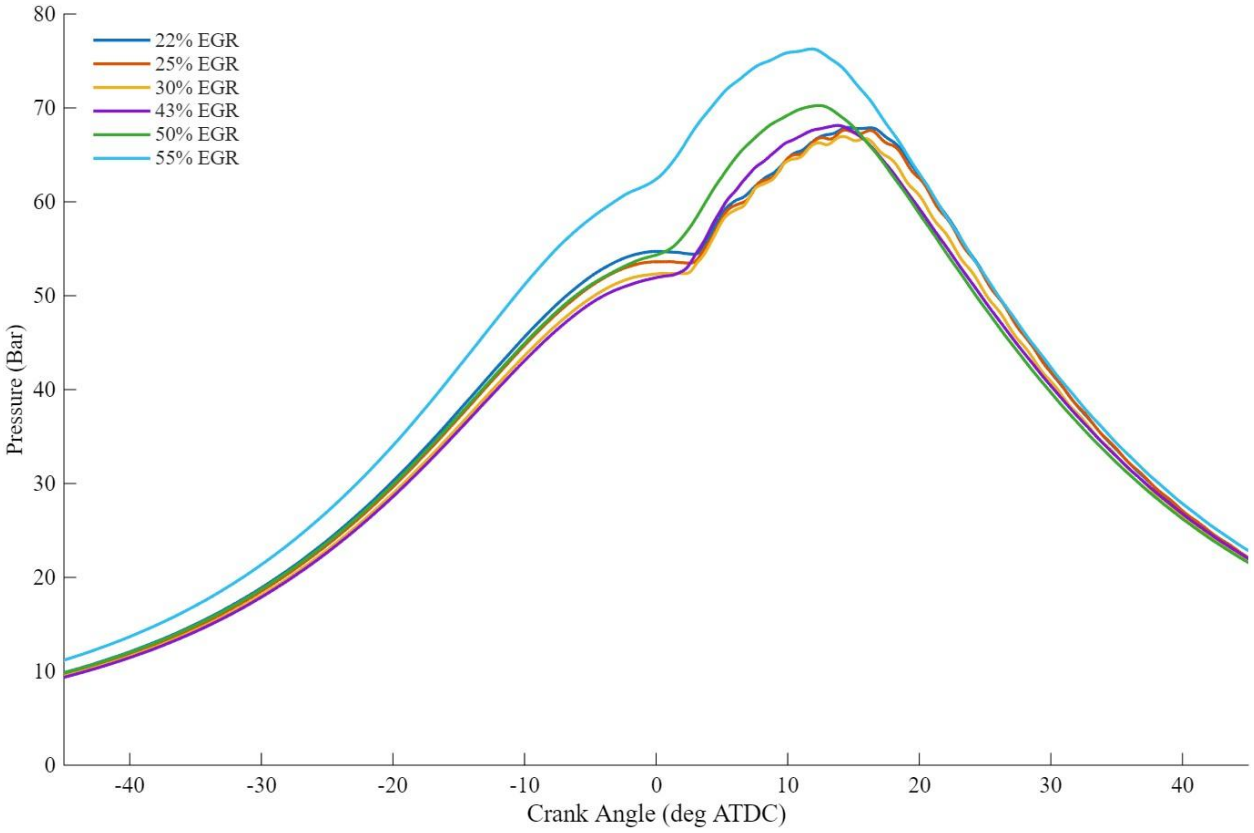


**Fig. 30.** Average pressure traces for exhaust gas recirculation sweep at 1600 rpm 50% load

Figure 31 shows the AHRR traces for the DME EGR sweep at 1600 rpm and 50% load, with EGR rates ranging from 22% to 55%. As EGR increases, the onset of heat release remains similar, but the shape and magnitude of the main heat release event shift. Lower EGR cases (22%–30%) exhibit higher peak AHRR and a sharper rise in heat release, while higher EGR levels (40%–55%) show reduced peak magnitudes and broader main combustion profiles.

Figure 32 shows the duration for SOI–CA5 across the DME EGR sweep at 1600 rpm and 50% load. The figure shows an increase in SOI–CA5 duration as EGR rate rises from 22% to 55%, with higher EGR rates corresponding to longer intervals between injection and the onset of combustion.

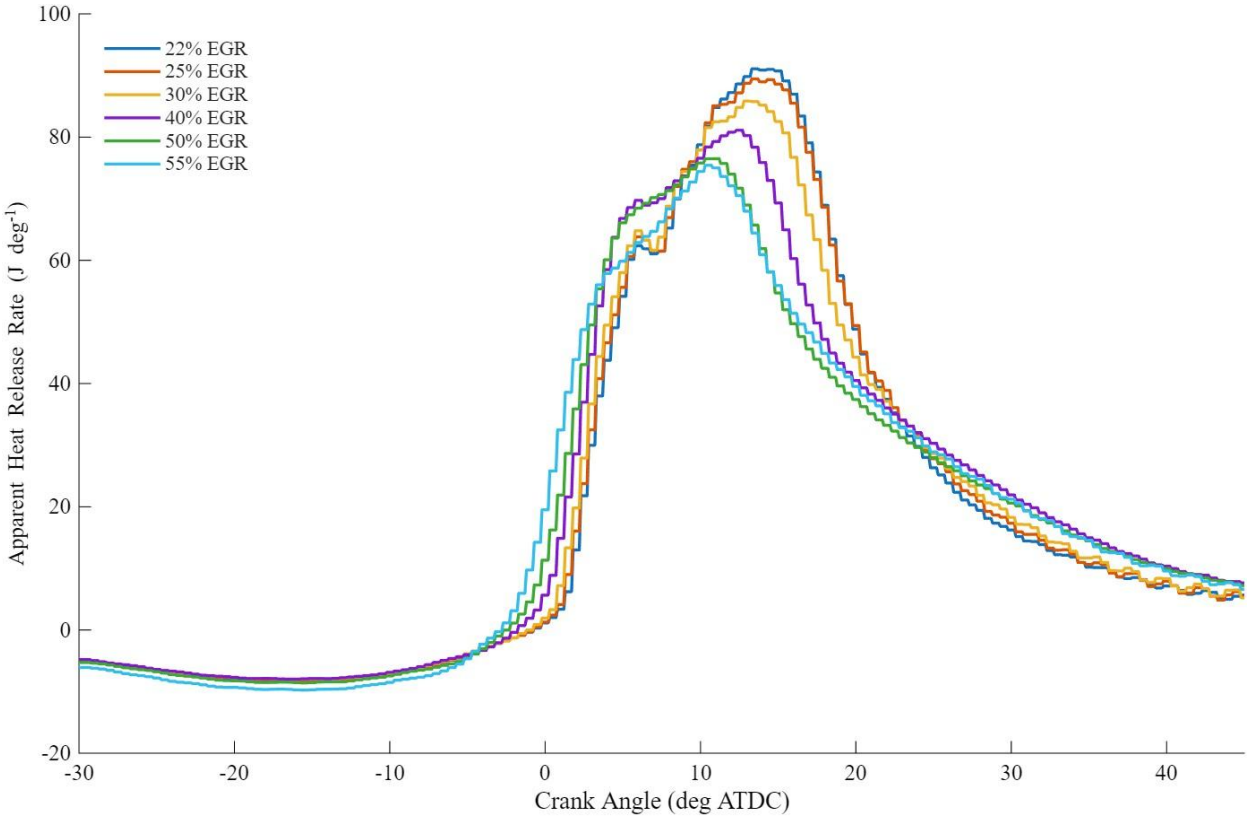


**Fig. 31.** Apparent heat release rates for exhaust gas recirculation sweep at 1600 rpm 50% load

Figure 33 presents the CA10–90 across the DME EGR sweep at 1600 rpm and 50% load. The figure shows that CA10–90 increases as EGR rate rises from 22% to 55%, with higher EGR rates producing progressively longer burn durations across the sweep.

Figure 34 presents the COV for IMEP and CA50 across the DME EGR sweep at 1600 rpm and 50% load. COV of IMEP and COV of CA50 are shown for EGR rates ranging from 22% to 55%. The figure shows that both COV of IMEP and COV of CA50 vary across the sweep, with less variation at the moderate EGR points and greater variation at higher EGR rates. IMEP COV exhibits the largest range of variation, while CA50 COV remains relatively low at the lower EGR rates and increases at the upper end of the sweep.

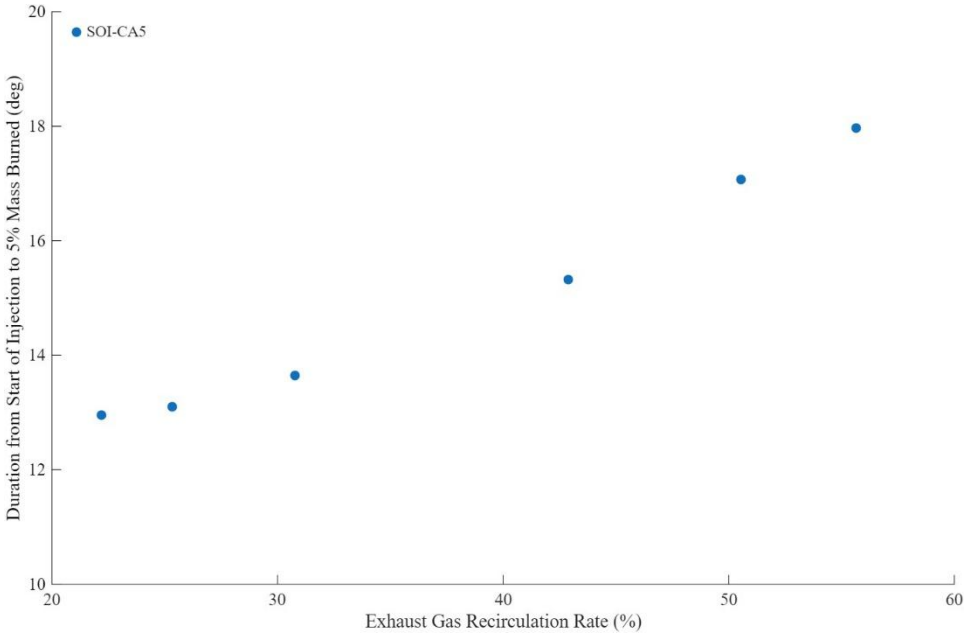


**Fig. 32.** Exhaust gas recirculation rate vs start of injection to 5% mass fraction burned duration

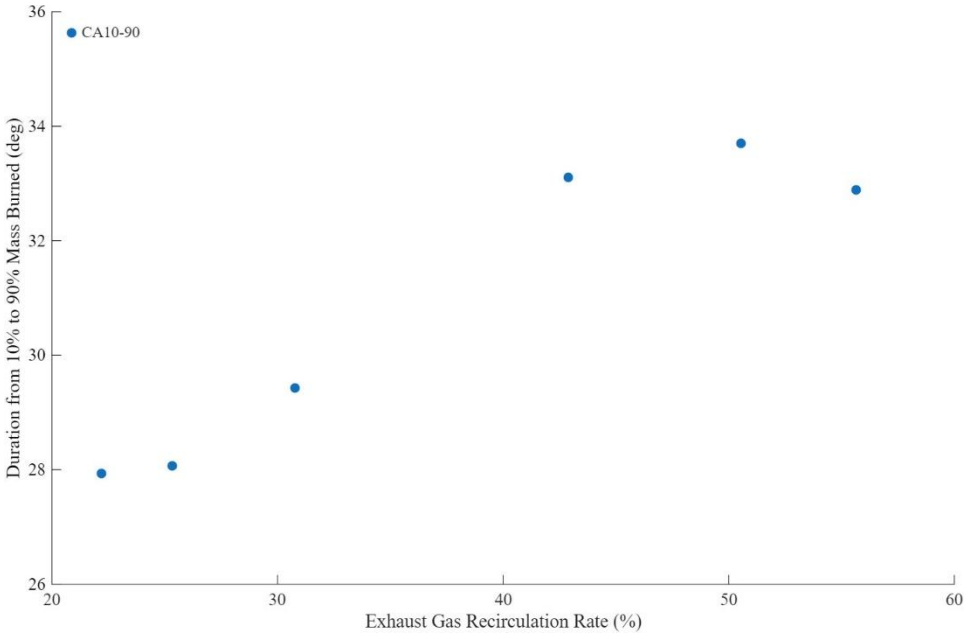


**Fig. 33.** Exhaust gas recirculation rate vs 10% mass burned to 90% mass burned duration

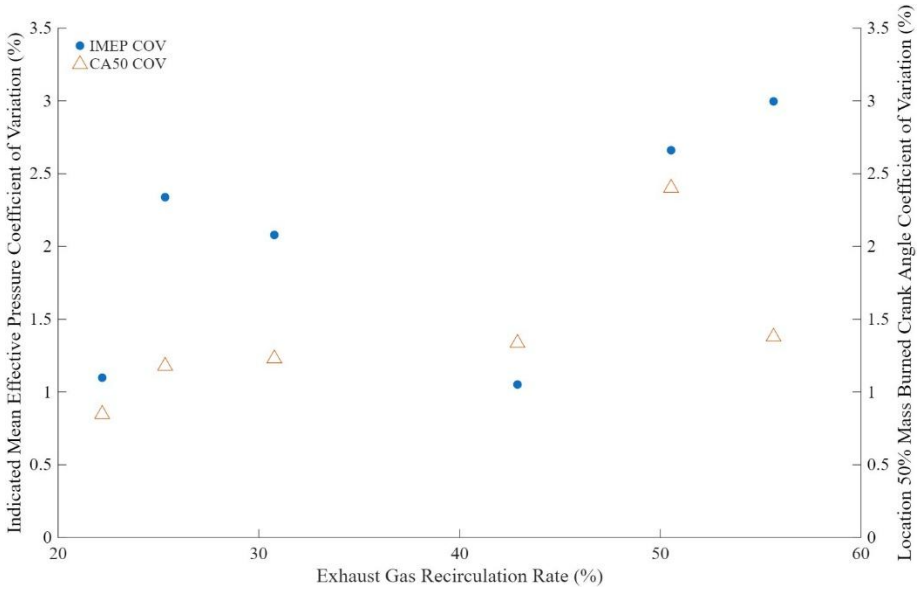


**Fig. 34.** Exhaust gas recirculation rate vs coefficient of variation for indicated mean effective pressure and location of 50% mass burned

The effect of EGR dilution on DME combustion is shown in Figure 35, comparing $BSNO_x$ and BSCO as a function of EGR rate. $NO_x$ decreases with increasing EGR. However, elevated EGR introduces incomplete oxidation behavior, visible in the rise of CO emissions at high EGR rates. This $NO_x$-CO tradeoff occurs around 40% EGR where the levels of CO emissions are significantly higher than the baseline value for diesel.

BSPM remained consistently low throughout the sweep, staying below the diesel baseline value of 0.50 g $kWh^{-1}$ and exhibiting only modest variation despite substantial changes in EGR rate as shown in Figure 36. This stability in PM is notable, as increased EGR typically suppresses $NO_x$ formation at the expense of soot production. However, PM did not increase as $NO_x$ was reduced. Concurrently, $NO_x$ decreased sharply with increasing EGR, falling from approximately 0.58 g $kWh^{-1}$ at low EGR to near zero levels beyond 50% EGR.

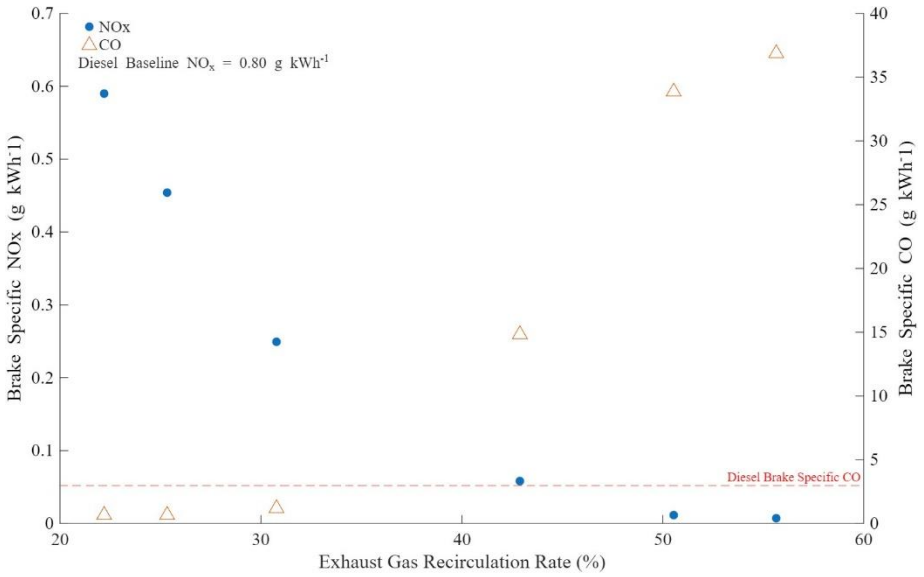


**Fig. 35.** EGR rate vs brake specific nitrogen oxides and brake specific carbon monoxide

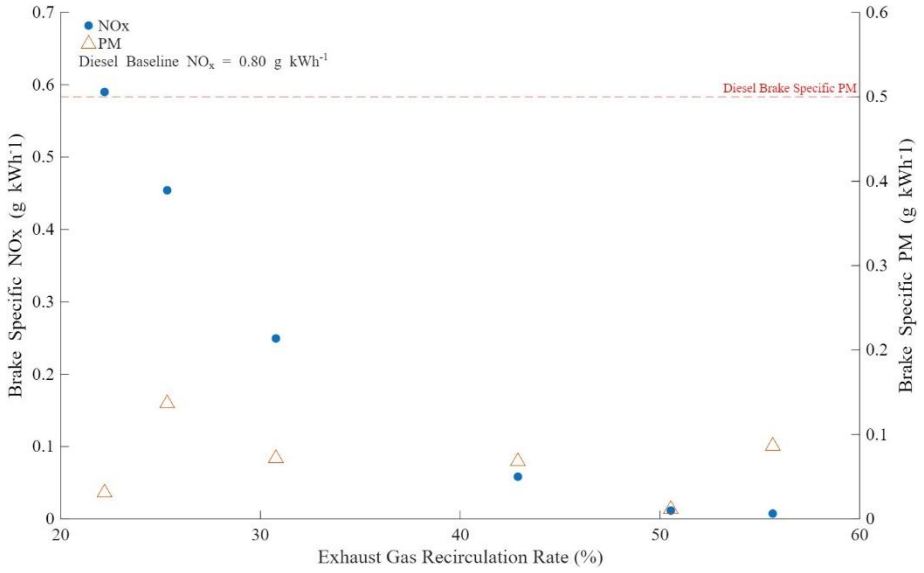


**Fig. 36.** EGR rate vs brake specific nitrogen oxides and brake specific particulate matter

## 5.3 $NO_x$ Tradeoffs

To evaluate how emissions interact across varying operating conditions, $NO_x$ was plotted against CO, PM, THC, and fuel consumption. The data points plotted consist of all the operating points and fuels from this study and are represented in Figures 37–40.

In Figure 37, a clear $NO_x$–CO tradeoff is observed. CO remains relatively constant as $NO_x$ decreases, with no notable rise in CO until $NO_x$ levels drop below approximately 0.1 g $kWh^{-1}$. Above this threshold, CO emissions for DME remain lower than diesel at similar $NO_x$ levels.

Figure 38 shows a favorable PM–$NO_x$ tradeoff. PM emissions remain low across the full $NO_x$ range, suggesting that soot formation is largely independent of $NO_x$ reduction strategies when using DME. In contrast, diesel produces higher PM at comparable $NO_x$ values. One DME outlier exists, where PM rises to 0.47 g $kWh^{-1}$ at a $NO_x$ level of 0.58 g $kWh^{-1}$.

Figure 39 shows that THC increases as $NO_x$ decreases, following a trend similar to CO. THC remains near zero and below diesel across most of the $NO_x$ range, and only begins to rise once $NO_x$ drops below the same approximately 0.1 g $kWh^{-1}$ threshold identified in the CO results.

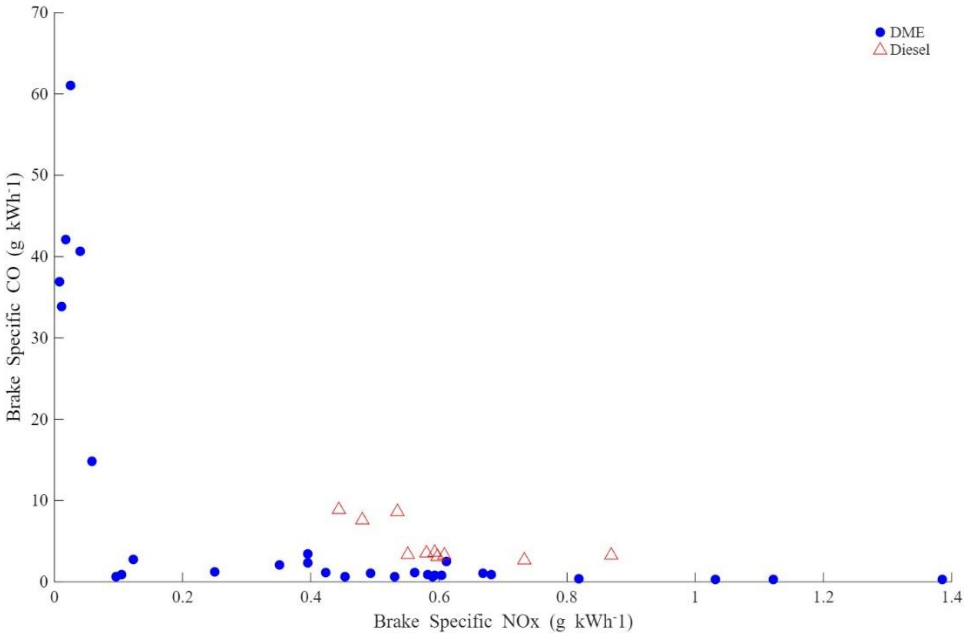


**Fig. 37.** Brake specific nitrogen oxides vs brake specific carbon monoxide

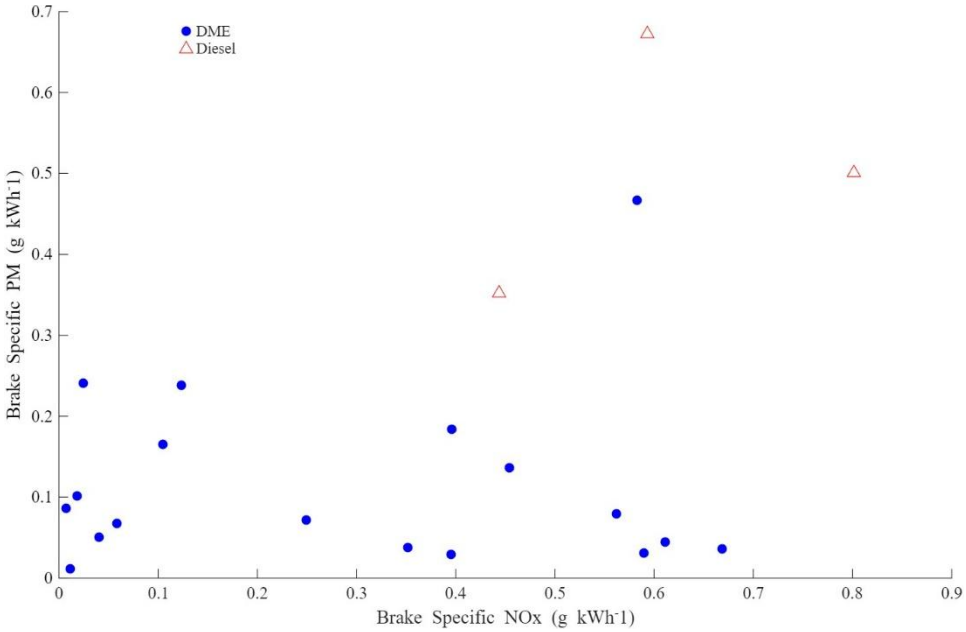


**Fig. 38.** Brake specific nitrogen oxides vs brake specific particulate matter

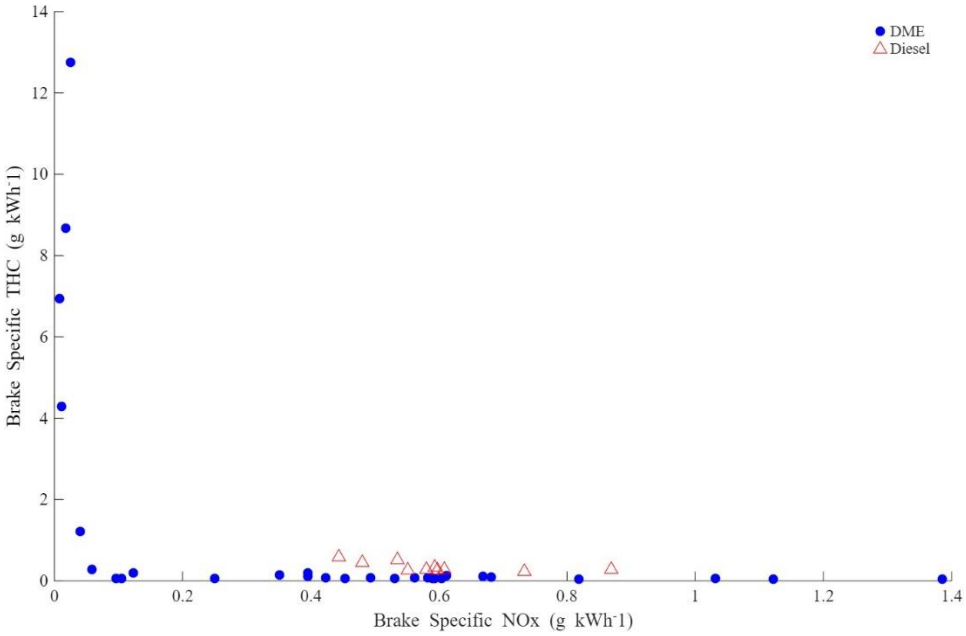


**Fig. 39.** Brake specific nitrogen oxides vs brake specific total unburned hydrocarbons

Fuel consumption trends are shown in Figure 40. Energy based BSFC increases as brake specific $NO_x$ decreases. A noticeable rise in energy based BSFC occurs near the same 0.1 g $kWh^{-1}$ $NO_x$ threshold where THC and CO also increase. However, above this threshold energy

based BSFC remains constant, with the exception of several points near 15 kJ $kWh^{-1}$. These elevated values correspond to the higher speed and load conditions at 2200 rpm and 50% and 75% load.

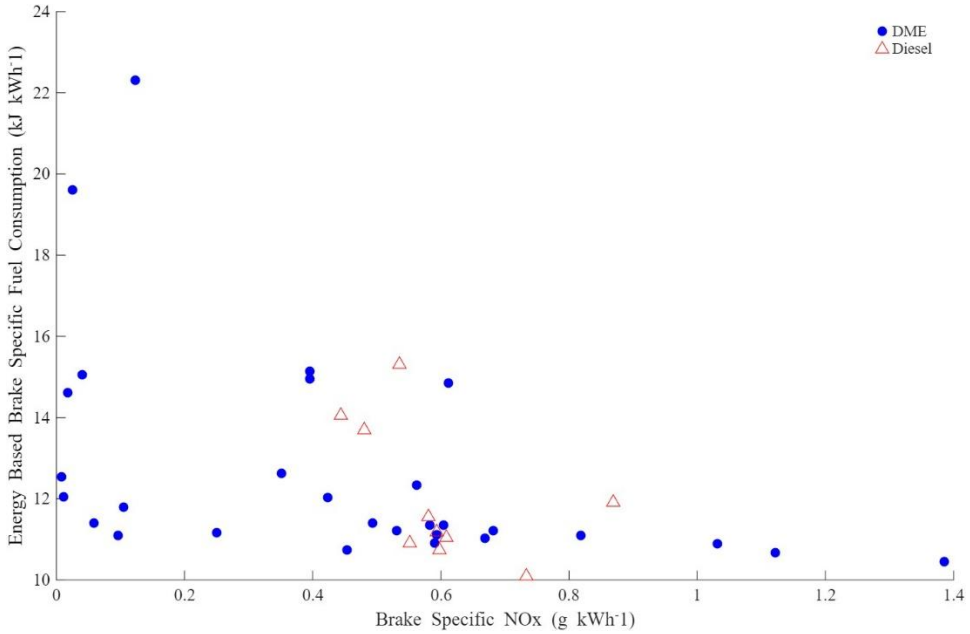


**Fig. 40.** Brake specific nitrogen oxides vs energy based brake specific fuel consumption

5.4 DME Combustion Discussion

The injection timing and EGR sweeps conducted in this chapter show how DME responds to changes in combustion phasing and dilution. By analyzing in-cylinder pressure traces, AHRR, SOI–CA5, CA10–90, and combustion stability through COV of IMEP and CA50, a range of operating conditions that produce low $NO_x$, low PM, stable combustion, and competitive fuel consumption can be found.

As injection timing is retarded across the sweep, the main combustion event shifts later into the expansion stroke, lowering peak temperature and residence time, which in turn suppresses $NO_x$ formation and reduces overall heat release magnitude, although at the expense of fuel consumption. Earlier combustion phasing produces higher peak pressures and sharper heat

release peaks due to elevated temperatures near TDC. $NO_x$ levels do not fall below the diesel baseline until combustion is shifted to a CA50 of roughly 15 deg ATDC or later. These conditions increase thermal $NO_x$ formation through the extended Zeldovich mechanism, which dominates $NO_x$ production in conventional and moderately premixed CI operation[1], [20].

The pressure and AHRR traces in this study show a single premixed-type profile heat release across all injection timings, consistent with the behavior reported by Kim et al. 2007 and Arcoumanis et al. 2008, who observed that DME in CI engines tends to burn in a broad, single-stage premixed fashion due to its high cetane number, high volatility, and lack of soot forming C–C bonds[50], [54]. Similar single-stage premixed heat release structures with reduced diffusion burning and reduced smoke have been observed for DME by Song et al. 2004 and Huang et al. 1999, who showed that homogeneous premixed combustion dominates and suppresses late diffusion flames [55], [56]. Roh et al. 2018 and Park et al. 2012 further showed that DME in a common rail CI engine exhibits relatively smooth, premixed-dominated AHRR profiles over a wide range of injection strategies, supporting the trends observed here[57], [58]. Together, these studies reinforce that the single-stage premixed heat release patterns observed across the injection timing sweep are characteristic of DME combustion.

The ignition timing related metrics further clarify this behavior. The SOI–CA5 interval shortens as injection timing is retarded because the charge temperature is higher near TDC and DME's ignition delay becomes very short under these warm conditions. Youn et al. 2022 reported that, in a DME fueled CI engine, ignition delay is governed strongly by in-cylinder temperature and early reaction rates, rather than by the crank angle separation between injection and ignition[15]. Teng et al. 2003 also showed that DME's physical and chemical delays collapse rapidly once local gas temperature exceeds a critical level, making ignition timing highly

sensitive to temperature and less dependent on injection timing in warmed conditions[59]. Spray ignition experiments by Cung et al. 2021 similarly demonstrated that DME autoignition occurs quickly once the vaporizing jet encounters sufficiently hot ambient gas, with shorter ignition delay and lower lift-off length than diesel under the same conditions[60]. This supports the observed SOI–CA5 trend, which decreases as in-cylinder temperatures rise due to the proximity to TDC.

CA10-90 follows the same trend as timing is retarded, the CA10–90 burn duration decreases, reflecting a more compact and rapid release of heat within a narrower crank angle window. This observation aligns with studies on DME CI combustion by Huang et al. 1999, who reported that DME exhibits shorter combustion duration and more compact heat release when mixture preparation is favorable and in-cylinder temperatures are high, even when the peak heat release magnitude is reduced [56].

Combustion stability metrics reveal additional insights. Across the timing sweep, COV of IMEP remained below accepted stability limits for CI engines, which generally define stable operation as COV of IMEP less than about 5% [1]. In this sweep, COV of IMEP stayed under 3.2%, indicating consistently stable combustion. The COV of CA50 decreases steadily as combustion is retarded, demonstrating that more consistent combustion phasing occurs when ignition takes place closer to the higher and more uniform cylinder temperatures near TDC. COV of CA50 values below 2–3% indicated stable phasing, and in this sweep all conditions remained under about 2.5% COV of CA50 [1], [61]. A DME cyclic variation study by Sezer 2025 showed that COV of CA50 and IMEP remain very low until combustion phasing is pushed to the edge of stable operation, at which point both metrics rise sharply as partial burn and misfire cycles

appear[35]. This behavior is consistent with the trends observed in the present study, where COV values remain low throughout the timing sweep.

When the combustion behavior is compared with emissions and fuel consumption trends, an optimal phasing becomes clear. Earlier phasing increases $NO_x$ sharply, whereas late phasing degrades efficiency as combustion moves further into expansion. The point where $NO_x$ is reduced without incurring a significant BSFC penalty corresponds to a CA50 of approximately 16 deg ATDC. This phasing is consistent with other DME CI studies that identified moderately retarded combustion phasing as the region that minimizes $NO_x$ while preserving efficiency, particularly when combined with suitable EGR levels[15], [50], [62]. Zhang et al. 2009 reported that moving CA50 moderately into the expansion stroke reduces $NO_x$ without a large efficiency penalty, while further retardation produces rising BSFC and incomplete combustion[63]. The injection timing sweep in this chapter therefore establishes an optimal CA50 at 16 deg ATDC for low $NO_x$ and low PM DME operation.

The EGR sweep expands the analysis by isolating the effects of dilution on combustion and emissions at the optimal CA50 found previously. Increasing EGR from 22% to 55% extends SOI–CA5 and CA10–90 due to reduced oxygen concentration, increased specific heat of the cylinder charge, and lower in-cylinder temperature[1], [20]. However, combustion remains stable throughout the full EGR sweep, with both COV of IMEP and COV of CA50 staying within accepted stability limits. Although both metrics increase with higher dilution, the EGR sweep remained within these thresholds, with COV of IMEP staying under 3% and COV of CA50 remaining below 2.5%. Only the highest EGR points display rising variability, suggesting that misfire proximity is reached beyond 50% EGR. This trend is consistent with findings by Roh et al. 2018 who showed that DME maintains relatively stable combustion over a wide EGR range,

with instability emerging only at very high dilution[57]. SMOLEC et al. 2017 similarly reported that DME engines tolerate high dilution with stable oxidation chemistry compared to diesel, particularly because of DME's high reactivity and complete vaporization[64].

The heat release traces for the EGR sweep show decreasing peak magnitude and broader combustion intervals as dilution increases, reflecting lower in-cylinder temperatures and slower overall reaction rates. Even under these cooler and more diluted conditions, particulate emissions remain low across all EGR levels and consistently below the diesel baseline. This behavior aligns with the results of SMOLEC et al. 2017 and Oda Yuji et al. 2004, who reported essentially smoke free or very low soot combustion for DME in CI engines over a wide operating range [64], [65]. Fang et al. n.d. showed that a heavy-duty DME fueled engine can achieve simultaneously low $NO_x$ and low smoke opacity up to about 40% EGR, with soot emission regions significantly smaller than for diesel due to DME's high oxygen content and absence of C–C bonds [19]. The present data confirm that increasing EGR reduces $NO_x$ without incurring a PM penalty.

At high dilution levels, additional tradeoffs emerge. When EGR exceeds approximately 40%, CO increases noticeably and rises above the diesel baseline threshold, marking the onset of incomplete oxidation caused by lower combustion temperatures and slower reaction kinetics. Plots of emissions versus $NO_x$ reveal a boundary near 0.1 g $kWh^{-1}$ where below this $NO_x$ level, CO and THC begin to rise above diesel baseline levels, and BSFC increases noticeably. This threshold is consistent with DME low temperature combustion (LTC) and high EGR studies that report similar behavior. This behavior was reported by Fang et al. n.d., who observed that high EGR in a DME fueled heavy-duty engine reduces $NO_x$ and smoke but eventually increases THC, CO, and BSFC once dilution becomes too strong [19]. Beatrice et al. n.d. documented a similar

pattern in diesel LTC experiments with clean, cooled EGR, showing that very high EGR effectively suppresses $NO_x$ but leads to incomplete combustion and higher CO, THC, and fuel consumption penalties[27].

When the injection timing and EGR results are considered together, an optimal operating region emerges. Combustion phasing centered around a CA50 of approximately 16 deg ATDC and EGR rates between 30% and 40% provide a favorable balance of low $NO_x$, low PM, controlled CO and THC, stable combustion, and efficient fuel use. Within this region, COV of IMEP and COV of CA50 remain well below stability thresholds, PM remains low, and $NO_x$ is reduced without triggering the penalties seen at extremely low $NO_x$ levels. Observed trends in prior DME CI studies support this identified optimum range.

Based on the combined results of the injection timing and EGR sweeps, the recommended operating condition for DME at 1600 rpm and 50% load is a combustion phasing near CA50 of 16 deg ATDC with an EGR rate between 30% and 40%. These values were selected because they represent the region where DME simultaneously achieves low $NO_x$, low PM, stable combustion, and acceptable efficiency without inducing the increases in CO, THC, and BSFC observed at higher dilution or more retarded phasing.

# CONCLUSION

This thesis examined the feasibility of DME as a CI fuel capable of achieving low engine out $NO_x$ emissions while maintaining negligible PM and diesel comparable brake power. The research began with the conversion of a John Deere 6068CI550 engine into a fully instrumented SCRE, followed by baseline characterization on diesel, and a series of controlled combustion experiments using DME. The work addressed all research objectives outlined in Chapter 1, including the successful conversion of the engine to single cylinder operation, complete diesel baseline testing, integration of a DME compatible fuel system, and execution of injection timing and EGR sweeps to map DME combustion behavior. Each objective was completed in a manner that directly supported the overarching goal of understanding DME's soot–$NO_x$ tradeoff and defining the limits of clean, stable combustion. Key take aways for this study are below:

1. DME produced lower overall emissions than diesel while maintaining the maintain diesel equivalent IMEP, CA50 and EGR
2. DME maintained similar thermal efficiency to diesel, despite higher mass based BSFC.
3. Low NOx and low PM occurred simultaneously with DME across the full EGR range tested (approximately 20%–55%), demonstrating the absence of a diesel like soot–NOx tradeoff.
4. DME PM consisted almost entirely of organic carbon, with negligible elemental carbon measured across all operating points.
5. DME combustion remained stable up to 55% EGR with appropriate boost and fueling support.

6. Optimal operating conditions were identified at CA50 of 16 deg ATDC and an EGR rate between 30% and 40%.
7. A combustion incompleteness threshold appeared below approximately 0.1 g $kWh^{-1}$ NOx, above which CO, THC, and BSFC noticeably increased.

Future work should focus on refining the combustion boundary identified near 0.1 g $kWh^{-1}$ $NO_x$, where CO, THC, and BSFC begin to increase and incomplete oxidation emerges. Higher resolution sweeps around this transition zone would clarify the mechanisms governing the onset of combustion instability and provide more precise calibration guidance. Additional testing at higher loads and speeds is needed to determine whether the optimal EGR region and phasing characteristics observed here persist across the broader operating map. Further investigation into multi-injection strategies, injection pressure effects, and alternative nozzle geometries may help suppress incomplete combustion products at ultra-low $NO_x$ conditions.

Future studies should expand the current test matrix using multi-variable design of experiments and optimization methods to more efficiently identify globally optimal DME operating regions. Techniques such as response surface methodology and the method of steepest ascent could be used to simultaneously vary injection timing, EGR rate, rail pressure, and boost to efficiently identify globally optimal operating regions. This approach would directly quantify how control parameters interact and would allow identification of optimal tradeoff regions between emissions, fuel consumption, and combustion stability, supporting development of full DME calibration maps.

Beyond combustion optimization, practical considerations need attention. Longer duration testing is required to evaluate DME pump, injector, and sealing reliability, and to ensure that fuel system materials can withstand DME's low lubricity. In addition, the feasibility of DME

as a commercial diesel replacement depends heavily on expanding its production and distribution network, which remains limited today. Because of DME's lower LHV compared to diesel, larger onboard fuel storage is required to achieve comparable operating duration, further emphasizing the need for supply and infrastructure development. Finally, CFD studies of DME evaporation, mixing, and ignition would help interpret the physical processes underlying the experimental results and guide future hardware and calibration strategies.

# REFERENCES


[1] J. B. . Heywood, *Internal combustion engine fundamentals*. McGraw-Hill Book Company, 1988.

[2] J. E. Sinor Consultants Inc., "Fundamental Aspects of Dimethyl Ether," *Department of Energy*, 1998.

[3] D. Stepanenko and Z. Kneba, "DME as alternative fuel for compression ignition engines-a review," *Combustion Engines*, 2019, doi: 10.19206/CE-2019-230.

[4] A. K. Agarwal, V. Kumar, H. Valera, N. K. Mukherjee, S. Mehra, and D. Nene, "Ultra-low soot/ particulate emissions from a dimethyl ether-fueled agricultural tractor engine," *Fuel*, vol. 356, Jan. 2024, doi: 10.1016/j.fuel.2023.129637.

[5] M. Y. Kim, H. Bang, and C. S. Lee, "Experimental Investigation of Spray and Combustion Characteristics of Dimethyl Ether in a Common-Rail Diesel Engine," *Energy and Fuels*, 2007, doi: 10.1021/ef060310o.

[6] "REGULATION (EU) 2016/ 1628 OF THE EUROPEAN PARLIAMENT AND OF THE COUNCIL - of 14 September 2016-on requirements relating to gaseous and particulate pollutant emission limits and type-approval for internal combustion engines for non-road mobile machinery, amending Regulations (EU) No1024/ 2012 and (EU) No 167/ 2013, and amending and repealing Directive 97/ 68/ EC," *Official Journal of the European Union*, Sep. 2016.

[7] "Control of Emissions of Air Pollution From Nonroad Diesel Engines and Fuel", Accessed: Dec. 01, 2025. [Online]. Available: www.epa.gov/edocket.

[8] "U.S. Department of Energy Continues to Fund DMEProjects." Accessed: Dec. 01, 2025. [Online]. Available: https://www.oberonfuels.com/es/us-department-of-energy-funds-dme

[9] G. A. Olah, A. Goeppert, and G. K. S. Prakash, "Chemical recycling of carbon dioxide to methanol and dimethyl ether: From greenhouse gas to renewable, environmentally carbon neutral fuels and synthetic hydrocarbons," Jan. 16, 2009. doi: 10.1021/jo801260f.

[10] "Justice40 Initiative | Environmental Justice | The White House." Accessed: Sep. 12, 2025. [Online]. Available: https://bidenwhitehouse.archives.gov/environmentaljustice/justice40/

[11] "Mission | Department of Energy." Accessed: Sep. 12, 2025. [Online]. Available: https://www.energy.gov/mission

[12] J. J. Zhang, Z. Huang, J. H. Wu, X. Q. Qiao, and J. H. Fang, “Combustion and performance of heavy-duty diesel engines fuelled with dimethyl ether,” *Proceedings of the Institution of Mechanical Engineers, Part D: Journal of Automobile Engineering*, vol. 222, no. 9, pp. 1691–1703, Sep. 2008, doi: 10.1243/09544070JAUTO783.

[13] A. K. Agarwal, V. Kumar, H. Valera, N. K. Mukherjee, S. Mehra, and D. Nene, “Ultra-low soot/ particulate emissions from a dimethyl ether-fueled agricultural tractor engine,” *Fuel*, vol. 356, Jan. 2024, doi: 10.1016/j.fuel.2023.129637.

[14] P. Soltic, T. Hilfiker, Y. Wright, G. Hardy, B. Fröhlich, and D. Klein, “The potential of dimethyl ether (DME) to meet current and future emissions standards in heavy-duty compression-ignition engines,” *Fuel*, vol. 355, Jan. 2024, doi: 10.1016/j.fuel.2023.129357.

[15] I. Youn and J. Jeon, “Combustion Performance and Low NOx Emissions of a Dimethyl Ether Compression-Ignition Engine at High Injection Pressure and High Exhaust Gas Recirculation Rate,” *Energies (Basel)*, vol. 15, no. 5, Mar. 2022, doi: 10.3390/en15051912.

[16] I. Youn and J. Jeon, “Combustion Performance and Low NOx Emissions of a Dimethyl Ether Compression-Ignition Engine at High Injection Pressure and High Exhaust Gas Recirculation Rate,” *Energies (Basel)*, vol. 15, no. 5, Mar. 2022, doi: 10.3390/en15051912.

[17] İ. Sezer, “MANAS Journal of Engineering A review study on the use of dimethyl ether in diesel engines: effects on CO2 emissions,” *MJEN MANAS Journal of Engineering*, vol. 11, no. 1, p. 2023, 2023, doi: 10.51354/mjen.

[18] S. H. Yoon, S. C. Han, and C. S. Lee, “Effects of high EGR rate on dimethyl ether (DME) combustion and pollutant emission characteristics in a direct injection diesel engine,” *Energies (Basel)*, vol. 6, no. 10, pp. 5157–5167, 2013, doi: 10.3390/en6105157.

[19] Q. Fang, Z. Huang, L. Zhu, J.-J. Zhang, and J. Xiao, “Study on low nitrogen oxide and low smoke emissions in a heavy-duty engine fuelled with dimethyl ether”, doi: 10.1177/2041299110394513.

[20] R. S. Turns, *An Introduction to Combustion Concepts and Applications*, 3rd ed. McGraw Hill, 2012.

[21] W. Shang, H. Li, K. Yang, H. Qi, and K. Nishida, “Effects of split injection strategies on evaporation dynamics and combustion performance: Role of first injection mass ratio in soot and NOx reduction,” *Energy*, vol. 332, Sep. 2025, doi: 10.1016/j.energy.2025.137214.

[22] G. Hampson and R. Reitz, “Mechanism of Soot and NOx Emission Reduction Using Multiple-Injection in a Diesel Engine,” 1996. [Online]. Available: https://www.researchgate.net/publication/254072612

[23] B. S. Haynes and H. G. Wagner, “SOOT FORMATION,” *Progress in Energy and Combustion Science, vol. 7*, vol. 7, p. 1001, 1981.

[24] J. E. Dec, “A Conceptual Model of DI Diesel Combustion Based on Laser-Sheet Imaging*,” *SAE Technical Papers*, Feb. 1997, doi: 10.4271/970873.

[25] D. T. Hountalas, G. C. Mavropoulos, and K. B. Binder, “Effect of exhaust gas recirculation (EGR) temperature for various EGR rates on heavy duty DI diesel engine performance and emissions,” *Energy*, vol. 33, no. 2, pp. 272–283, 2008, doi: 10.1016/j.energy.2007.07.002.

[26] T. Jacobs, D. Assanis, and Z. Filipi, “The Impact of Exhaust Gas Recirculation on Performance and Emissions of a Heavy-Duty Diesel Engine,” 2003.

[27] C. Beatrice, P. Capaldi, N. Del Giacomo, C. Guido, and M. Lazzaro, “The Effect of ‘Clean and Cold’ EGR on the Improvement of Low Temperature Combustion Performance in a Single Cylinder Research Diesel Engine.”

[28] John Deere, “OMAL213158.” Accessed: Sep. 12, 2025. [Online]. Available: http://manuals.deere.com/omview/OMAL213158_19/DX,FUEL1_19_20130617.html

[29] “Specification for Diesel Fuel,” Aug. 01, 2024, *ASTM International, West Conshohocken, PA*. doi: 10.1520/D0975-24A.

[30] “Higher Calorific Values of Common Fuels: Reference & Data.” Accessed: May 08, 2025. [Online]. Available: https://www.engineeringtoolbox.com/fuels-higher-calorific-values-d_169.html

[31] H. Zhu, S. V. Bohac, K. Nakashima, L. M. Hagen, Z. Huang, and D. N. Assanis, “Effect of fuel oxygen on the trade-offs between soot, NOx and combustion efficiency in premixed low-temperature diesel engine combustion,” *Fuel*, vol. 112, pp. 459–465, 2013, doi: 10.1016/j.fuel.2013.05.023.

[32] N. Raeie, S. Emami, and O. Karimi Sadaghiyani, “Effects of injection timing, before and after top dead center on the propulsion and power in a diesel engine,” *Propulsion and Power Research*, vol. 3, no. 2, pp. 59–67, Jun. 2014, doi: 10.1016/j.jppr.2014.06.001.

[33] I. Diesel Engine Author, R. C. Yu, and S. M. Shahed, “Effects of Injection Timing and Exhaust Gas Recirculation on Emissions from a D.I. Diesel Engine,” 1981.

[34] C. W. Squibb, H. Schock, R. Vedula, and T. Stuecken, “Analysis of Variations in Fuel Spray, Combustion, and Soot Production in an Optical Diesel Engine Operating under

High Simulated Exhaust Gas Recirculation Operating Conditions," in *SAE Technical Papers*, SAE International, 2016. doi: 10.4271/2016-01-0727.

[35] İ. Sezer, "Effects of dimethyl ether on cyclic variations in compression ignition engines," *Eurasian Journal of Science Engineering and Technology*, vol. 6, no. 2, pp. 121–135, Jul. 2025, doi: 10.55696/ejset.1662475.

[36] T. Kanda, T. Hakozaki, T. Uchimoto, J. Hatano, N. Kitayama, and H. Sono, "2005-01-0378 PCCI Operation with Early Injection of Conventional Diesel Fuel." [Online]. Available: www.sae.org

[37] M. C. Besch, A. N. Covington, D. Johnson, N. Fowler, and R. Heltzel, "Effects of EGR Addition onto Combustion Stability and Alternator Performance Variability of a Small, Single-Cylinder Diesel Generator," in *SAE Technical Papers*, SAE International, Nov. 2016. doi: 10.4271/2016-32-0063.

[38] F. Zhang, Z. Wang, J. Tian, L. Li, K. Yu, and K. He, "Effect of EGR and fuel injection strategies on the heavy-duty diesel engine emission performance under transient operation," *Energies (Basel)*, vol. 13, no. 3, 2020, doi: 10.3390/en13030566.

[39] J. Felipe, R. Rueda, D. B. Olsen, B. Windom, D. Baker, and J. Quinn, "DISSERTATION EXPANDING THE KNOCK/EMISSIONS LIMITS FOR THE REALIZATION OF ULTRA-LOW EMISSIONS, HIGH-EFFICIENCY HEAVY-DUTY NATURAL GAS ENGINES Submitted by," 2023.

[40] C. L'orange, G. Neymark, E. Carter, and J. Volckens, "A high-throughput, robotic system for analysis of aerosol sampling filters," *Aerosol Air Qual Res*, vol. 21, no. 11, 2021, doi: 10.4209/AAQR.210037.

[41] Eileen Birch M., "NIOSH Manual of Analytical Methods (NMAM), Fourth Edition," Mar. 2003.

[42] Hussain. Jaffar, Palaniradja. K, Natarajan. Alagumurthi, and Manimaran. R, "Effect of Exhaust Gas Recirculation (EGR) on Performance and Emission of a Compression Ignition Engine with Staged Combustion (Insertion of Unburned Hydrocarbon)," *International Journal of Energy Engineering*, vol. 2, no. 6, pp. 285–292, Dec. 2012, doi: 10.5923/j.ijee.20120206.03.

[43] J. M. Desantes, J. Galindo, C. Guardiola, and V. Dolz, "Air mass flow estimation in turbocharged diesel engines from in-cylinder pressure measurement," *Exp Therm Fluid Sci*, vol. 34, no. 1, pp. 37–47, Jan. 2010, doi: 10.1016/j.expthermflusci.2009.08.009.

[44] M. Zheng, G. T. Reader, and J. G. Hawley, "Diesel engine exhaust gas recirculation - A review on advanced and novel concepts," *Energy Convers Manag*, vol. 45, no. 6, pp. 883–900, 2004, doi: 10.1016/S0196-8904(03)00194-8.

[45] Y. Wang, Y. Zhuang, M. Yao, Y. Qin, and Z. Zheng, “An experimental investigation into the soot particle emissions at early injection timings in a single-cylinder research diesel engine,” *Fuel*, vol. 316, May 2022, doi: 10.1016/j.fuel.2022.123288.

[46] A. Vressner, *Studies on the Load Range of an HCCI Engine using In-Cylinder Pressure, Ion Current and Optical Diagnostics*. 2003.

[47] H. Persson, “Spark Assisted Compression Ignition, SACI,” Lund University, 2008.

[48] Kistler Group, “High-Temperature Pressure Sensor for Combustion Engine Measurements, Type 6052C, datasheet no. 6052C_000-552e-03.24,” Winterthur, Switzerland, 2006.

[49] Windom and Bret, “Poly(oxymethylene) Ethers as a High Cetane, Low Sooting Biofuel Blendstock for Use in Medium to Heavy Duty Mixing Controlled Compression Ignition Engines,” Dec. 2023. doi: 10.2172/2448099.

[50] C. Arcoumanis, C. Bae, R. Crookes, and E. Kinoshita, “The potential of di-methyl ether (DME) as an alternative fuel for compression-ignition engines: A review,” Jun. 2008. doi: 10.1016/j.fuel.2007.06.007.

[51] Y. Putrasari and O. Lim, “Dimethyl Ether as the Next Generation Fuel to Control Nitrogen Oxides and Particulate Matter Emissions from Internal Combustion Engines: A Review,” 2021, doi: 10.1021/acsomega.1c03885.

[52] “Reciprocating internal combustion engines-Exhaust emission measurement-Part 1: COPYRIGHT PROTECTED DOCUMENT,” 2020. [Online]. Available: https://standards.iteh.ai/catalog/standards/sist/4c414d60-cdef-4c95-a588-

[53] U. Epa, O. of Transportation, A. Quality, S. Division, and prepared for EPA by Southwest Research Institute, “Determination of PEMS Measurement Allowances for Gaseous Emissions Regulated Under the Heavy-Duty Diesel Engine In-Use Testing Program: Revised Final Report (EPA420-R-08-005).”

[54] M. Y. Kim, S. H. Bang, and C. S. Lee, “Experimental investigation of spray and combustion characteristics of dimethyl ether in a common-rail diesel engine,” *Energy and Fuels*, vol. 21, no. 2, pp. 793–800, Mar. 2007, doi: 10.1021/ef060310o.

[55] J. Song, Z. Huang, X. Qiao, and W. Wang, “Performance of a controllable premixed combustion engine fueled with dimethyl ether,” *Energy Convers Manag*, vol. 45, no. 13–14, pp. 2223–2232, Aug. 2004, doi: 10.1016/j.enconman.2003.11.004.

[56] Z. H. Huang, H. W. Wang, Y. Chen, L. B. Zhou, and D. M. Jiang, “Study of combustion characteristics of a compression ignition engine fuelled with dimethyl ether,” 1999.

[57] H. G. Roh, S. Park, and C. S. Lee, “Effect of Exhaust Gas Recirculation on the Combustion and Emissions of Dimethyl Ether in a Passenger Vehicle Diesel Engine,” *Journal of Energy Engineering*, vol. 144, no. 5, p. 04018061, Aug. 2018, doi: 10.1061/(ASCE)EY.1943-7897.0000575.

[58] S. H. Park, J. Cha, and C. S. Lee, “Reduction of the pollutant emissions from a diesel engine by the application of dimethyl ether (DME) and the control of the intake oxygen flow rate,” in *Energy and Fuels*, May 2012, pp. 3024–3033. doi: 10.1021/ef300297b.

[59] H. Teng, J. C. McCandless, and J. B. Schneyer, “Compression Ignition Delay (Physical + Chemical) of Dimethyl Ether - An Alternative Fuel for Compression-Ignition Engines,” *SAE Technical Papers*, Mar. 2003, doi: 10.4271/2003-01-0759.

[60] K. D. Cung, A. A. Moiz, X. Zhu, and S. Y. Lee, “Ignition Process and Flame Lift-Off Characteristics of dimethyl ether (DME) Reacting Spray,” *Front Mech Eng*, vol. 7, Mar. 2021, doi: 10.3389/fmech.2021.547204.

[61] A. Jamrozik, W. Tutak, R. Gnatowska, and Ł. Nowak, “Comparative analysis of the combustion stability of diesel-methanol and diesel-ethanol in a dual fuel engine,” *Energies (Basel)*, vol. 12, no. 6, 2019, doi: 10.3390/en12060971.

[62] M. Y. Kim, S. H. Yoon, B. W. Ryu, and C. S. Lee, “Combustion and emission characteristics of DME as an alternative fuel for compression ignition engines with a high pressure injection system,” *Fuel*, vol. 87, no. 12, pp. 2779–2786, Sep. 2008, doi: 10.1016/j.fuel.2008.01.032.

[63] J. Zhang, X. Qiao, Z. Wang, B. Guan, and Z. Huang, “Experimental investigation of low-temperature combustion (LTC) in an engine fueled with dimethyl ether (DME),” *Energy and Fuels*, vol. 23, no. 1, pp. 170–174, Jan. 2009, doi: 10.1021/ef800674s.

[64] R. SMOLEC, M. IDZIOR, W. KARPIUK, and M. KOZAK, “Assessment of the potential of dimethyl ether as an alternative fuel for compression ignition engines,” *Combustion Engines*, vol. 169, no. 2, pp. 181–186, May 2017, doi: 10.19206/ce-2017-232.

[65] Oda Yuji, Osafune Shinnosuke, Ueda Hiroyuki, and Fujimura Koutaro, “Clean Combustion Technology in Diesel Engines Operated with Dimethyl ether,” Dec. 2004.

APPENDIX A: SOLID MODELS

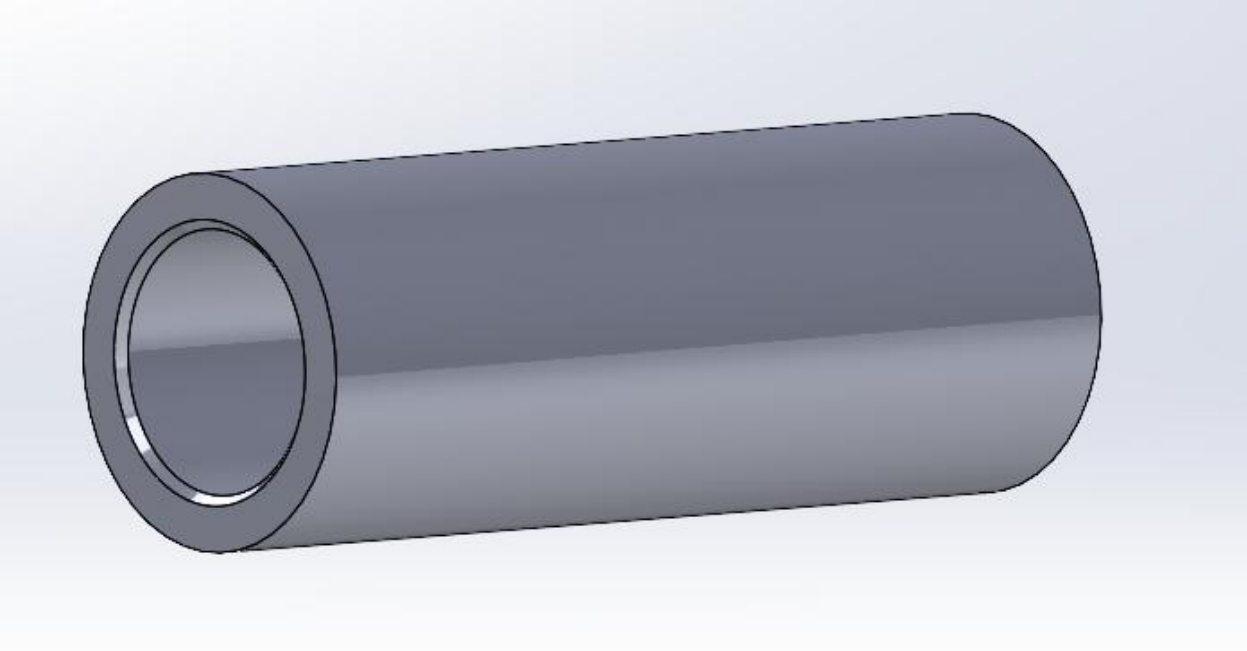

**A- 1.** SolidWorks model of rocker arm deactivation sleeve

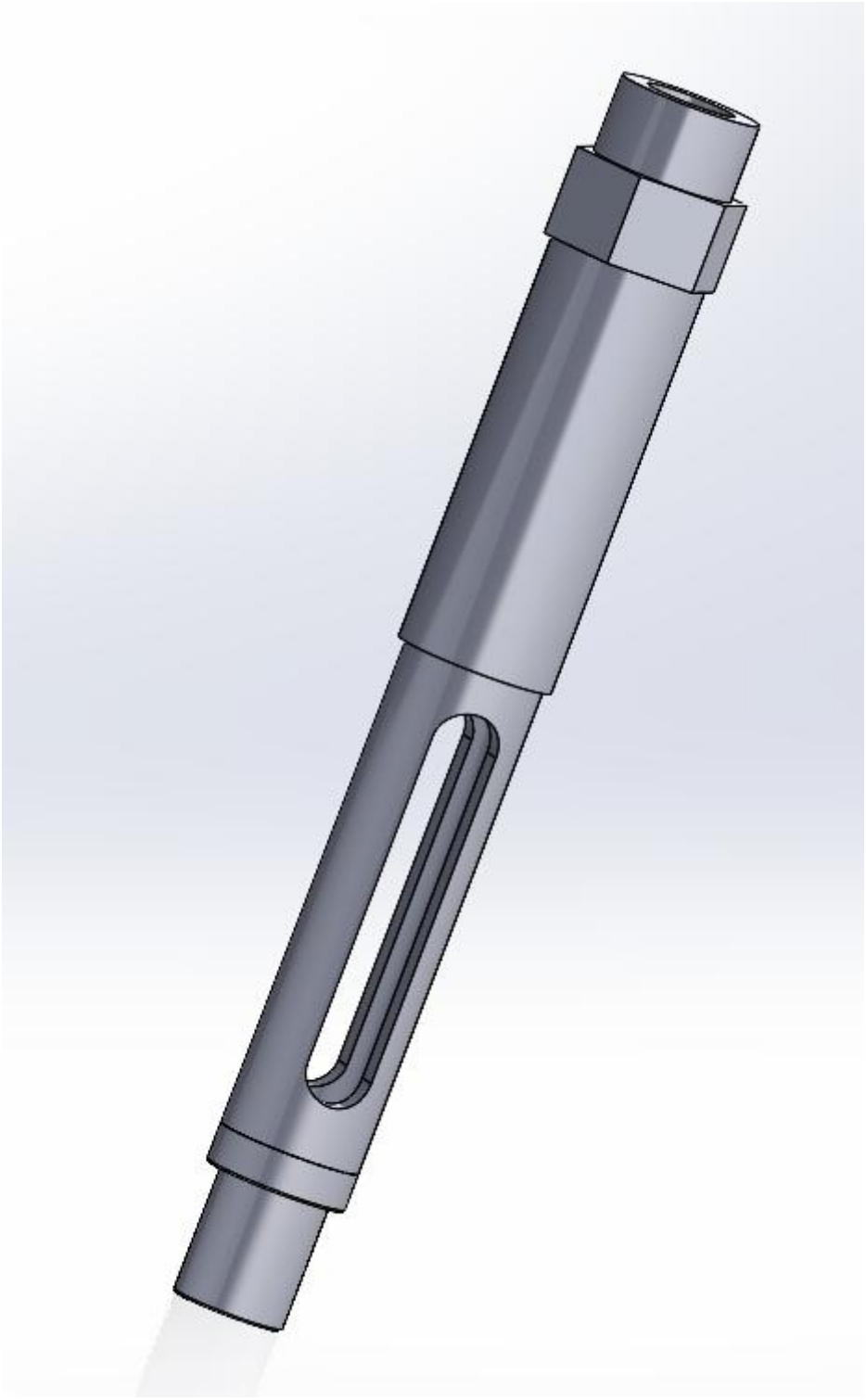

**A- 2.** SolidWorks model of adapter from AVL pressure transducer to Kistler pressure transducer

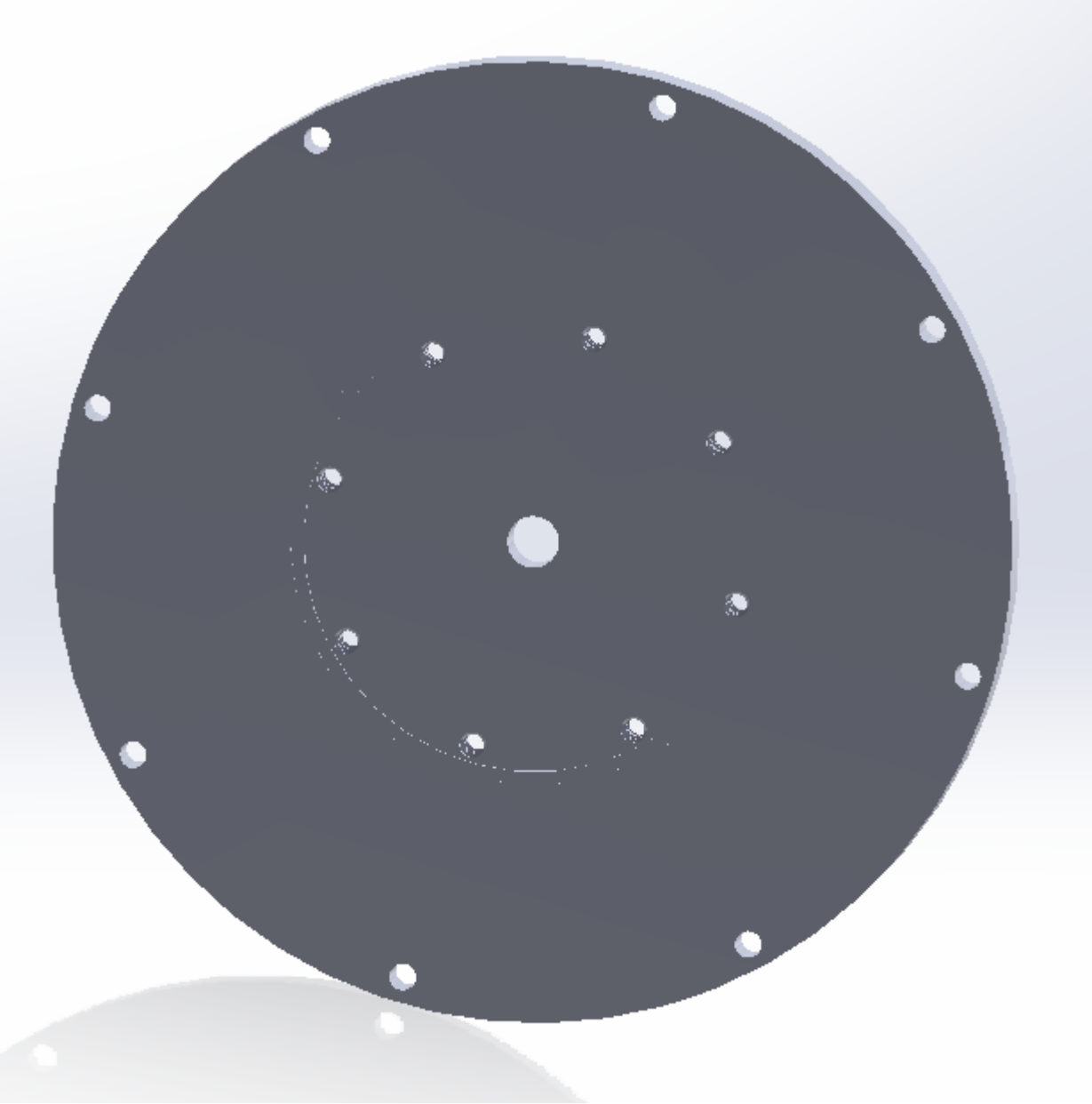

**A- 3.** SolidWorks model of flywheel adapter plate from the John Deere flywheel to the dyno driveshaft

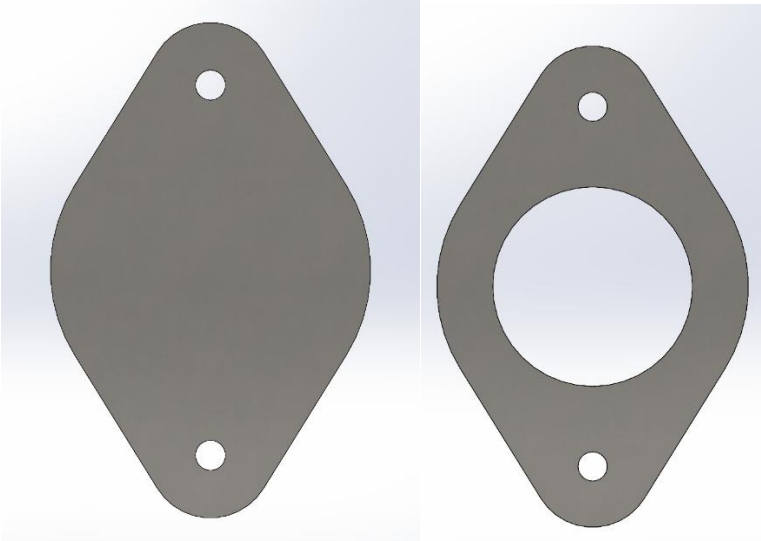

**A- 4.** Left**:** SolidWorks models of the exhaust block off plate Right: SolidWorks model of exhaust spacer

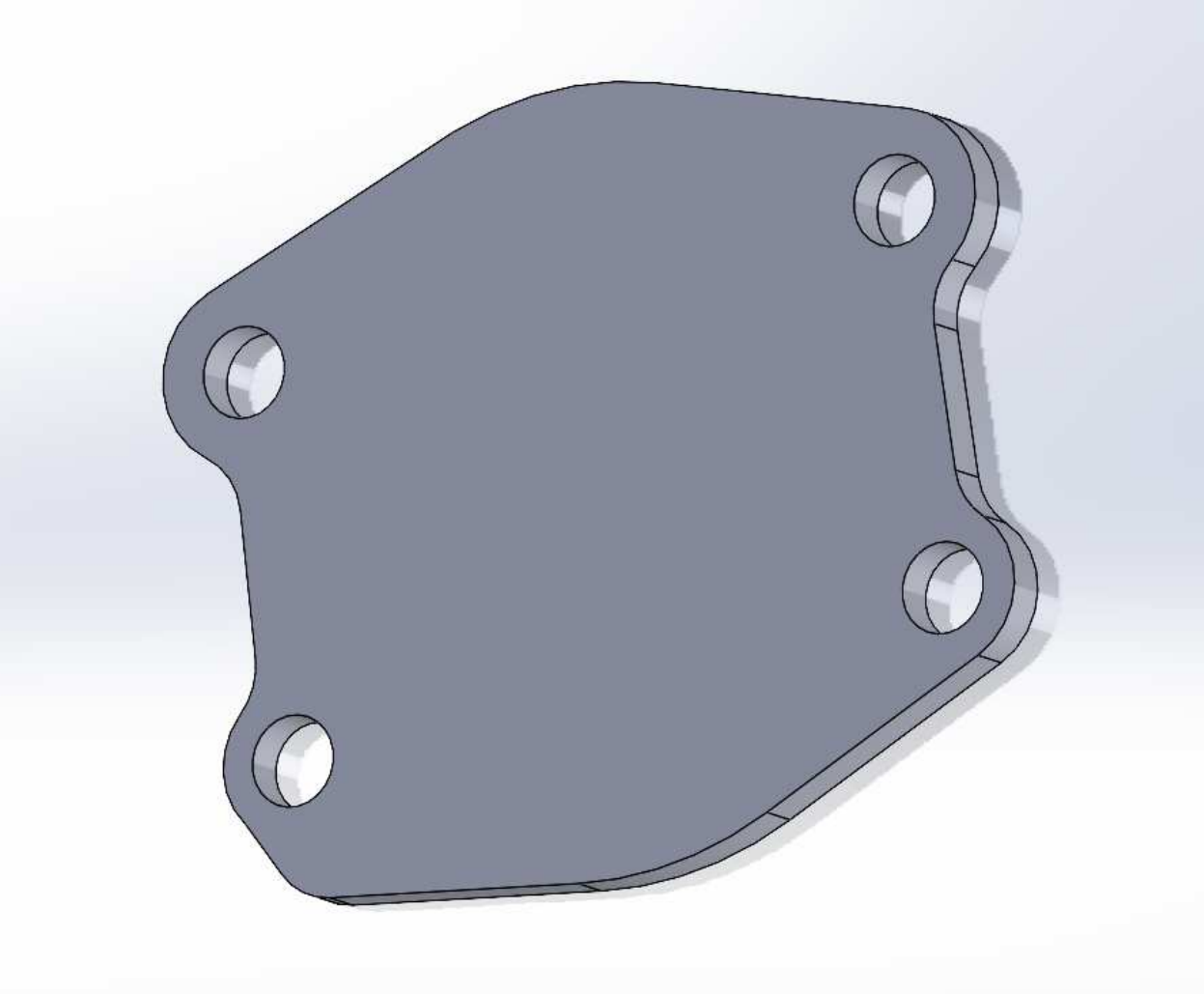

**A- 5.** SolidWorks model of diesel high pressure pump block off plate

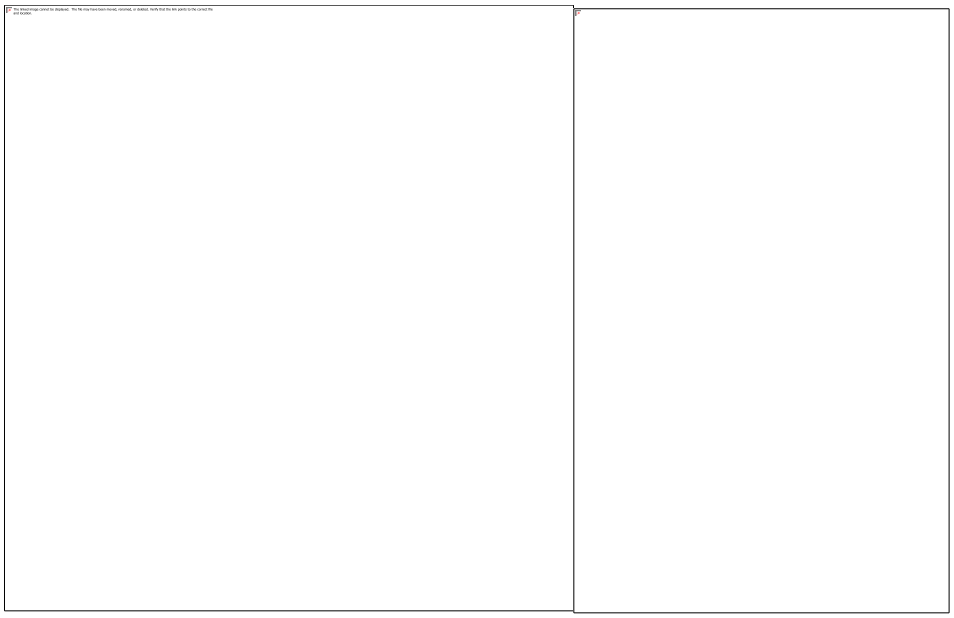

**A- 6.** SolidWorks model showing alternative routing of accessory belt in SCRE configuration

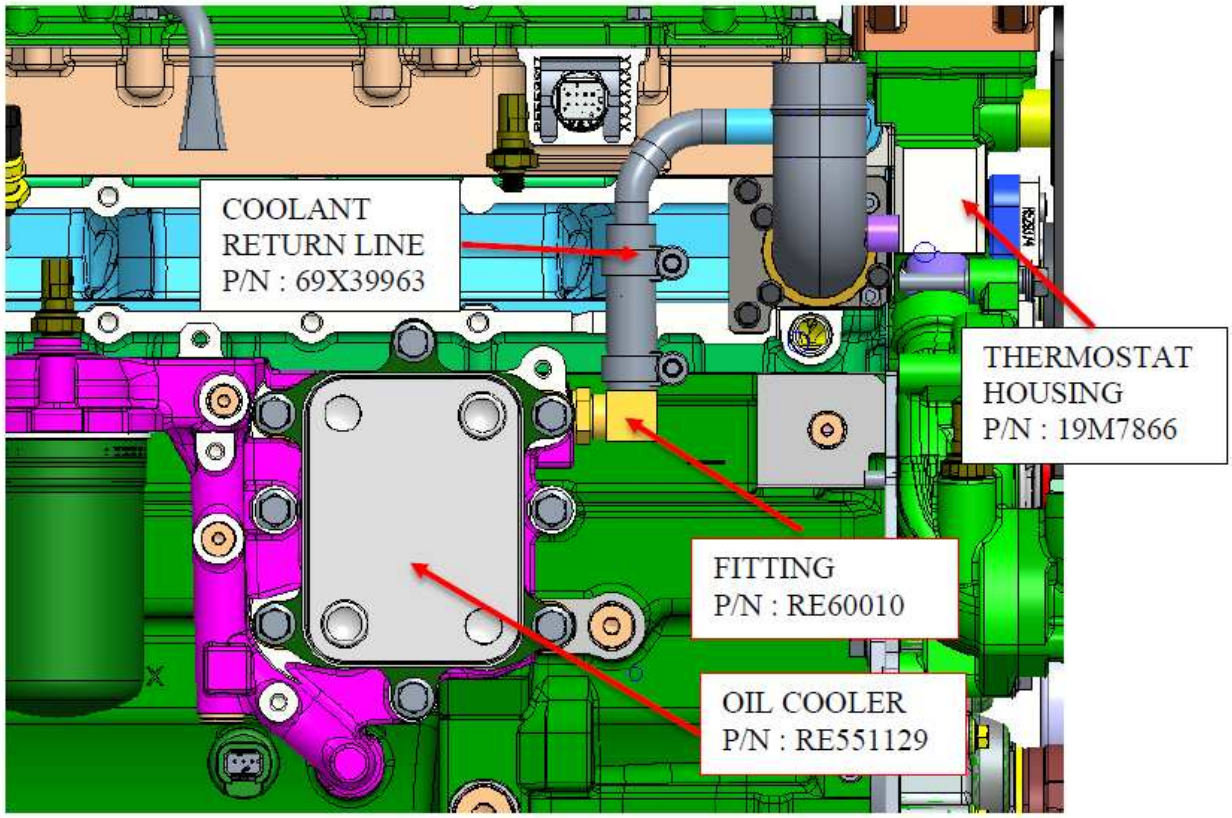


**A- 7.** SolidWorks modeling showing SCRE intake configuration with modified head, thermostat housing and rerouted coolant line for the oil cooler

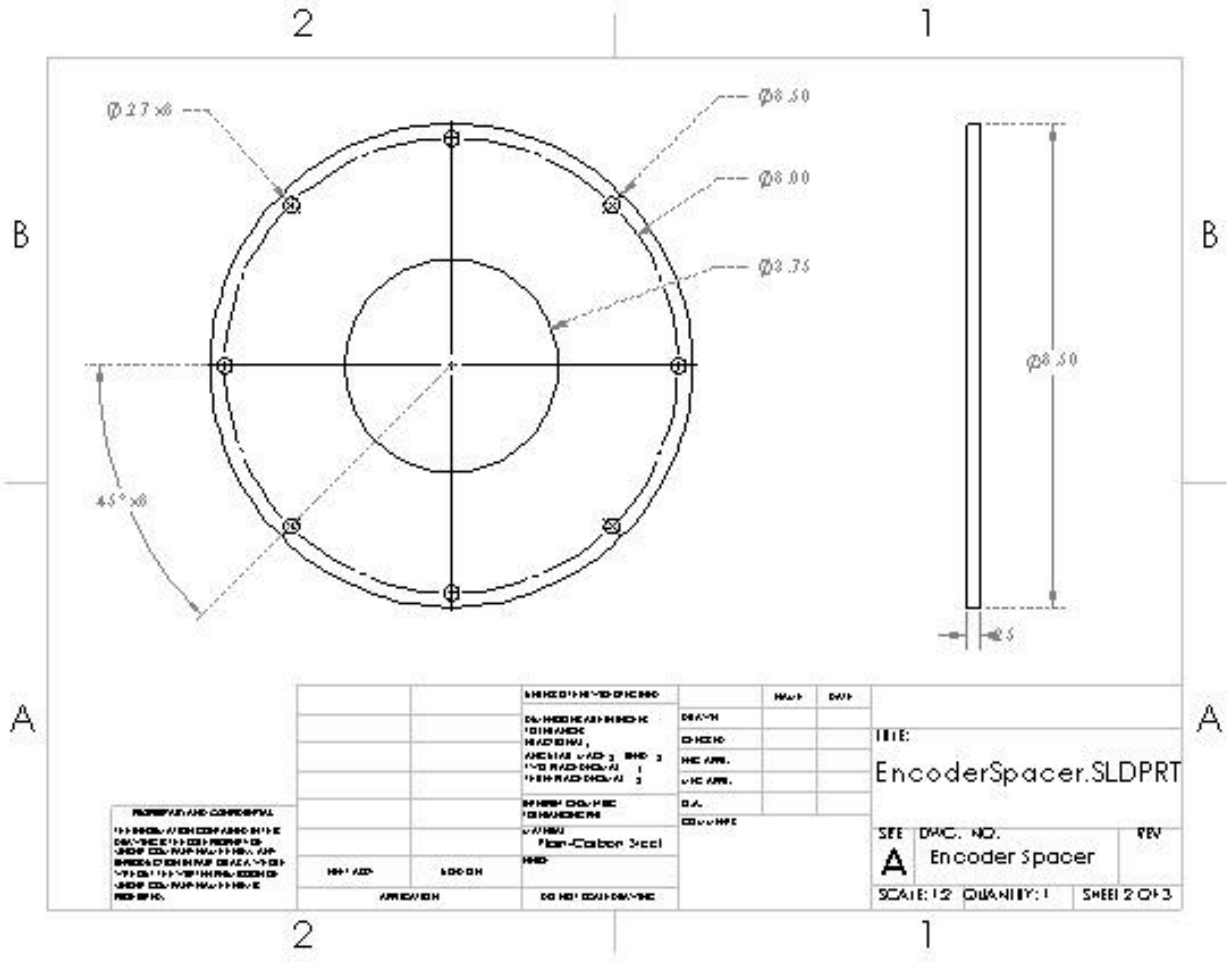


**B- 1.** Drawing of front encoder mounting plate

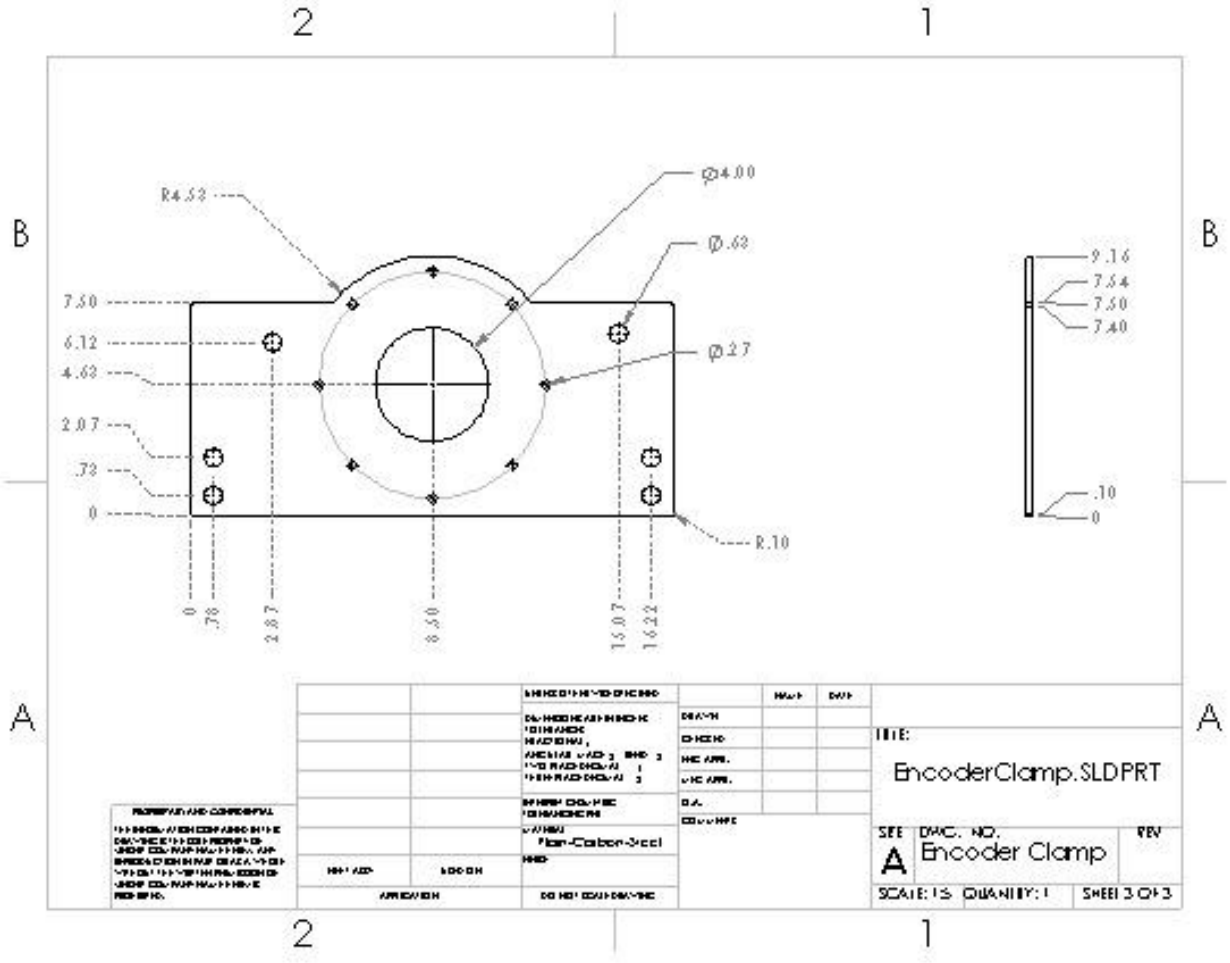


**B- 2.** Drawing of main encoder mounting plate

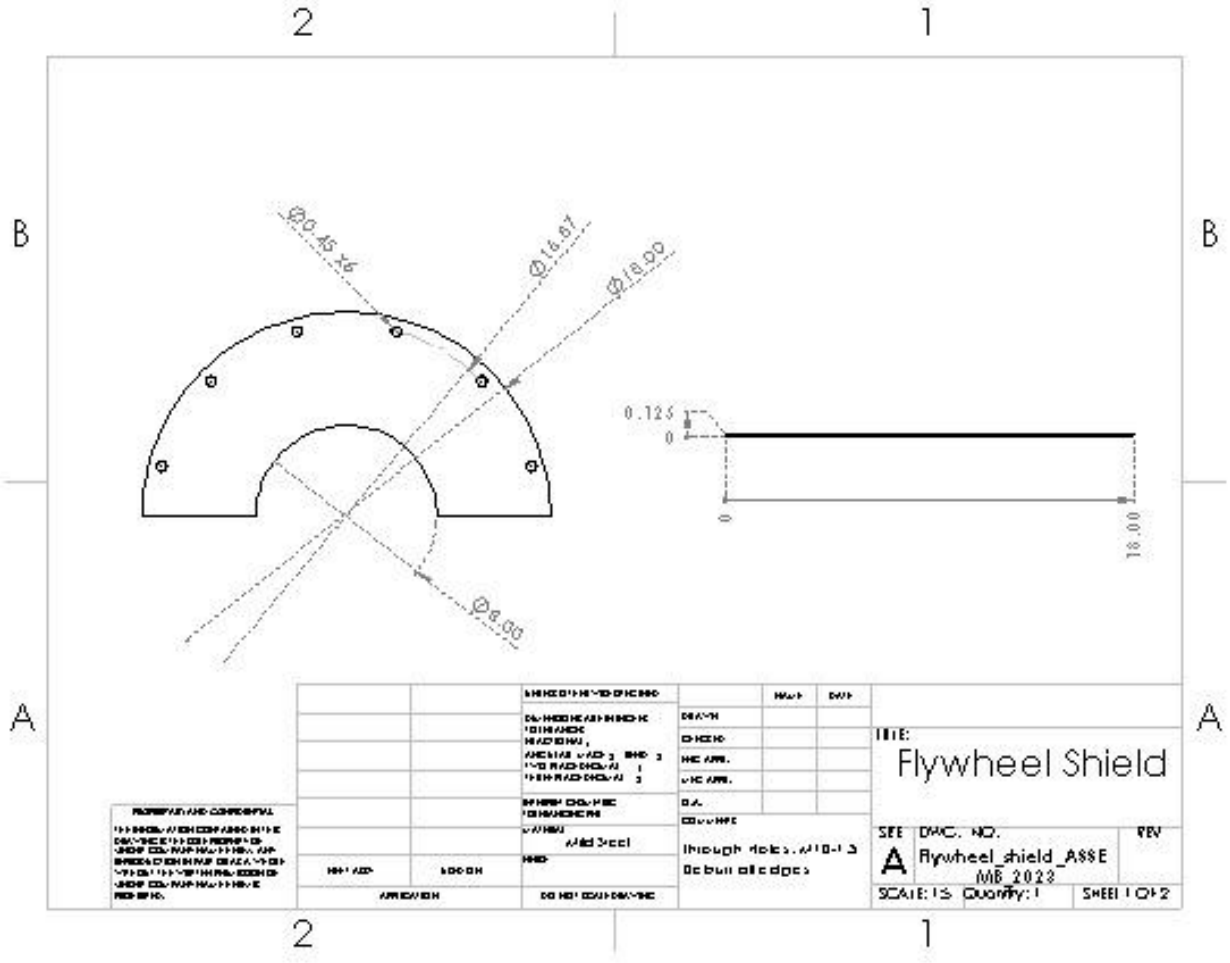


**B- 3.** Drawing of flywheel shield

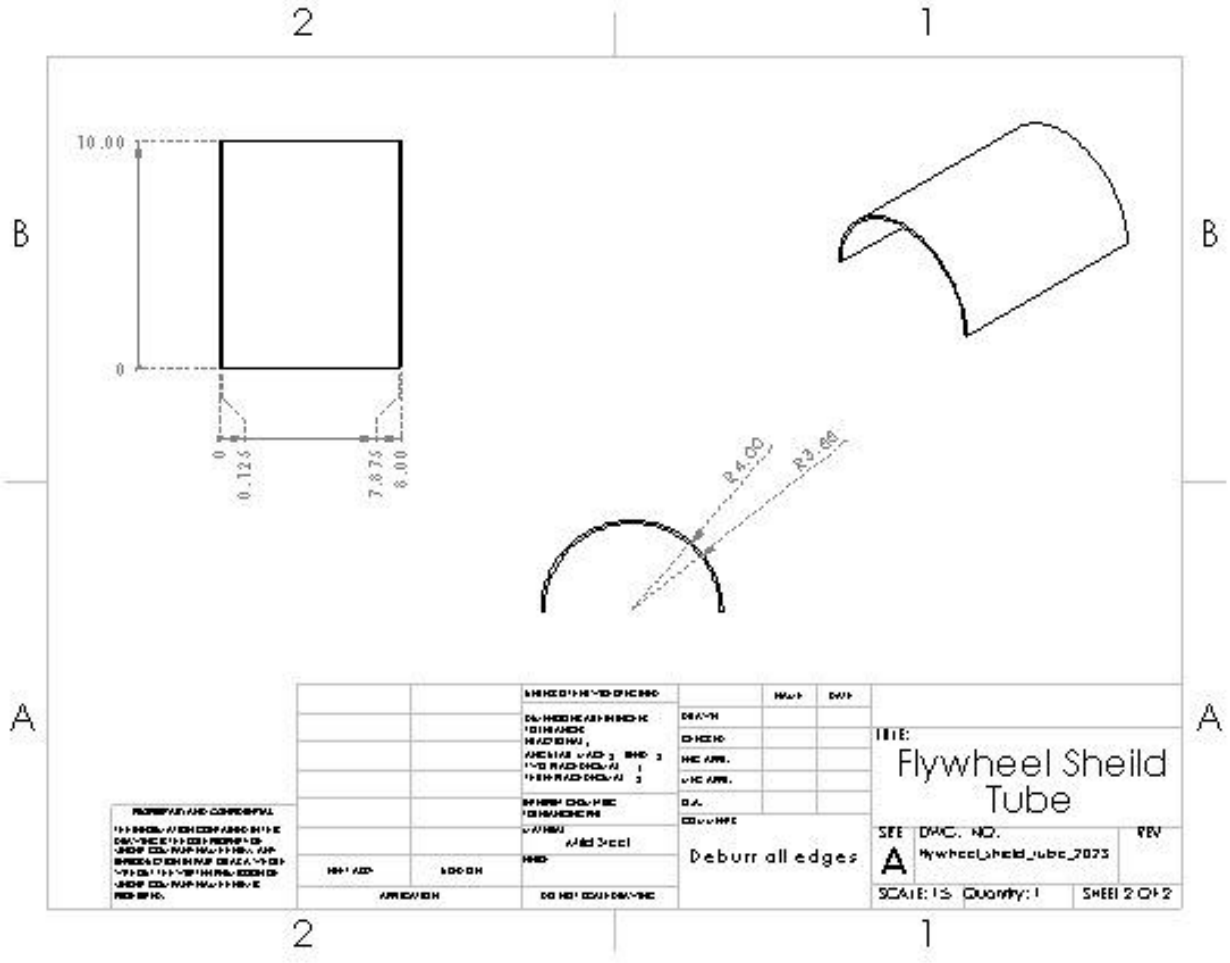


**B- 4.** Drawing of driveshaft shield

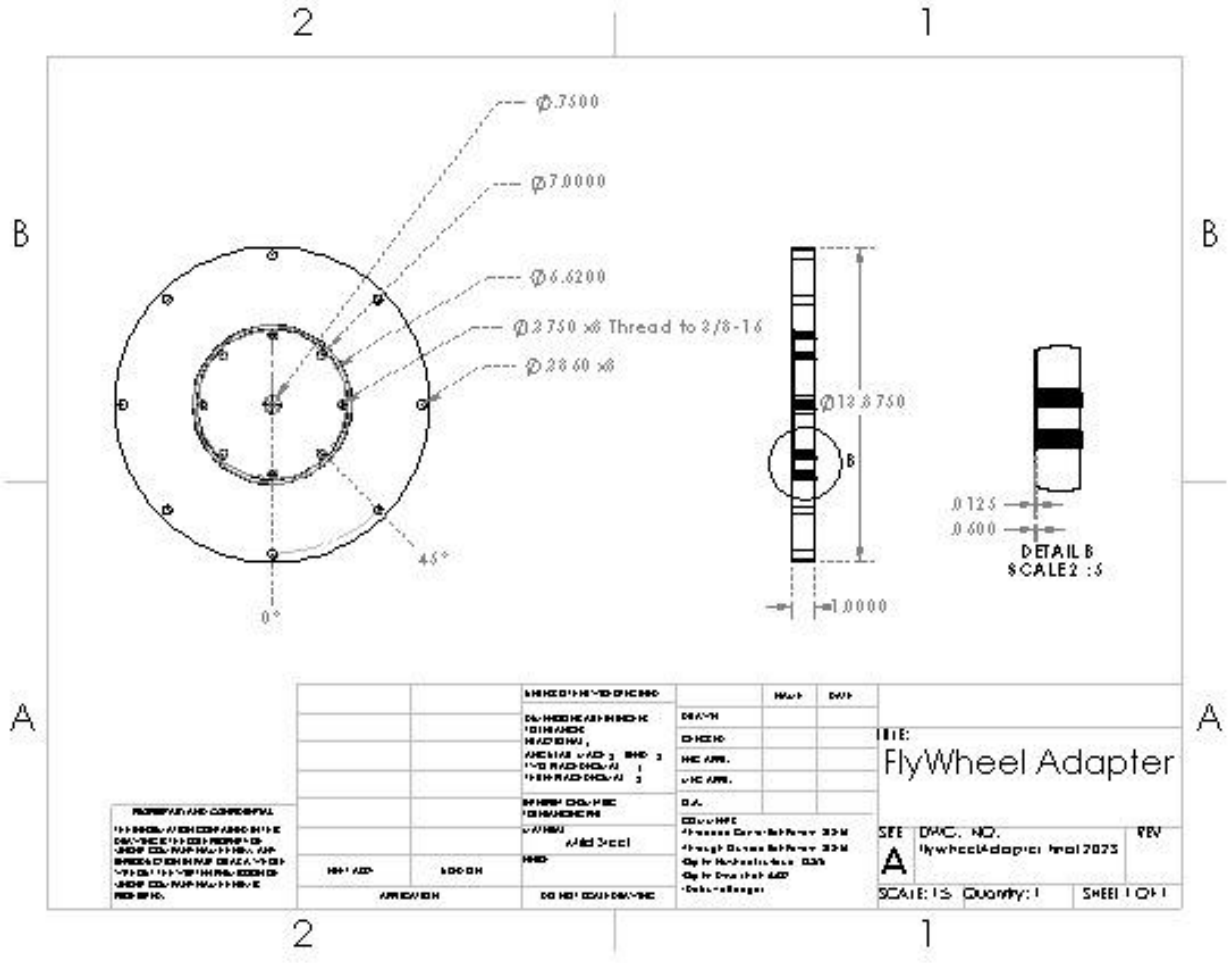


**B- 5.** Drawing of flywheel adapter

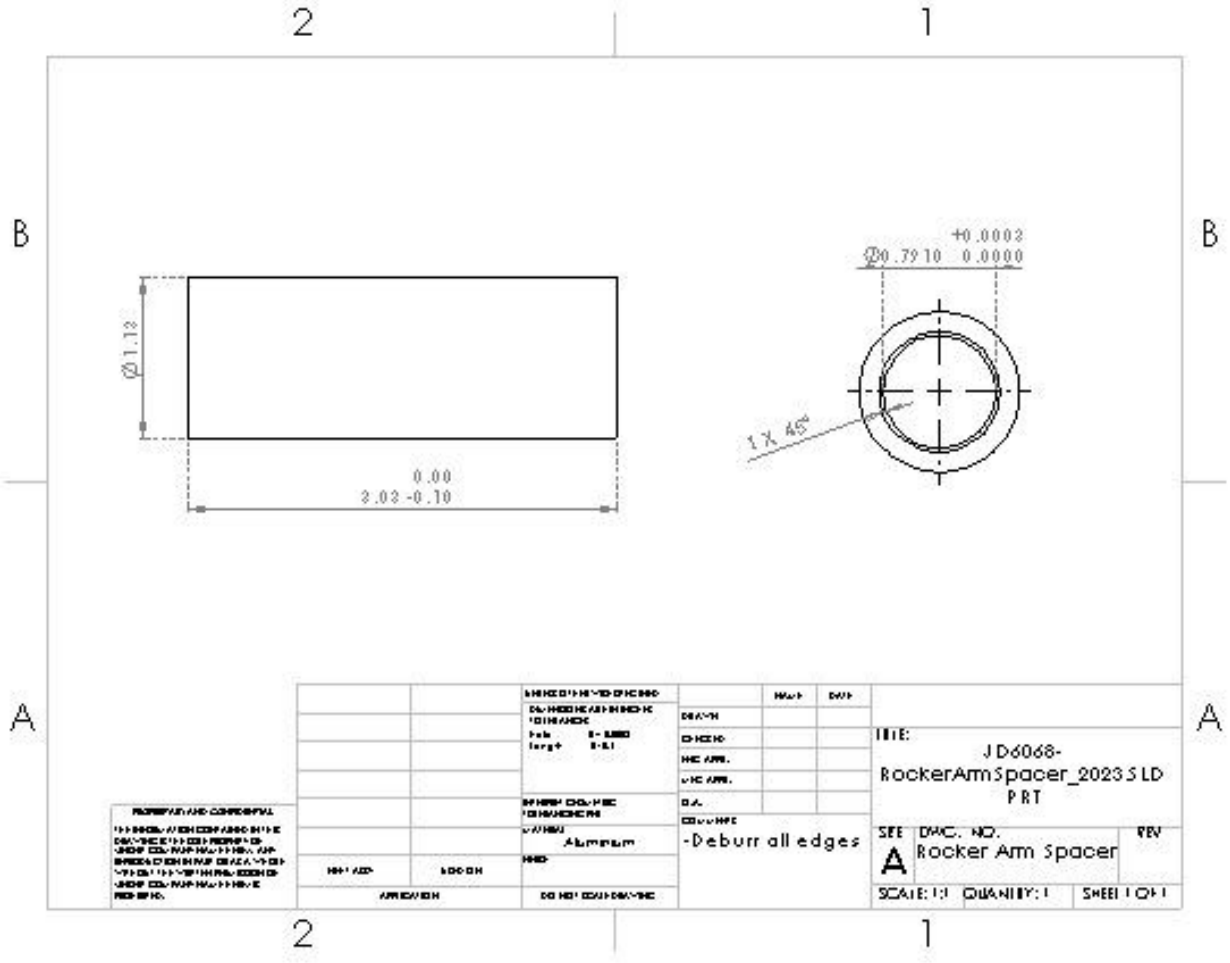


**B- 6.** Drawing of rocker arm spacer sleeve

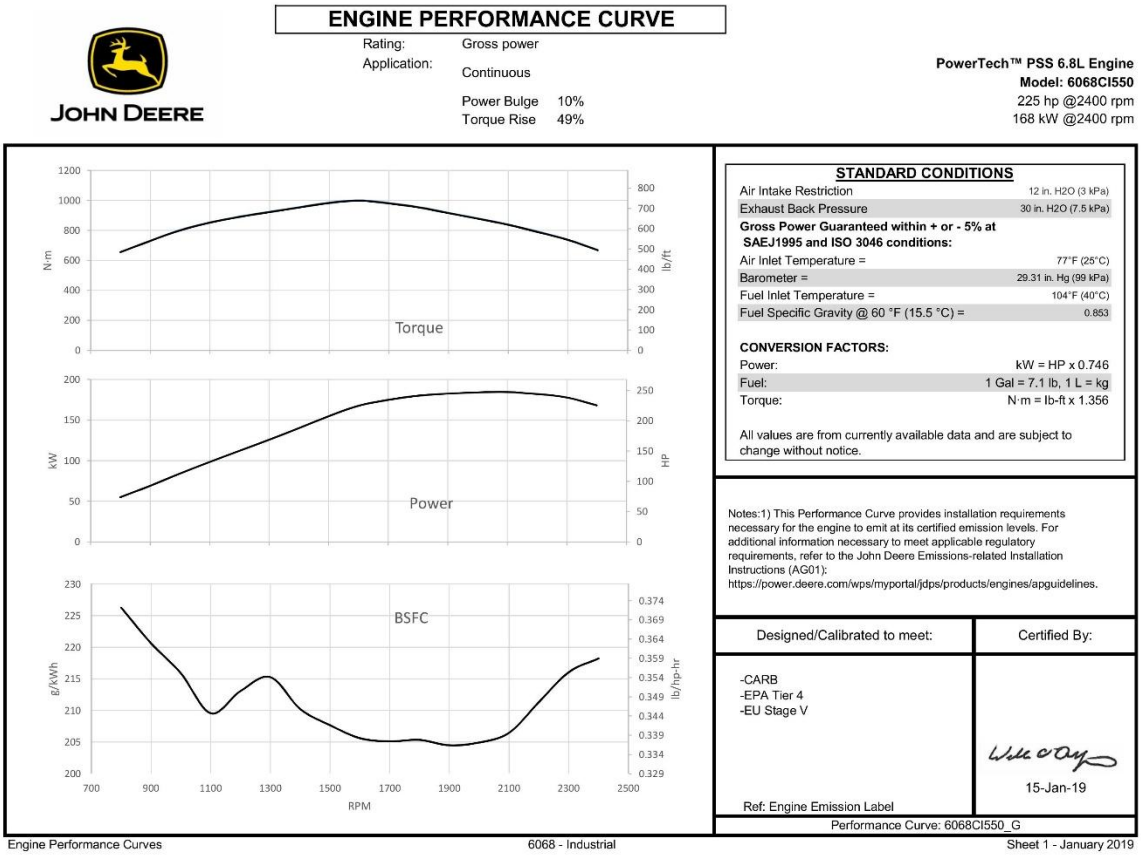


**C- 1.** Performance curves for the John Deere 6068CI550 (torque, power, and BSFC)

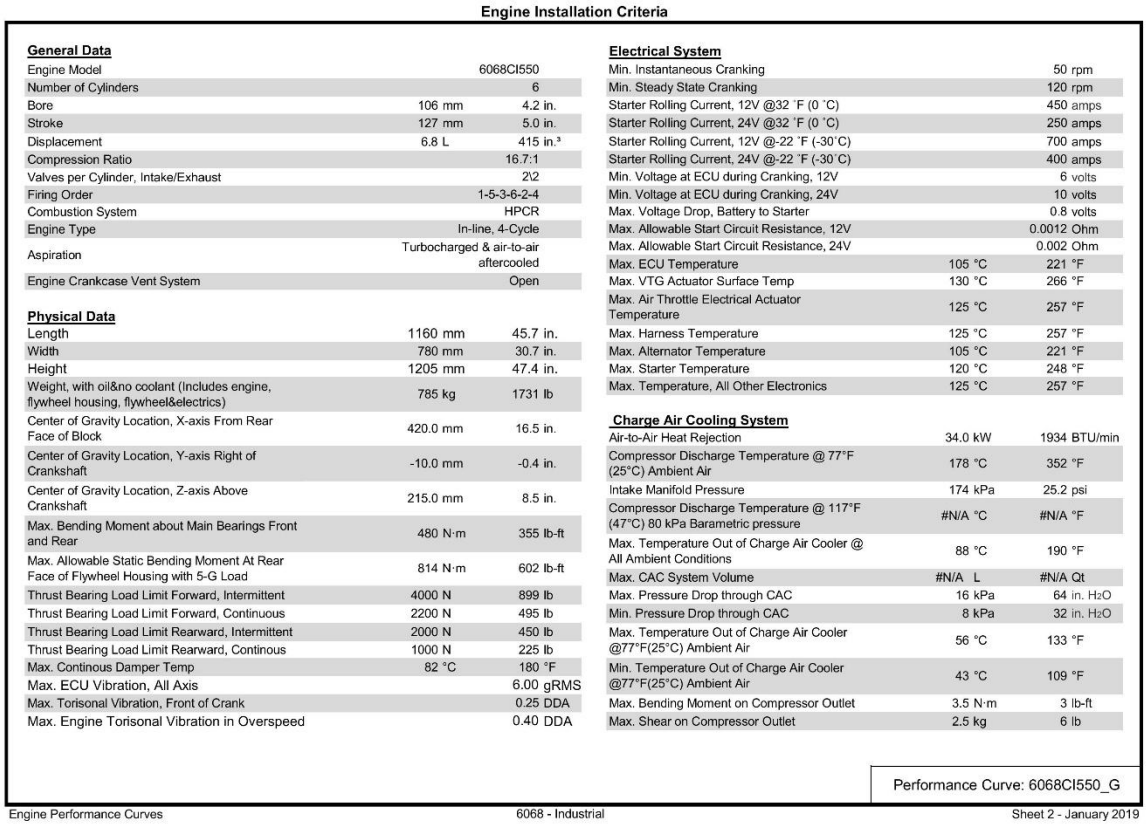

**Engine Installation Criteria**

**General Data**

| | | |
|---|---|---|
| Engine Model | | 6068CI550 |
| Number of Cylinders | | 6 |
| Bore | 106 mm | 4.2 in. |
| Stroke | 127 mm | 5.0 in. |
| Displacement | 6.8 L | 415 in.³ |
| Compression Ratio | | 16.7:1 |
| Valves per Cylinder, Intake/Exhaust | | 2\2 |
| Firing Order | | 1-5-3-6-2-4 |
| Combustion System | | HPCR |
| Engine Type | | In-line, 4-Cycle |
| Aspiration | | Turbocharged & air-to-air aftercooled |
| Engine Crankcase Vent System | | Open |

**Physical Data**

| | | |
|---|---|---|
| Length | 1160 mm | 45.7 in. |
| Width | 780 mm | 30.7 in. |
| Height | 1205 mm | 47.4 in. |
| Weight, with oil&no coolant (Includes engine, flywheel housing, flywheel&electrics) | 785 kg | 1731 lb |
| Center of Gravity Location, X-axis From Rear Face of Block | 420.0 mm | 16.5 in. |
| Center of Gravity Location, Y-axis Right of Crankshaft | -10.0 mm | -0.4 in. |
| Center of Gravity Location, Z-axis Above Crankshaft | 215.0 mm | 8.5 in. |
| Max. Bending Moment about Main Bearings Front and Rear | 480 N·m | 355 lb-ft |
| Max. Allowable Static Bending Moment At Rear Face of Flywheel Housing with 5-G Load | 814 N·m | 602 lb-ft |
| Thrust Bearing Load Limit Forward, Intermittent | 4000 N | 899 lb |
| Thrust Bearing Load Limit Forward, Continuous | 2200 N | 495 lb |
| Thrust Bearing Load Limit Rearward, Intermittent | 2000 N | 450 lb |
| Thrust Bearing Load Limit Rearward, Continous | 1000 N | 225 lb |
| Max. Continous Damper Temp | 82 °C | 180 °F |
| Max. ECU Vibration, All Axis | | 6.00 gRMS |
| Max. Torisonal Vibration, Front of Crank | | 0.25 DDA |
| Max. Engine Torisonal Vibration in Overspeed | | 0.40 DDA |

**Electrical System**

| | | |
|---|---|---|
| Min. Instantaneous Cranking | | 50 rpm |
| Min. Steady State Cranking | | 120 rpm |
| Starter Rolling Current, 12V @32 °F (0 °C) | | 450 amps |
| Starter Rolling Current, 24V @32 °F (0 °C) | | 250 amps |
| Starter Rolling Current, 12V @-22 °F (-30°C) | | 700 amps |
| Starter Rolling Current, 24V @-22 °F (-30°C) | | 400 amps |
| Min. Voltage at ECU during Cranking, 12V | | 6 volts |
| Min. Voltage at ECU during Cranking, 24V | | 10 volts |
| Max. Voltage Drop, Battery to Starter | | 0.8 volts |
| Max. Allowable Start Circuit Resistance, 12V | | 0.0012 Ohm |
| Max. Allowable Start Circuit Resistance, 24V | | 0.002 Ohm |
| Max. ECU Temperature | 105 °C | 221 °F |
| Max. VTG Actuator Surface Temp | 130 °C | 266 °F |
| Max. Air Throttle Electrical Actuator Temperature | 125 °C | 257 °F |
| Max. Harness Temperature | 125 °C | 257 °F |
| Max. Alternator Temperature | 105 °C | 221 °F |
| Max. Starter Temperature | 120 °C | 248 °F |
| Max. Temperature, All Other Electronics | 125 °C | 257 °F |

**Charge Air Cooling System**

| | | |
|---|---|---|
| Air-to-Air Heat Rejection | 34.0 kW | 1934 BTU/min |
| Compressor Discharge Temperature @ 77°F (25°C) Ambient Air | 178 °C | 352 °F |
| Intake Manifold Pressure | 174 kPa | 25.2 psi |
| Compressor Discharge Temperature @ 117°F (47°C) 80 kPa Barametric pressure | #N/A °C | #N/A °F |
| Max. Temperature Out of Charge Air Cooler @ All Ambient Conditions | 88 °C | 190 °F |
| Max. CAC System Volume | #N/A L | #N/A Qt |
| Max. Pressure Drop through CAC | 16 kPa | 64 in. $H_2O$ |
| Min. Pressure Drop through CAC | 8 kPa | 32 in. $H_2O$ |
| Max. Temperature Out of Charge Air Cooler @77°F(25°C) Ambient Air | 56 °C | 133 °F |
| Min. Temperature Out of Charge Air Cooler @77°F(25°C) Ambient Air | 43 °C | 109 °F |
| Max. Bending Moment on Compressor Outlet | 3.5 N·m | 3 lb-ft |
| Max. Shear on Compressor Outlet | 2.5 kg | 6 lb |

Performance Curve: 6068CI550_G

Engine Performance Curves | 6068 - Industrial | Sheet 2 - January 2019

**C- 2.** General engine specifications and installation criteria for the 6068CI550

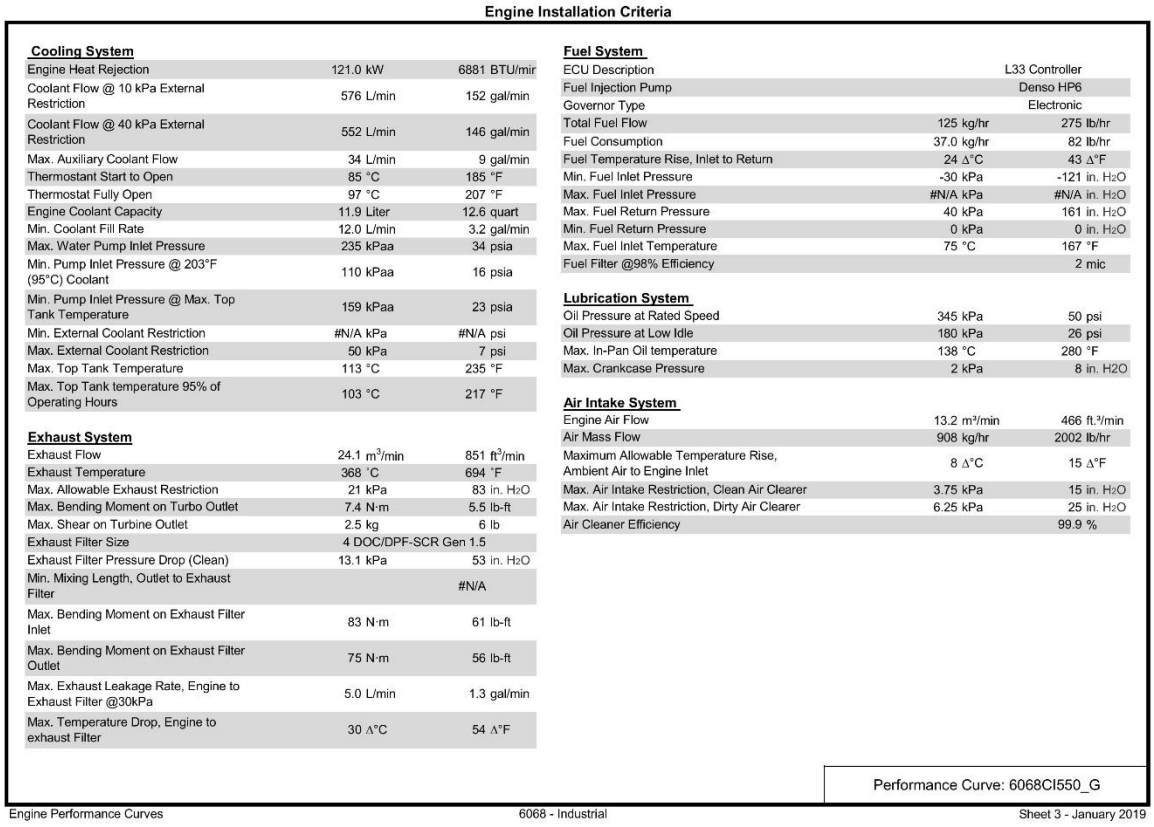

**Engine Installation Criteria**

**Cooling System**

| | | |
|---|---|---|
| Engine Heat Rejection | 121.0 kW | 6881 BTU/mir |
| Coolant Flow @ 10 kPa External Restriction | 576 L/min | 152 gal/min |
| Coolant Flow @ 40 kPa External Restriction | 552 L/min | 146 gal/min |
| Max. Auxiliary Coolant Flow | 34 L/min | 9 gal/min |
| Thermostant Start to Open | 85 °C | 185 °F |
| Thermostat Fully Open | 97 °C | 207 °F |
| Engine Coolant Capacity | 11.9 Liter | 12.6 quart |
| Min. Coolant Fill Rate | 12.0 L/min | 3.2 gal/min |
| Max. Water Pump Inlet Pressure | 235 kPaa | 34 psia |
| Min. Pump Inlet Pressure @ 203°F (95°C) Coolant | 110 kPaa | 16 psia |
| Min. Pump Inlet Pressure @ Max. Top Tank Temperature | 159 kPaa | 23 psia |
| Min. External Coolant Restriction | #N/A kPa | #N/A psi |
| Max. External Coolant Restriction | 50 kPa | 7 psi |
| Max. Top Tank Temperature | 113 °C | 235 °F |
| Max. Top Tank temperature 95% of Operating Hours | 103 °C | 217 °F |

**Exhaust System**

| | | |
|---|---|---|
| Exhaust Flow | 24.1 $m^3$/min | 851 $ft^3$/min |
| Exhaust Temperature | 368 °C | 694 °F |
| Max. Allowable Exhaust Restriction | 21 kPa | 83 in. $H_2O$ |
| Max. Bending Moment on Turbo Outlet | 7.4 N·m | 5.5 lb-ft |
| Max. Shear on Turbine Outlet | 2.5 kg | 6 lb |
| Exhaust Filter Size | 4 DOC/DPF-SCR Gen 1.5 | |
| Exhaust Filter Pressure Drop (Clean) | 13.1 kPa | 53 in. $H_2O$ |
| Min. Mixing Length, Outlet to Exhaust Filter | | #N/A |
| Max. Bending Moment on Exhaust Filter Inlet | 83 N·m | 61 lb-ft |
| Max. Bending Moment on Exhaust Filter Outlet | 75 N·m | 56 lb-ft |
| Max. Exhaust Leakage Rate, Engine to Exhaust Filter @30kPa | 5.0 L/min | 1.3 gal/min |
| Max. Temperature Drop, Engine to exhaust Filter | 30 Δ°C | 54 Δ°F |

**Fuel System**

| | | |
|---|---|---|
| ECU Description | | L33 Controller |
| Fuel Injection Pump | | Denso HP6 |
| Governor Type | | Electronic |
| Total Fuel Flow | 125 kg/hr | 275 lb/hr |
| Fuel Consumption | 37.0 kg/hr | 82 lb/hr |
| Fuel Temperature Rise, Inlet to Return | 24 Δ°C | 43 Δ°F |
| Min. Fuel Inlet Pressure | -30 kPa | -121 in. $H_2O$ |
| Max. Fuel Inlet Pressure | #N/A kPa | #N/A in. $H_2O$ |
| Max. Fuel Return Pressure | 40 kPa | 161 in. $H_2O$ |
| Min. Fuel Return Pressure | 0 kPa | 0 in. $H_2O$ |
| Max. Fuel Inlet Temperature | 75 °C | 167 °F |
| Fuel Filter @98% Efficiency | | 2 mic |

**Lubrication System**

| | | |
|---|---|---|
| Oil Pressure at Rated Speed | 345 kPa | 50 psi |
| Oil Pressure at Low Idle | 180 kPa | 26 psi |
| Max. In-Pan Oil temperature | 138 °C | 280 °F |
| Max. Crankcase Pressure | 2 kPa | 8 in. H2O |

**Air Intake System**

| | | |
|---|---|---|
| Engine Air Flow | 13.2 $m^3$/min | 466 $ft.^3$/min |
| Air Mass Flow | 908 kg/hr | 2002 lb/hr |
| Maximum Allowable Temperature Rise, Ambient Air to Engine Inlet | 8 Δ°C | 15 Δ°F |
| Max. Air Intake Restriction, Clean Air Clearer | 3.75 kPa | 15 in. $H_2O$ |
| Max. Air Intake Restriction, Dirty Air Clearer | 6.25 kPa | 25 in. $H_2O$ |
| Air Cleaner Efficiency | | 99.9 % |

Performance Curve: 6068CI550_G

Engine Performance Curves 6068 - Industrial Sheet 3 - January 2019

**C- 3.** Cooling, fuel, lubrication, exhaust system and air intake system specifications for the 6068CI550

**Engine Installation Criteria**

**Performance Data**

| | | |
|---|---|---|
| Rated Power | 168 kW | 225 HP |
| Rated Speed | | 2400 rpm |
| Max. Fast Idle Speed | | 2600 rpm |
| Breakway Speed | | 2450 rpm |
| Power Bulge Speed | | 2200 rpm |
| Peak Torque Speed | | 1600 rpm |
| Low Idle Speed | | 800 rpm |
| Rated Torque | 669 N·m | 495.06 lb-ft |
| Peak Torque | 1000 N·m | 740 lb-ft |
| Power Bulge | | 10 % |
| Torque Rise | | 49 % |
| BMEP, Rated | | 1237 psi |
| BMEP, Peak Torque | 1855 kPa | 269 psi |
| Attitude Capability | 3048 m | 10000 ft |
| Friction Power @Rated Speed | 36 kW | 48 HP |
| Air Fuel Ratio | | 24.8:1 |
| Noise @1 m | | 95 dB(A) |

**DEF Data**

| Load Factor | Engine Speed | DEF Consumption* | | Percent of Diesel Consumption** |
|---|---|---|---|---|
| % | RPM | g/kWh | lb/hp-hr | % |
| 100 | 2400 | 6.9 | 0.0113 | 2.5 |
| Peak Torque | 1600 | 6.9 | 0.0113 | 6.9 |

*DEF conversion factor: 1.087 kg/l (9.071 lb/gal)

**Percent of diesel consumption by volume at 100% load and peak torque

**Curved Data**

| Engine Speed | Power | | Torque | | BSFC | |
|---|---|---|---|---|---|---|
| rpm | kW | hp | N·M | lb-ft | g/kWh | lb/hp-hr |
| 800 | 55 | 74 | 656 | 484 | 226 | 0.372 |
| 900 | 69 | 92 | 731 | 539 | 221 | 0.363 |
| 1000 | 84 | 113 | 802 | 592 | 216 | 0.355 |
| 1100 | 98 | 132 | 853 | 630 | 210 | 0.345 |
| 1200 | 112 | 150 | 892 | 658 | 213 | 0.350 |
| 1300 | 126 | 169 | 924 | 682 | 215 | 0.354 |
| 1400 | 140 | 188 | 955 | 705 | 210 | 0.346 |
| 1500 | 155 | 207 | 985 | 727 | 208 | 0.341 |
| 1600 | 168 | 225 | 1000 | 738 | 206 | 0.338 |
| 1700 | 175 | 234 | 982 | 725 | 205 | 0.337 |
| 1800 | 180 | 241 | 955 | 705 | 205 | 0.338 |
| 1900 | 182 | 245 | 917 | 677 | 205 | 0.336 |
| 2000 | 184 | 247 | 879 | 649 | 205 | 0.337 |
| 2100 | 185 | 247 | 839 | 619 | 206 | 0.339 |
| 2200 | 182 | 244 | 790 | 583 | 211 | 0.347 |
| 2300 | 178 | 238 | 738 | 545 | 216 | 0.355 |
| 2400 | 168 | 225 | 669 | 494 | 218 | 0.359 |

Performance Curve: 6068CI550_G

Engine Performance Curves 6068 - Industrial Sheet 4 - January 2019

**C- 4.** Performance data and curved data for the 6068CI550

# APPENDIX D: EXTRA PLOTS

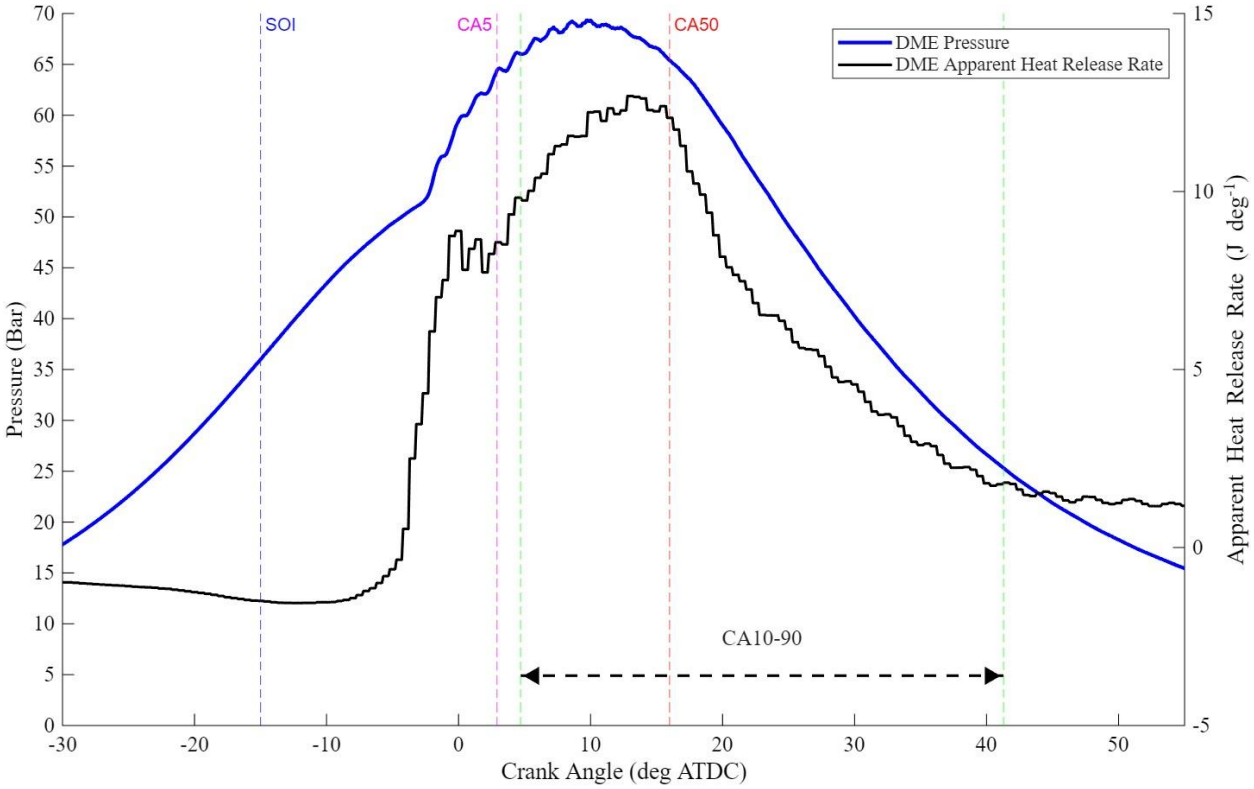


**D- 1.** DME average pressure trace and apparent heat release rate 2200 rpm 50% load with location of 50% mass burned of 16 deg ATDC

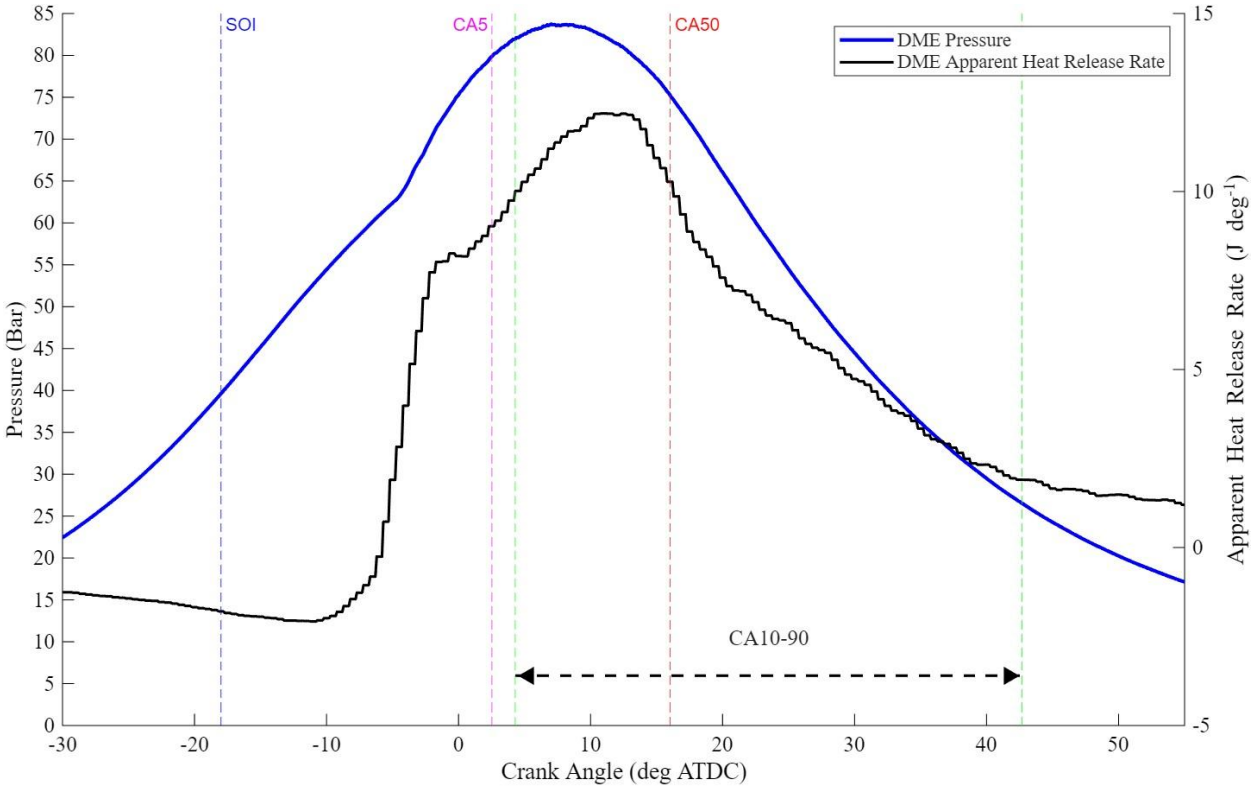


**D- 2.** DME average pressure trace and apparent heat release rate 2200 rpm 50% load with 47% exhaust gas recirculation

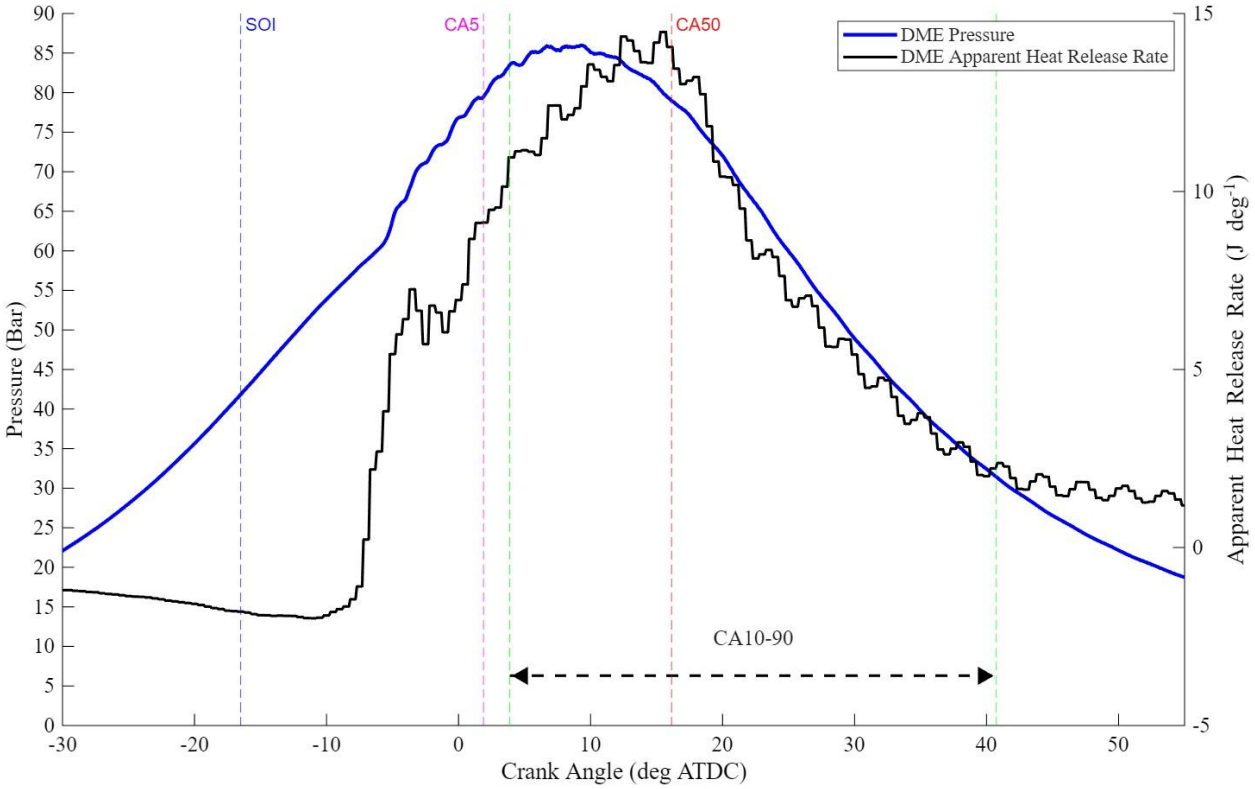


**D- 3.** DME average pressure trace and apparent heat release rate 2200 rpm 75% load with location of 50% mass burned of 16 deg ATDC

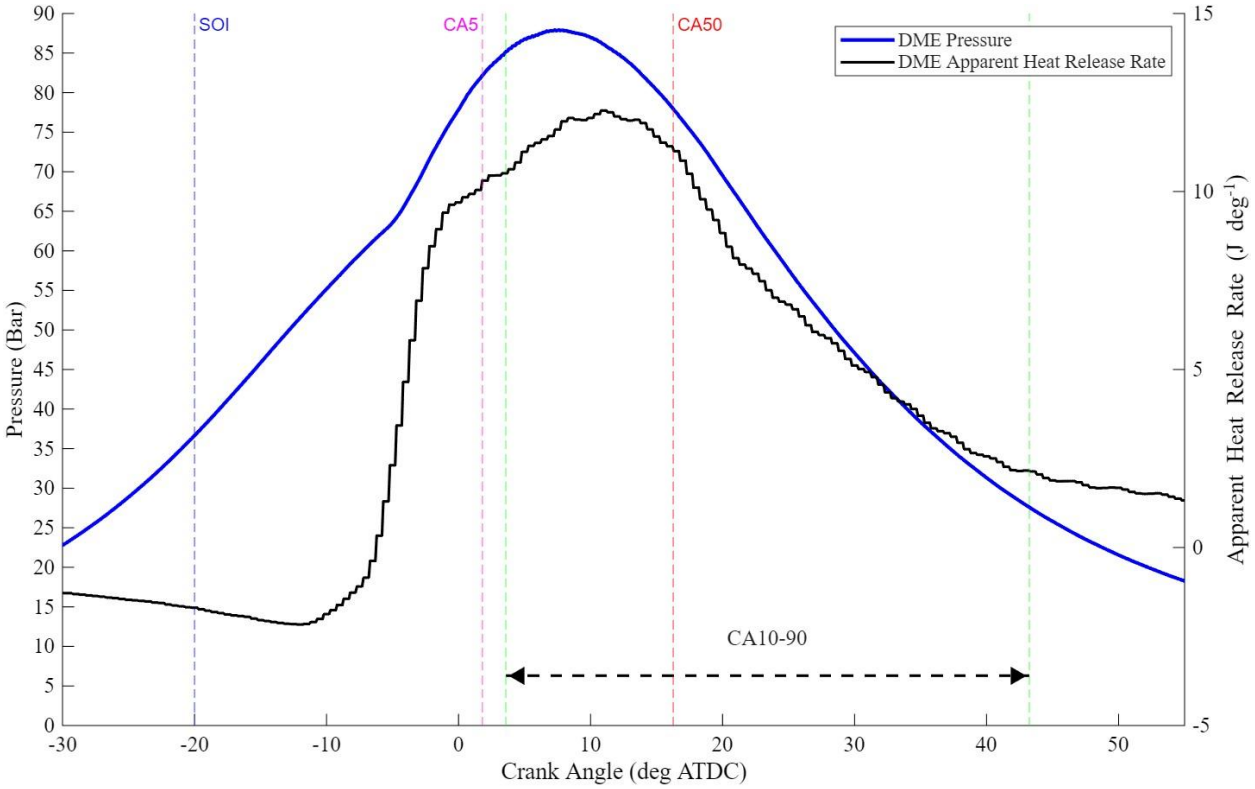


**D- 4.** DME average pressure trace and apparent heat release rate 2200 rpm 75% load with 49% exhaust gas recirculation